Alma Mater Studiorum · Università di Bologna

SCUOLA DI SCIENZE
Corso di Laurea in Astrofisica e Cosmologia
Dipartimento di Fisica e Astronomia

A COMBINED JVLA AND CHANDRA STUDY OF THE ABELL 2626 GALAXY CLUSTER

Tesi di Laurea Magistrale in Astrofisica e Cosmologia

Relatore:
Chiar.ma Prof.ssa
Myriam GITTI

Candidato:
Alessandro IGNESTI

Co-Relatore:
Dr. **Gianfranco BRUNETTI**

Sessione III
Anno Accademico 2015/2016

THIS THESIS WORK WAS DONE AS
PART OF THE RESEARCH ACTIVITY OF
THE
ISTITUTO DI RADIOASTRONOMIA -
ISTITUTO NAZIONALE DI ASTROFISICA
(BOLOGNA)

Per aspera,
ad astra.

Abstract

In questo lavoro di Tesi è stata svolta un'accurata analisi di nuove osservazioni dell'ammasso di galassie Abell 2626 in banda radio e nella banda dei raggi X. Abell 2626 è un ammasso composto da $\sim$70 galassie, delle quali la più brillante è la galassia centrale IC5338, caratterizzata dalla presenza di due nuclei ottici distanti 3.3 kpc. In banda X, Abell 2626 è classificato come ammasso cool-core, mentre la sua emissione radio è composta dall'emissione della radiogalassia associata a IC5338, che esibisce una coppia di getti, e da un'emissione estesa entro $\sim$60 kpc dal centro, composta da un gruppo di particolari radio sorgenti, gli *archi*, le cui proprietà sono diverse da quelle solite delle sorgenti diffuse negli ammassi. Molti modelli sono stati proposti negli anni passati per spiegare le loro origini, uno dei più promettenti ipotizza che gli archi siano scie di hot-spot, che si stanno muovendo per effetto della precessione dei getti di IC5338.

Nel nostro lavoro studiamo l'origine di questi archi. Abbiamo analizzato due nuove osservazioni JVLA dell'ammasso a 3.0 e 5.5 GHz. Così facendo abbiamo osservato gli archi a 3.0 GHz e trovato evidenze di emissione estesa al loro interno a 5.5 GHz. Combinando mappe d'archivio a 1.4 GHz con le nuove a 3.0 GHz abbiamo stimato che gli archi abbiano un indice spettrale $\alpha \sim$-3. Queste mappe sono state un test del modello di precessione dei getti, che prevedeva una variazione dello spettro lungo gli archi, dovuta alla diversa età radiativa del plasma depositato in tempi diversi. Studiando lo spettro di sincrotrone degli archi siamo riusciti a valutarne l'età radiativa, mentre dalla distribuzione dell'indice spettrale abbiamo stimato un tempo scala Δt_{rad} =5-10 Myr per la precessione dei getti. Questo tempo scala si è rivelato essere molto più breve del periodo stimato per la precessione dei due nuclei di IC5338. L'analisi di una nuova osservazione CHANDRA dell'ammasso ha portato a risultati sorprendenti. Abbiamo evidenziato una connessione spaziale fra gli archi radio e la regione di gas freddo nel centro dell'ammasso e, soprattutto, abbiamo scoperto un *cold-front* coincidente con due archi.

E' noto che la turbolenza nei cold fronts possa accelerare particelle relativistiche e generare emissione radio in forma di mini-aloni. In alcuni casi, tali emissioni risultano come sottili archi a spettro molto ripido, che tracciano la disposizione dei cold fronts. Proponiamo quindi uno scenario secondo cui gli archi in Abell 2626

non siano connessi alla precessione dei getti dell'AGN, ma bensì ad attività non termica legata alla formazione ed evoluzione dei cold fronts al suo centro. In tal caso la forma peculiare degli archi sarebbe dovuta alla dinamica e alla geometria dei cold fronts, cosa che andrà esplorata con future simulazioni numeriche.
Riportiamo di seguito un breve riassunto del contenuto di ogni capitolo:

- Nel **Capitolo 1** descriviamo le proprietà generali degli ammassi di galassie, ed introduciamo Abell 2626;
- Nel **Capitolo 2** descriviamo le basi della riduzione delle osservazioni interferometriche e riportiamo i risultati della calibrazioni dei nostri dati JVLA;
- Nel **Capitolo 3** riportiamo i risultati dell'analisi delle nuove osservazioni JVLA nella banda radio e descriviamo le mappe di intensità totale e di indice spettrale;
- Nel **Capitolo 4** descriviamo gli studi morfologici e spettrali dell'emissione termica dell'ammasso sulla base delle nuove osservazioni CHANDRA;
- Nel **Capitolo 5** confrontiamo i risultati delle analisi radio e X con le previsioni del modello della precessione dei getti e proponiamo un nuovo scenario per l'origine degli archi;
- Nel **Capitolo 6** riassumiamo il nostro lavoro e proponiamo possibili sviluppi futuri;
- Nell'**Appendice A** descriviamo come abbiamo ottenuto una semplice relazione matematica fra indice spettrale ed età radiativa;
- Nell'**Appendice B** riportiamo le mappe che sono state usate per creare le mappe di indice spettrale;

Abstract

In this thesis work we carried out an accurate analysis of the new observations of the galaxy cluster Abell 2626 in the radio and X-ray band. Abell 2626 is composed by $\sim$70 galaxies, of which the most luminous in the core-dominant elliptical galaxy IC5338, that is characterized by two optical nuclei separated by 3.3 kpc. In the X-band Abell 2626 is classified as cool-core cluster, whereas its radio emission is composed by the emission of the radio galaxy associated to IC5338, which exhibits a pair of radio jets, and an extended emission located within $\sim$60 kpc from the center. This emission is characterized by the presence of a system of peculiar radio sources, the *arcs*, whose properties differs from the properties of the common cluster diffuse radio sources. In the past years, several models have been proposed to explain their origin. One of the most promising suggests that the arcs are trails of a pair of hot-spots that are moving, due to the precession of the jets of IC5338.

Our work aims to investigate the origin of the arcs. We analyzed two new JVLA observations of the cluster at 3.0 and 5.5 GHz. During the radio analysis we detected the arcs at 3.0 GHz and possible evidences for extended emission inside them at 5.5 GHz. By combining archival maps at 1.4 GHz and the new ones at 3.0 GHz, we estimated that the arcs have a spectral index α $\sim$-3. The spectral index maps have been a test for the jet-precession scenario, which predicted a spectral trend along the arcs, resulting from the deposit of the plasma at different ages. By studying the synchrotron spectrum evolution, we were able to evaluate the radiative age of the arcs, whereas, from the spectral index distribution along each arc, we estimated a time-scale Δt_{rad}=5-10 Myr for the precession of the jets . This time-scale is shorter than the precession time that we estimated from the nuclei of IC5338.

The analysis of a new CHANDRA observation of the cluster produced surprising results. We highlighted the a spatial connection between the radio arcs and a cold region inside the cluster core and, moreover, we discovered a cold front which coincides with the south-west junction of the radio arcs.

It is well known that the turbulence inside the cold fronts is able to accelerate the relativistic particles, triggering radio emission in form of mini-halos. Under certain conditions, this emission results in form of collimated steep-spectrum arcs that traces the dynamics of the cold fronts. So we proposed a scenario, in which the arcs are not related to the precession of AGN jets, but instead are produced by non-thermal processes (particle acceleration and magnetic filed amplification)

that are related to the formation and the evolution of the cold fronts in the core of Abell 2626. In this case the peculiar morphology of the arcs is the result of the dynamics of the cold fronts, that will be studied with future MHD simulations. Here we provide a brief summary of what is reported in the Chapters:

- In **Chapter 1** we describe the general properties of the galaxy clusters, and we introduce Abell 2626;
- In **Chapter 2** we describe the basics of radio interferometric observation reduction and we report the results of the calibration of our JVLA datasets;
- In **Chapter 3** we report the results of the radio analysis from the new JVLA observations, and we describe the total intensity maps and the spectral index maps;
- In **Chapter 4** we describe the spectral and morphological studies that we carried out on the thermal emission of the cluster from the new CHANDRA observation;
- In **Chapter 5** we compare the results of the radio and X-rays analysis with the predictions of the jet-precession model, then proposing a new scenario for the origin of the arcs;
- In **Chapter 6** we summarize our work and we propose future developments;
- In **Appendix A** we describe the basis of a mathematical relation between the spectral index and the radiative age;
- In **Appendix B** we report the total intensity maps that we created to compute the spectral index maps;

Contents

1 Introduction 1
- 1.1 Galaxy clusters . . . 1
- 1.2 The mass of galaxy clusters . . . 2
- 1.3 Observed properties of galaxy clusters . . . 3
  - 1.3.1 Optical properties . . . 4
  - 1.3.2 Radio properties . . . 5
  - 1.3.3 X-rays properties . . . 8
- 1.4 The galaxy cluster Abell 2626 . . . 11
  - 1.4.1 Previous studies of Abell 2626 . . . 12
  - 1.4.2 The cD galaxy IC5338 . . . 15
  - 1.4.3 The radio arcs system . . . 15
  - 1.4.4 The head-tail galaxy IC5337 . . . 18

2 Data reduction of the JVLA dataset 21
- 2.1 Radio astronomy and Interferometry . . . 21
- 2.2 Karl G. Jansky Very Large Array . . . 25
- 2.3 A-priori calibration . . . 28
  - 2.3.1 Basic steps of radio data reduction . . . 28
  - 2.3.2 Calibration of the new JVLA datasets . . . 36
- 2.4 Imaging and Self-Calibration . . . 37
  - 2.4.1 Imaging . . . 37
  - 2.4.2 Self-calibration . . . 51

3 Results of the new JVLA observations 53
- 3.1 The new JVLA maps at 3.0 and 5.5 GHz . . . 53
  - 3.1.1 5.5 GHz (C-band) maps . . . 54
  - 3.1.2 3.0 GHz (S-band) maps . . . 57
  - 3.1.3 Flux densities estimates . . . 58

3.2 Spectral Index maps 64
3.2.1 Observed flux density-spectral index trends 72

4 The thermal side of the cluster: results of the CHANDRA observation 77
4.1 CHANDRA X-ray Observatory 79
4.2 Data Reduction and Analysis techniques 79
4.2.1 Data reduction 80
4.2.2 Morphological analysis 81
4.2.3 Spectral analysis 82
4.3 Analysis of the Cluster 85
4.3.1 Spectral maps analysis 89
4.3.2 Morphological analysis 92
4.4 Analysis of the South-West Junction 93

5 On the origin of the radio arcs 109
5.1 Constraining the jet-precession model 109
5.2 A new possible scenario for the origin of the arcs? 115

6 Conclusions 119

Appendix A A simple relationship between the spectral index and the radiative age 123
A.1 Analytical derivation 123
A.2 Numerical test 125
A.3 Radiative age map 126

Appendix B Input maps for the spectral index estimates 131

List of Figures

1.1 NASA/ESA Hubble Space Telescope image of the galaxy cluster SDSS J1038+4849. The system of gravity lenses is also knows as the *smiley* complex, due to their interesting resemblance. . . . 4

1.2 Collection of clusters showing several types of radio emission, shown in contours, overlaid onto the X-ray emission, shown in colors. Clusters are (from left to right and from top to bottom) A 2219 (halo), A 2744 (halo+relic), A 115 (relic), A 754 (complex, halo plus relic), A 1664 (relic), A 548b (relic), A 520 (halo), A 2029 (mini-halo), RXCJ1314.42515 (halo plus double relics)(Feretti et al. 2012). 6

1.3 Schematic picture of AGN/ICM interaction (Churazov et al. 2001), inspired by analogy with mushroom clouds produced by powerful atmospheric explosions. The black region in the center denotes the inner radio lobes, driven by the super-massive black hole mechanical power. The circular structure is a weak shock wave produced by these inner lobes. Gray "mushrooms" correspond to the buoyant bubbles already transformed into tori, and the gray lens-shaped structures are the pancakes formed by the older bubbles 10

1.4 Archieve HST optical image of Abell 2626. 11

1.5 1.5 GHz map of A2626 Gitti et al. (2004). The resolution is 4.5"x3.9". The rms level is 0.03 mJy/beam. The map shows the emission from the core and a couple of radio bars. 12

1.6 VLA 1.4 image of A2626. The RMS level is 0.01 mJy/beam and the resolution is 1.7"x1.6" (Gitti 2013) 13

1.7 GMRT 610 MHz image of A2626. The RMS level is 0.08 mJy/beam and the resolution is 8.5"x4.4" (Kale and Gitti 2017) 14

1.8 Overlay of *Left:* CHANDRA image of the core of IC5338 with the VLA 1.4 GHz contours (Gitti 2013); *Right:* HST image of the double core of IC5338 with the 1.4 GHz contours (Gitti 2013); . . 15

1.9 Sketch of the jet-precession model. In this picture, that preceded the discovery of the fourth arc (2017), the north-south arcs and the western arc are thought to be originated by two different couple of jets. 17

2.1 Atmospheric windows of the astrophysical observations. 22

2.2 How a typical baseline works: the signal of the wavefront is collected by the antennae and the signal of each antenna is elaborated to reduce the noise, then it is composed in a single visibility $V_{ij}(u, v)$ by the Correlator (Middelberg and Bach 2008). 24

2.3 the Karl G. Jansky Very Large Array 26

2.4 Resolution power of each receiver band of the JVLA in the four configurations. 27

2.5 Flow diagram of a Radio dataset calibration 31

2.6 Amplitude vs UVwave (Top) and Amplitude vs Frequency (Bottom) plot of the model of 3C48. the flux density calibrator, that we used for the calibration of the C-band dataset. 33

2.7 UVplane coverage of the observations in C (top) and S (bottom) band. 38

2.8 Amplitude vs Frequency plot for the Flux Calibrator 3C48 at 5.5 GHz before (top) and after (bottom) the calibration. Notice the change in amplitude level. 39

2.9 Amplitude vs UVdist plot for the Flux Calibrator 3C48 at 5.5 GHz before (top) and after (bottom) the calibration. Notice the change in amplitude level and the shape of the distribution, which resemble the theorical model in Fig. 2.6. 40

2.10 Amplitude vs Frequency plot for A2626 at 5.5 GHz before (top) and after (bottom) the calibration. Notice the change in amplitude level and the frequency chunk that we removed due to the presence of RFI. 41

2.11 Amplitude vs UVdist plot for A2626 at 5.5 GHz before (top) and after (bottom) the calibration. Notice the change in amplitude level and the frequency chunk that we removed due to the presence of RFI. 42

2.12 Amplitude vs Frequency plot for A2626 at 3.0 GHz before (top) and after (bottom) the calibration. Notice the change in amplitude level and the frequency chunk that we removed due to the presence of RFI. It is important to notice that, even if the RFI at 2.3 GHz (blue) looks like its is dominating the signal, each one of the other spectral windos had a signal above 10 mJy before the editing. 43

2.13 Amplitude vs UVdist plot for A2626 at 3.0 GHz before (top) and after (bottom) the calibration. Notice the change in amplitude level. 44

2.14 Some examples of what happen when the clean goes wrong. The top panel is the result of wrong setting of `MULTISCALE`, and the bottom one is an attempt to combine the `nterms 2` with the `NATURAL` weighting: the mean flux density of the whole map is over 2000 Jy/beam, which means that the clean had amplified tremendously the real amplitude of the signal. 49

2.15 Result of a `ROBUST 0` clean with `nterms 1` (Left) and `nterms 2` (Right). The `nterms 2` clean improves dramatically the removal of the Beam artifacts, especially around the bright source located at North-West. The absence of these artifact improves, in turn, the sensitivity of the map, making the diffuse emission of A2626 more clear. 50

3.1 5.5 GHz image obtained by setting `UNIFORM`, `nterms=1`. The beam size is 2.8"x2.7". The RMS is 16.1 μJy beam^{-1} and the contours levels are -3,3,6,12,24·RMS. 55

3.2 5.5 GHz image obtained by setting `ROBUST 0`, `nterms=2`. The beam size is 3.2"x2.8". The RMS is 8.0 μJy beam^{-1} and the contours levels are -3,3,6,12,24·RMS. 56

3.3 5.5 GHz image obtained by setting `NATURAL`, `nterms=1`, `UVTAPER=[0,20]`. The beam size is 4.9"x4.4". The RMS is8.6 μJy beam^{-1} and the contours levels are -3,3,6,12,24·RMS. 56

3.4 Comparison of the diffuse emission at 5.5 GHz (white) and 1.4 GHz (magenta). 57

3.5 3.0 GHz image obtained by setting `UNIFORM`, `nterms=1`. The beam size is 7.5"x8.5". The RMS is 40.1 μJy beam^{-1} and the contours levels are -3,3,6,12,24·RMS. 58

3.6 3.0 GHz image obtained by setting `ROBUST 0`, `nterms=2`. The beam size is 8.7"x5.8". The RMS is 20.4μJy beam^{-1} and the contours levels are -3,3,6,12,24·RMS. The purple contours are the 3σ level of the 1.4 GHz map by Gitti (2013) 60

3.7 3.0 GHz image obtained by setting `NATURAL`, `nterms=1` and `UVTAPER=[0,20]`. The beam size is 13.1"x8.5". The RMS is 18.5 μJy beam^{-1} and the contours levels are -3,3,6,12,24·RMS. In black there are the vectors of the polarized emission. 61
3.8 Radio spectra of the components reported in Tab. 3.3 63
3.9 *Top:* 1.4-3.0 GHz spectral index map.*Bottom:* Relative error map 66
3.10 *Top:* 1.4-3.0 GHz spectral index map.*Bottom:* Relative error map 67
3.11 *Top:* 1.4-5.5 GHz spectral index map with 1.4 GHz contours.*Bottom:* Relative error map 68
3.12 *Top:* 1.4-4.8 GHz spectral index map with 1.4 GHz contours.*Bottom:* Relative error map 69
3.13 *Top:* 1.4-5.5 GHz spectral index map.*Bottom:* Relative error map 70
3.14 *Top:* 3.0-5.5 GHz spectral index map.*Bottom:* Relative error map 71
3.15 Sampling method used to produce the graphics in Fig. 3.16-3.18 73
3.16 Spectral index and flux trend along the arc North. On the x-axis is shown the sampling numeration, on the left y-axis the flux scale and on the right y-axis the spectral index scale. The values are measured on: *Top:* `NATURAL` maps; *Bottom:* `ROBUST 0` maps. . . 74
3.17 Spectral index and flux trend along the arc South. On the x-axis is shown the sampling numeration, on the left y-axis the flux scale and on the right y-axis the spectral index scale. The values are measured on: *Top:* `NATURAL` maps; *Bottom:* `ROBUST 0` maps. . . 75
3.18 Spectral index and flux trend along the arc West. On the x-axis is shown the sampling numeration, on the left y-axis the flux scale and on the right y-axis the spectral index scale. The values are measured on: *Top:* `NATURAL` maps; *Bottom:* `ROBUST 0` maps. . . 76

4.1 Images of the two nuclei of the cD galaxy IC 5338 in Abell 2626. All images show the same FOV of 30"x30". Top left: Optical image from HST archive. The image was taken with WFPC2 using the F555W filter. The two green circles, included in the other panels, are centered at the two optical nuclei observed by HST. Top right: Background-subtracted, exposure-corrected, adaptively smoothed CHANDRA image in the 0.3 -10 keV band. The image was smoothed to a signal-to-noise ratio of 3. The color represents the X-ray intensity from high (white-yellow) to low (dark blue). Bottom left: Raw CHANDRA image in the soft (0.3-2 keV) band. Two intensity peaks can be identified. Bottom right: Raw CHANDRA image in the hard (2 -10 keV) band. Only the southwestern nucleus corresponds to the peak in the hard band (Wong et al. 2008). 78

4.2 Renamed the CHANDRA X-ray Observatory after launch, the image on the left shows AXAF during pre-launch testing. The image on the right shows the instruments onboard the observatory. Credit: NASA 79
4.3 Flow chart of the code developed to perform the spectral analysis. 84
4.4 0.5-2 keV smoothed raw image of A2626 made from the CHANDRA dataset. 85
4.5 X-ray emission of IC5337 in the 0.5-2 keV energy band. In white are overlaid the contours of its radio emission at 1.4 GHz (Gitti 2013). 86
4.6 The azimuthally-averaged radial profiles inside 170 kpc *Top:* projected azimuthally-averaged radial profiles *Bottom:* de-projected azimuthally-averaged radial profiles. 87
4.7 Spectrum of the emission of A2626 inside R_3 in the energy range 0.5-7 keV and residual of the fit with the `WABS·(APEC+MKCFLOW)`. The best fit has χ^2_r=1.2. We removed the point sources in IC5338 and IC5337. 88
4.8 Azimuthally-averaged SB profile in arbitrary unit of the cluster, extracted from circular annulus inside ~100 kpc. We report in red the result of the double β-model fit. In the table are reported the best-fit parameters. 89
4.9 Temperature maps of A2626, courtesy of Dr. O'Sullivan. In green are overlaid the contours of the 1.4 GHz map of radio emission from Gitti (2013). The values have a relative error of $\sim 10\%$ . . 90
4.10 Pressure maps of A2626, courtesy of Dr. O'Sullivan. In green are overlaid the contours of the 1.4 GHz map of radio emission from Gitti (2013). The values have a relative error of $\sim 10\%$ 91
4.11 Overlay of the residual of the 2-D fit and the contours of the radio emission at 1.4 GHz from Gitti (2013). Positive values are in white-orange scale, whereas the zeros are in blue and the negative ones are in black. In the table are reported the parameters of best-fit. The values differ from the fit of the SB profile due to a different behavior of the 2D model with respect to the 1D model. The emission of IC5337 has been masked with elliptical region because it was not related to the cluster thermal emission. 94
4.12 The result of the Gaussian filtering: *Top-left:* 1σ filtering; *Top-right:* 4σ filtering. In green are reported the contours of the radio emission at 1.4 GHz (Gitti 2013); *Bottom-left:* 8σ filtering; *Bottom-right:* multi-scale filtering. 95
4.13 The region where we performed the spectral analysis of the S-W junction. In green are overlaid the 1.4 GHz radio contours. 96

4.14 The profiles extracted from Fig.4.13. The region has been divided in 7 annuli *Top:* projected profile *Bottom:* de-projected profile. . 97

4.15 The profiles extracted from Fig.4.13. The region has been divided in 8 annuli *Top:* projected profile *Bottom:* de-projected profile. . 98

4.16 The profiles extracted from Fig.4.13. The region has been divided in 9 annuli *Top:* projected profile *Bottom:* de-projected profile. . 99

4.17 Sampling system that we adopted in the SB profiles analysis. . . 100

4.18 Surface brightness profile from each sub-sector of the 0.5 Sequence. The SB is expressed in arbitrary units. 101

4.19 Surface brightness profile from each sub-sector of the 0.3 Sequence. The SB is expressed in arbitrary units. 102

4.20 Surface brightness profile from each sub-sector of the 0.25 Sequence. The SB is expressed in arbitrary units. 103

4.21 Profile of *0.3-1*. Front radius=29.7 kpc, Density jump=$1.27^{+0.22}_{-0.18}$ 104

4.22 Profile of *0.25-1*. Front radius=29.5 kpc, Density jump=$1.31^{+0.27}_{-0.21}$ 104

4.23 Profile of *0.3-3*. Front radius=26.3 kpc, Density jump=$1.36^{+0.16}_{-0.14}$ 104

4.24 Surface brightness profiles fitted with the broken-power law model.104

4.25 *Blue:* Image of the thermal X-rays emission between 0.5-7.0 keV *Red:* Non-thermal emission at 1.4 GHz from Gitti (2013) *Green:* regions where we extracted the profile reported in Fig. 4.26 and Fig. 4.27. The discontinuities observed in the fits, that we have highlighted in yellow on each sector, follow the shape of the radio emission. 105

4.26 Profiles of the thermal properties across the jump at ∼29.5 kpc. *Top:* Projected profiles; *Bottom:* De-projected profiles 106

4.27 Profiles of the thermal properties across the jump at ∼26.3 kpc. *Top:* Projected profiles; *Bottom:* De-projected profiles 108

5.1 Radiative Age map (top) and error map (bottom) of A2626, obtained from the spectral index map in Fig. 3.9. The parameters are: ν_1=1.4 GHz, ν_2=3.0 GHz, R=2.14, z=0.0553, H_{eq}=2.08 μG, H_{CMB}=3.61 μG, and Γ=2.4. The black regions are upper limit to the radiative age. 113

5.2 Radiative Age map (top) and error map (bottom) of A2626, obtained from the spectral index map in Fig. 3.9 in condition of Equipartition. The parameters are: ν_1=1.4 GHz, ν_2=3.0 GHz, R=2.14, H_{eq}=12.1 μG, H_{CMB}=3.61 μG and Γ=2.4. The black regions are upper limit to the radiative age. 114

5.3 Results of the simulations of the particles acceleration (ZuHone et al. 2013). *Top:* Projected gas temperature maps with radio contours overlaid at several epochs for the frequencies 153, 327, and 1420 MHz in the x-projection. The radio filaments in the bottom-right panel resemble the radio arcs; *Bottom:* Magnetic field strength for several epochs. The distribution follows the morphology of the cold fronts. 117

A.1 Result of the numerical integration *Blue:* the relation between the observed spectral index between 1.4 and 3.0 GHz an the estimated age of the electron population; *Red:* the estimated position of the ν_{br} that produces the observed spectral index 127
A.2 Synchrotron spetrum computed by numerical integration of Eq. A.5 and the analytical approximation Eq. A.7 128
A.3 The Spectral index vs k_1, with Γ=2.4 and a ratio R=2.14 between the observed frequencies, computed from the emissivity spectra reported in Fig. A.2 128
A.4 Spectral Index vs Break frequency, with Γ=2.4, R=2.14 and ν_1^{obs}=1.4 GHz. 129
A.5 Spectral index vs Radiative time, with Γ=2.4, z=0.053, R=2.14 and ν_1^{obs}=1.4 GHz. 129

B.1 1.4 GHz image obtained by setting `NATURAL`, `nterms=1`, `UVRANGE=0-40`. The beam size is 13.1"x8.5". The RMS is 29.4 μJy beam^{-1}. . . . 132
B.2 3.0 GHz image obtained by setting `NATURAL`, `nterms=1`, `UVRANGE=0-40`. The beam size is 13.1"x8.5". The RMS is 20.5 μJy beam^{-1}. . . . 132
B.3 1.4 GHz image obtained by setting `ROBUST 0`, `nterms=2`, `UVRANGE=0-40`. The beam size is 8.7"x5.8". The RMS is 21.9 μJy beam^{-1}. . . . 133
B.4 3.0 GHz image obtained by setting `ROBUST 0`, `nterms=2`, `UVRANGE=0-40`. The beam size is 8.7"x5.8". The RMS is 20.8 μJy beam^{-1}. . . . 133
B.5 1.4 GHz image obtained by setting `ROBUST 0`, `nterms=2`, `UVRANGE=0-68`. The beam size is 3.2"x2.9". The RMS is 15.5 μJy beam^{-1}. . . . 134
B.6 5.5 GHz image obtained by setting `ROBUST 0`, `nterms=2`, `UVRANGE=0-68`. The beam size is 3.2"x2.9". The RMS is 8.3 μJy beam^{-1}. 134
B.7 1.4 GHz image obtained by setting `ROBUST 0`, `nterms=2`, `UVRANGE=0-170`. The beam size is 1.6"x1.5". The RMS is 12.3 μJy beam^{-1}. . . . 135
B.8 4.8 GHz image obtained by setting `ROBUST 0`, `nterms=2`, `UVRANGE=0-170`. The beam size is 1.6"x1.5". The RMS is 12.4 μJy beam^{-1}. . . . 135
B.9 5.5 GHz image obtained by setting `NATURAL`, `nterms=1`, `UVRANGE=0-40`. The beam size is 13.1"x8.5". The RMS is 8.1 μJy beam^{-1}. . . . 136

List of Tables

1.1 Typical properties of groups and clusters of galaxies (Bahcall 1996) 5
1.2 Summary of the radio properties of the arcs (Kale and Gitti 2017). 16

2.1 New JVLA data analysed in this work (project code:14B-022 PI M.Gitti) 36
2.2 Improvement of the self-calibration on the dataset. We report the RMS values after every cycle of self-cal. The RMS level of the S-band is high because the imaging between each cycle was developed in `nterms=1` to reduce the computation time: for this reason the RMS level is affected by the secondary lobes of the background sources. 51

3.1 List of Total Intensity maps 54
3.2 Flux Density values for each map. 59
3.3 Synchrotron spectra of the radio sources of A2626 62
3.4 Monochromatic radio power of the radio sources of A2626 . . . 62
3.5 Estimated properties of the residual diffuse emission 64
3.6 List of spectral index maps 65

4.1 New CHANDRA data analyzed in this work (PI C. Sarazin) . . . 80
4.2 Summary of the analysis of the discontinuities 107

B.1 Input maps for each spectral index map 131

Chapter 1

Introduction

1.1 Galaxy clusters

Historically, the first galaxy cluster was discovered as an accumulation of nebulae by Charles Messier in 1781 (Messier 1781), as documented after the entry of M91 in his catalog. He noted that 16 and thus unusually many "nebulae" of his catalog are situated in this small region in the sky at the north-western edge of Virgo and overlapping to Coma Berenices. At that time, the concentration of "nebulae" in this region was not understood and related to the proximity to the North Galaxctic Pole. It was Harlow Shapley and Adelaide Ames who in 1926 first used the term "cluster" ("of bright spiral nebulae") for this accumulation of galaxies, and determined data (brightness, color, diameter) for 103 of them. They estimated a mean distance of 10 million light-years for these "nebulae".
Nowadays we know that galaxy clusters, and the filaments that connect them, are the largest structures in the present Universe in which the gravitational force, due to the matter over densities, overcomes the cosmological expansion of the Universe. They extend over 1-3 Mpc regions and have typical total masses in the range 10^{14} – 10^{15} $M_{\odot}$. This mass is mostly in the form of dark matter (DM) (80-85%). The remaining 15-20% is baryonic matter, in particular 2-5% is in the form of galaxies and the rest 13-15% in the form of hot (T = 10^8 K) and tenuous gas (n_{gas} = 10^{-2}-10^{-4} cm^{-3}), the Intra Cluster Medium (ICM) (e.g. Bykov et al. 2015).
According to the observations, the galaxy cluster have been classified in several ways. Abell (1958) introduced a first classification based on the the approximate number of galaxies composing the cluster. Clusters were divided into six "richness group", from "Group 0" to "Group 5". Abell also divided the galaxy clusters in regular and irregular. The first ones are evolved, virialized and symmetric sys-

tem. The second ones are dynamically disturbed objects, showing asymmetric morphology with the presence of substructures. The recent X-rays observations, made with CHANDRA and XMM-Newton, reinforce the validity of the dynamical classification. According to their surface brightness distribution, the galaxy cluster are classified in *cool-core* cluster and *merging* cluster. The cool-core cluster exhibit a peak of the surface brightness in the center and are thought to be relaxed structures. On the other hand, merger cluster are characterized by an irregular distribution of the surface brightness.

In the current paradigm of structure formation, clusters are thought to form via a hierarchical sequence of mergers and accretion of smaller systems driven by the dark matter (DM) that dominates the gravitational field. Galaxy clusters are therefore reliable crossroads of cosmology and astrophysics. One the one hand, they can be used as cosmological probes to study the physics that governs the dynamics of the large scale structures of the Universe. On the other hand, they are laboratories to study the physics of baryons.

1.2 The mass of galaxy clusters

Galaxy clusters are the most massive systems in the Universe and there are several methods to estimate their masses. From an historical point of view, the first method applied was based on the dynamics traced by member galaxies (Zwicky 1933). The mass estimated from the optical luminosity alone was not enough to justify the observed galaxy velocities, therefore Zwicky argued that the cluster must host another kind of matter that does not interact with the electromagnetic waves. This was the first probe of the existence of the DM.

Another method to estimate the cluster mass assumes the condition of hydrostatic equilibrium, that determines the balance between the pressure force and gravitational force:

$$\bigtriangledown p_{gas} = -\rho_{gas} \bigtriangledown \phi \tag{1.1}$$

where $p_{gas} = \rho_{gas} kT/\mu m_p$ and ρ_{gas} are pressure and density of the gas, respectively and $\bigtriangledown\phi$ is the gravitational potential. Under the assumption of spherically symmetric gas distribution, it is possible to derive the expression for the $M(r)$ inside the radius r as:

$$M(r) = -\frac{rkT}{G\mu m_p}\left(\frac{\mathrm{d}ln\rho_{gas}(r)}{\mathrm{d}ln(r)} + \frac{\mathrm{d}lnT(r)}{\mathrm{d}ln(r)}\right) \tag{1.2}$$

where the temperature radial profile $T(r)$ is measurable directly through the X-ray spectroscopy of the cluster and the density radial profile $\rho_{gas}(r)$ is estimated by fitting a β-model. This model was proposed by Cavaliere and Fusco-Femiano (1976), who estimated that the density profile of a spherical isothermal distribution of gas may be written as

$$\rho_{gas}(r) = \rho_0 \left[1 + \left(\frac{r}{r_{core}}\right)^2\right]^{-\frac{3\beta}{2}} \tag{1.3}$$

and the surface brightness profile observed at a projected radius b, $\Sigma(b)$, is in the form:

$$\Sigma(b) = \Sigma_0 \left[1 + \left(\frac{b}{r_{core}}\right)^2\right]^{\frac{1}{2}-3\beta} \tag{1.4}$$

where parameter β is defined as:

$$\beta = \frac{\sigma_r^2}{kT/\mu m_p} \tag{1.5}$$

where σ_r is the line–of–sight velocity dispersion, and represents the ratio of specific kinetic energies of galaxies and gas. The parameter β is evaluated by fitting the surface brightness radial profile, then it is involved to estimate the density profile. In the cool-core clusters the β-model is found to be a poor description of the cluster surface brightness profile, because they do not fully satisfy the isothermal hypothesis. The density profile of these cluster is well represented by the *double* β-model, that assumes that the ICM is composed by two plasma with different temperature.

A third independent method is based on weak and/or strong gravitational lensing. Observations of weak lensing aim at reconstructing the cluster mass distribution from the weak ellipticity that the cluster gravity induces on faint background galaxies. A simple spherical lensing model provides a good estimate of the cluster mass within the distance between the arc-like image and the cluster centre.

.

1.3 Observed properties of galaxy clusters

The physics of the galaxy clusters is very complex. The most recent observations have shown that it is regulated by yet poorly understood non-gravitational processes beyond simple gravity, gas dynamic and radiative cooling usually considered in the standard cold dark matter cosmological scenario (e.g. McNamara and Nulsen (2007), Bykov et al. (2015)). We briefly summarize here the main properties of galaxy clusters observed in radio, optical and X-rays bands.

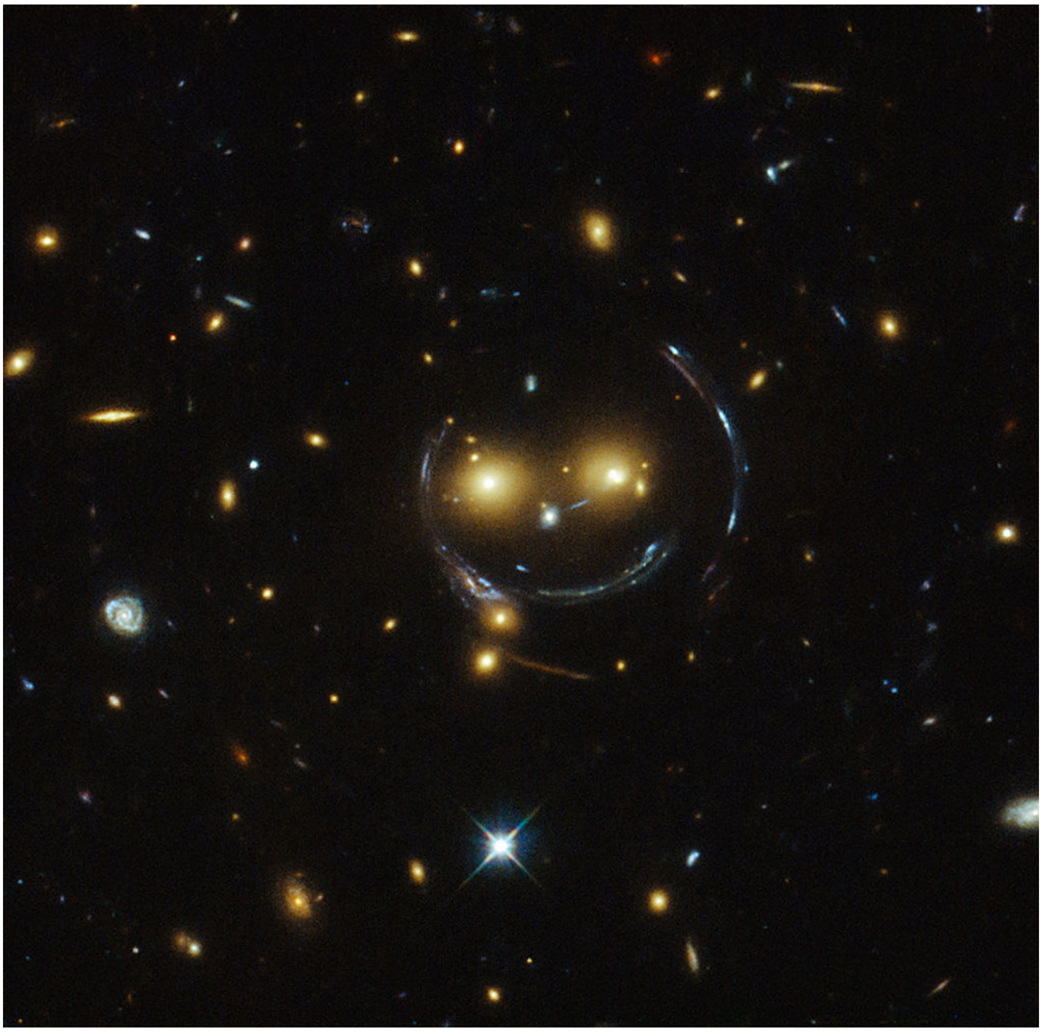

Figure 1.1: NASA/ESA Hubble Space Telescope image of the galaxy cluster SDSS J1038+4849. The system of gravity lenses is also knows as the *smiley* complex, due to their interesting resemblance.

1.3.1 Optical properties

The optical emission of a cluster comes mainly from the galaxies and, thus, it is produced by the thermal Black Body and Recombination mechanisms. The optical classification divides the cluster in *rich* clusters and *groups*. This classification, that was introduced by Abell (1958) based on the number of galaxies of each cluster, has been validate by the observations. Rich clusters and group are intrinsically different (e.g. Tab. 2.1), and this difference is used as a constrain for the cosmological models of structure formation.

The emission lines of the galaxies allow the estimate of the redshift of the clusters, thus also their distance and their radial velocity. These information are the

Property	Rich clusters	Poor clusters (groups)
Richness	30-300 galaxies	3-30 galaxies
Radius	(1-2) h^{-1} Mpc	(0.1-1) h^{-1} Mpc
Radial velocity dispersion	400-1400 km s^{-1}	100-500 km s^{-1}
Radial vel. disp. (median)	$\sim$ 750 km s^{-1}	$\sim$ 250 km s^{-1}
Mass (r $\leq$ 1.5 h^{-1} Mpc)	$(10^{14} - 2 \cdot 10^{15})h^{-1}\ M_\odot$	$(10^{12.5} - 10^{14})h^{-1}\ M_\odot$
Luminosity (B)	$(6 \cdot 10^{11} - 6 \cdot 10^{12})h^{-2}\ L_\odot$	$(10^{10.5} - 10^{12})\ h^{-2}\ L_\odot$
Mass-to-light Ratio	$300hM_\odot/L_\odot$	$200hM_\odot/L_\odot$
Cluster number density	$(10^{-5} - 10^{-6})h^3Mpc^{-3}$	$(10^{-3} - 10^{-5})h^3Mpc^{-3}$
Correlation scale	(22$\pm$4)h^{-1} Mpc	(13$\pm$2)h^{-1} Mpc

Table 1.1: Typical properties of groups and clusters of galaxies (Bahcall 1996)

base of large optical catalogs of clusters, that are the primary method to measure many cosmological parameters, as the mass density parameter Ω_m and the amplitude of the perturbation spectrum σ_8 (Oukbir and Blanchard 1992). Dynamical studies, based on optical surveys of galaxy cluster, led to the discovery of the *superclusters* of galaxies (Tully et al. 2014).

Optical observations of galaxy clusters are also the primary field of study of the Gravitational Lensing effect (Kneib and Natarajan 2011). The DM halo creates a converging lens for the light which comes from sources that are located behind the cluster in thee line-of-sight. The lensed sources are deformed, and the geometry of the distortion depends on the mass distribution of the DM halo (e.g. Fig.1.1). Due to its direct dependence to the mass of the cluster, the gravitational lensing is a useful tool to estimate it. Moreover, the lensing magnifies the brightness of the lensed sources, allowing us to observe high redshift objects that will not be detected otherwise.

1.3.2 Radio properties

In the recent years, radio observations have revealed that a fraction of galaxy cluster hosts diffuse synchrotron emission on cluster scale. The discovery of radio sources not associated with any individual galaxy (e.g. Fig. 1.2) proves the presence of non-thermal components, such as relativistic particles and magnetic fields, mixed with the thermal ICM on spatial scale that are comparable to the cluster size.

So far, cluster magnetic field properties have been studied from Faraday rotation measure (RM) of polarized sources in or behind galaxy cluster. The rotation of the polarization angle, $\Delta\theta$, takes place when an electromagnetic wave passes

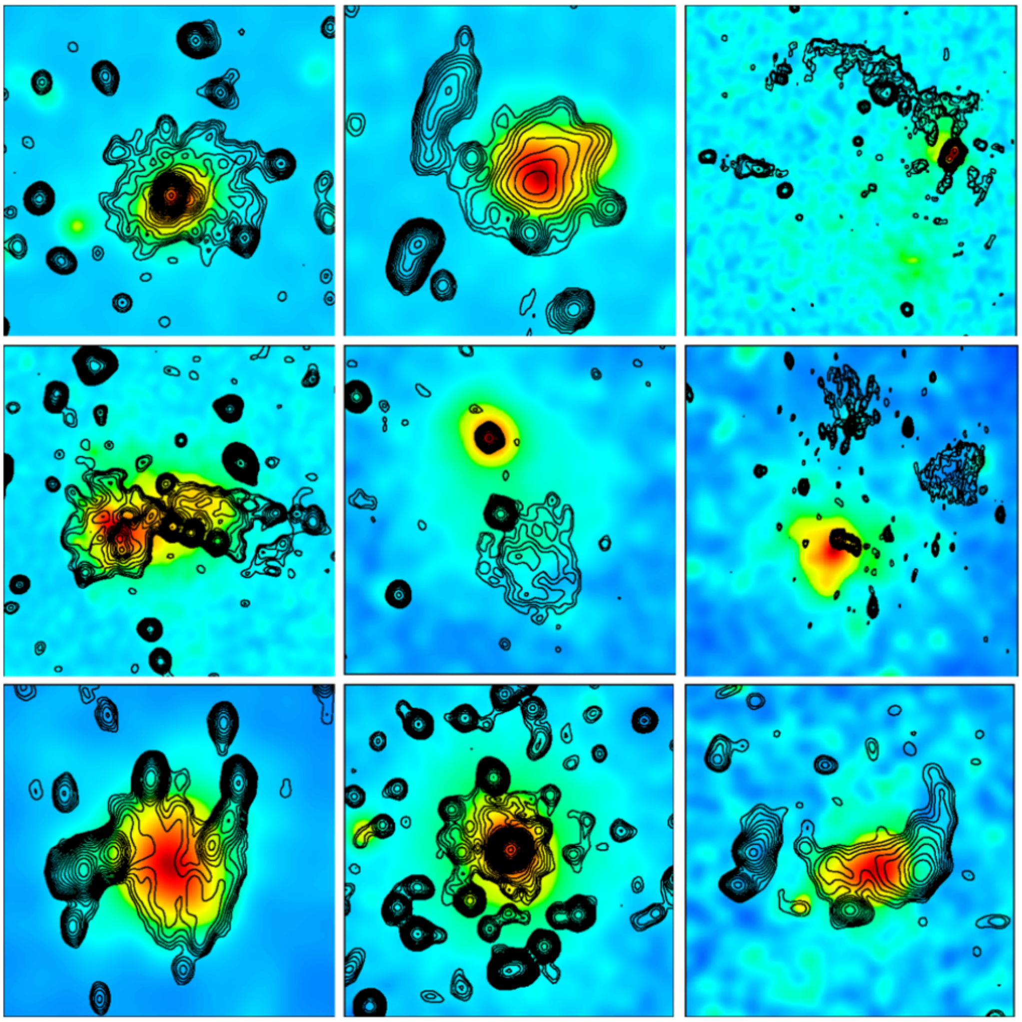

Figure 1.2: Collection of clusters showing several types of radio emission, shown in contours, overlaid onto the X-ray emission, shown in colors. Clusters are (from left to right and from top to bottom) A 2219 (halo), A 2744 (halo+relic), A 115 (relic), A 754 (complex, halo plus relic), A 1664 (relic), A 548b (relic), A 520 (halo), A 2029 (mini-halo), RXCJ1314.42515 (halo plus double relics)(Feretti et al. 2012).

through a magnetized plasma, and may be written as:

$$\Delta\theta = RM \cdot \lambda^2 \tag{1.6}$$

where RM is defined as:

$$RM = 812 \int_0^L \frac{n_e}{[\mathrm{cm}^3]} \frac{H}{[\mu\mathrm{G}]} \frac{dl}{[\mathrm{kpc}]} \text{ rad m}^2 \tag{1.7}$$

were L is the depth of the magnetized plasma, H is the magnetic field strength and n_e is the electron density of the plasma. Faraday rotation reveals magnetic field strengths of the order of few μG in cluster cores and suggests that the field intensity decreases with cluster radius (e.g. Carilli and Taylor 2002).

According to their morphology and location in the cluster, cluster-scale radio sources are classified as radio relic, radio halos and radio mini-halos (MH) (Feretti et al. 2012). Relics are elongated and arc-shaped synchrotron sources located in the peripheries of dynamically disturbed clusters. They usually show an increasing spectral index trend along their width, and an high fraction of polarized emission. Radio relics are also unique probes of the properties of magnetic fields in the outskirts of galaxy cluster. Halos and mini-halos instead are roundish radio sources located in the cluster central regions. The two classes differ in size and in the dynamical properties of the hosting clusters. The halo are located in the center of dynamically disrupted clusters, whereas mini-halos are detected only in relaxed, cool-core clusters, where recent major merger activity has not taken place.

The main problem concerning the diffuse radio sources is the *slow diffusion problem*. The diffusion time necessary for the electrons to cover the cluster scales ($\tau_{diff} >> 10^9$ yr) is much larger than their radiative life-time ($\tau_{rl} \leq 10^8$ yr). This short life-time requires that the emitting particles are continuously accelerated or generated in-situ in the ICM. According to the most accepted view, the relativistic electrons are continuously re-accelerated by manifold mechanisms associated with turbulence in the ICM (re-acceleration or leptonic models)(e.g. Brunetti and Jones 2014). The current leading scenario for the origin of the relic is based on diffusive shock acceleration theory, although several aspects of their formation mechanism are still unclear. The connection between radio relics and shocks is supported by several observational facts, including the coincidence between relics and shocks identified in the X-rays. Giant and mini halos radio emission is though to be triggered by the turbulence acceleration of the particles. According to the merger theories, giant halo turbolence is activated by the residual gravitational energy released after these events (a galaxy cluster merger is one of the most energetic phenomenon of the Universe, it is able to release up to 10^{60} erg of energy), instead the origin of mini-halos is still debated (e.g.

Gitti et al. (2002), ZuHone et al. (2011) for the leptonic model, Pfrommer and Enßlin (2004) for the adronic models).

The radio emission of galaxy cluster is composed also by the emission of the individual galaxies. The cluster radio galaxy show peculiar properties related to the interaction with the ICM. It is found that $\sim 71\%$ of the core dominant (cD) galaxies host an active galactic nucleus (AGN) (e.g. Burns (1990),Mittal et al. (2009)) and the distribution of the ICM is able to drive the diffusion of the relativistic plasma outflow (e.g. Nulsen et al. 2002). Moreover, galaxy cluster host the *head-tail radio galaxies*. These radio galaxies are characterized by a curved shape of the radio emission, result of the pressure of the ICM to the jets (e.g. Rudnick and Owen 1976).

In the whole work we define the synchrotron spectrum as $S \propto \nu^{\alpha}$.

1.3.3 X-rays properties

The first all sky survey in X-ray band with $Uhuru$ satellite revealed that the majority of galaxy clusters are X-ray luminous objects, with X-ray luminosities $L_X = 10^{43}$ – 10^{46} erg/s. It was found that the detected X-rays could not be associated with compact sources, but instead it comes from hot diffuse plasma. The ICM emits primarily by Thermal Bremsstrahlung emission from the diffuse plasma, which fills the deep potential well of the dark matter, that is heated to a temperature of $\sim 10^8$ keV by the gravitational collapse during the cluster formation (Felten et al. 1966).

The frequency-integrated total emissivity at a temperature T is expressed as:

$$J_X(T) = \Lambda(T) n_e n_p \text{ erg s}^{-1} \text{ cm}^{-3} \tag{1.8}$$

where $\Lambda(T)$ is the *cooling function*, that express the cooling of a plasma by thermal radiation. The general behavior of that function was calculated and discussed by Sutherland and Dopita (1993).

The X-ray emission represents the principal loss of energy of the ICM. The time scale of the energy loss, which correspond to a cooling of the ICM, is represented by the *cooling time* t_{cool} as:

$$t_{cool} = \frac{H_v}{\Lambda(T) n_e n_p} = \frac{\gamma}{\gamma - 1} \frac{kT}{\mu X n_e \Lambda(T)} \tag{1.9}$$

where γ is the adiabatic index, μ the mean molecular weigh and X is the Hydrogen mass fraction (e.g. Gitti et al. 2012). In the core of cool-core clusters the cooling time is shorter than 7.7 Gyr inside the cluster radius, thus meaning that the thermal emission is efficient. For that reason they show a strongly peaked surface brightness distribution. As the temperature decreases in these regions, the

density is forced to rise to balance the pressure of the ICM, causing a sub-sonic flow of cold matter called *cooling flow* (e.g. Fabian et al. 1994). This continuously accretion of cold matter would increase dramatically the star formation in the central galaxy of a cluster. However, the observations of cooling flow clusters failed to observe the predicted star formation rate, which opened a debate about the mechanism that could quench the cooling mechanism. Nowadays the most accepted explanation is the *AGN Feedback*: the presence of large reserves of cold matter could trigger the AGN activity of the cD galaxy, whose energy outflow is able to heat the ICM and contrast the cooling (e.g. Peterson and Fabian (2006), McNamara and Nulsen (2007), McNamara and Nulsen (2012)).
With the the high-resolution observation of X-rays emission, it became clear that the central AGN have a profound, persistent effect on the ICM. The most typical configuration is for jets from the cD elliptical of a cluster to extend outwards in a bipolar flow, inflating lobes of radio-emitting plasma (e.g. Fig. 1.3). These lobes push aside the X-ray emitting gas of the cluster atmosphere, excavating depressions in the ICM which are detectable as apparent 'cavities' in the X-ray images. It has been estimated that the mechanical energy released fromt these interactions is enough to compensate the cooling flow (e.g. Gitti et al. 2012).

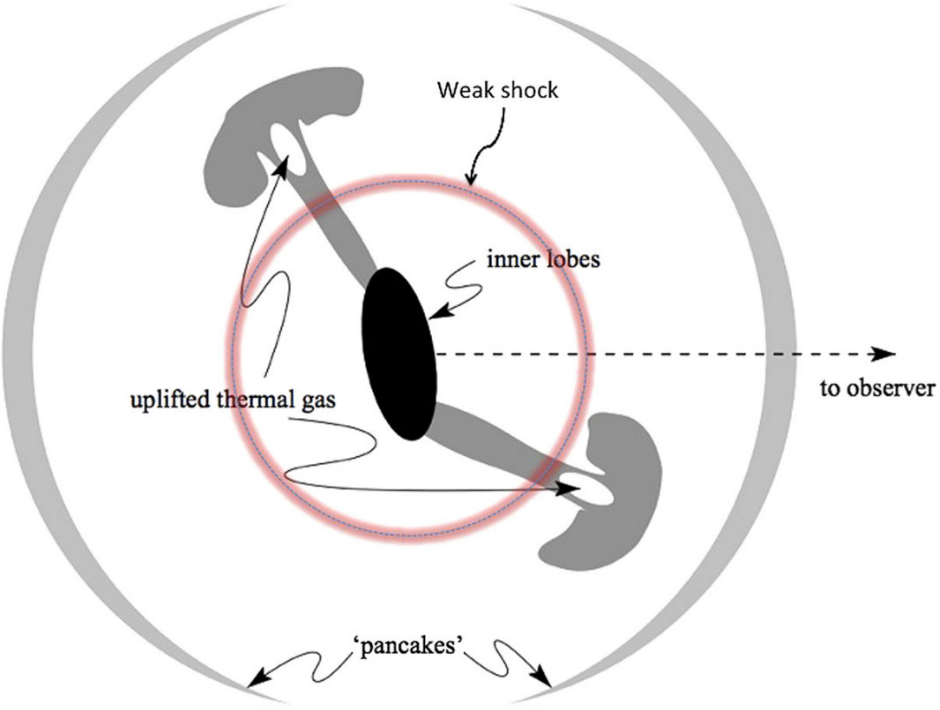

Figure 1.3: Schematic picture of AGN/ICM interaction (Churazov et al. 2001), inspired by analogy with mushroom clouds produced by powerful atmospheric explosions. The black region in the center denotes the inner radio lobes, driven by the super-massive black hole mechanical power. The circular structure is a weak shock wave produced by these inner lobes. Gray "mushrooms" correspond to the buoyant bubbles already transformed into tori, and the gray lens-shaped structures are the pancakes formed by the older bubbles

1.4 The galaxy cluster Abell 2626

This thesis work consists of an accurate study of the inner region of Abell 2626 (A2626) (e.g. Fig. 1.4), a low-redshift (z=0.0553 Struble and Rood 1999), regular, poor cluster (Mohr et al. 1996). The cluster is found at RA 23h36m30s DEC +21d08m33s. With H_0=70 km s^{1}Mpc^1, and $\Omega_M = 1 - \Omega_\Lambda = 0.3$, the luminosity distance of A2626 is 246.8 Mpc and 1 arcsec corresponds to 1.1 kpc. It is part of the Perseus-Pegasus super cluster, a filament of galaxy clusters extending to ~300 Mpc (Einasto et al. 2001). A2626 has a mass of $9 \cdot 10^{14}$ $M_\odot$h^{-1} and a virial radius of 1.64 Mpc (Mohr et al. 1996).
A2626 is a cool-core cluster with an estimated cooling flow of ~2 $M_\odot$/yr and X-ray luminosity about $1.9 \cdot 10^{44}$ erg/s (Wong et al. 2008). It hosts 70 galaxies, the most luminous are IC5338, the cD galaxy, and IC5337, a head-tail radio galaxy located to west.

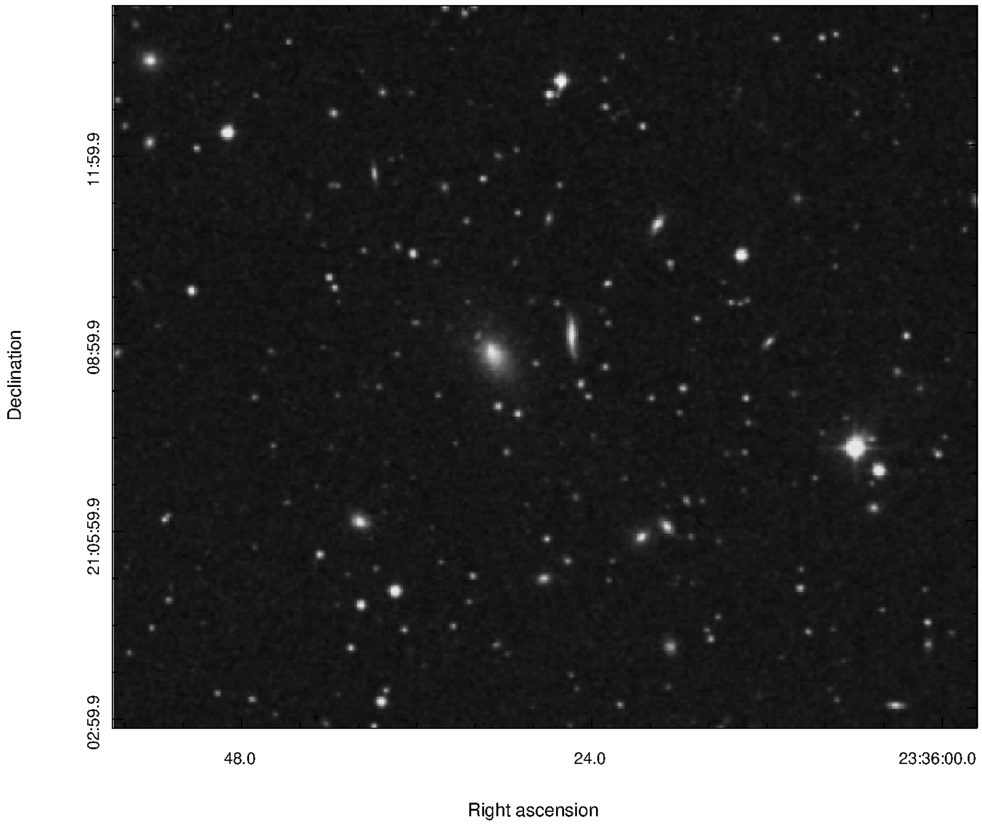

Figure 1.4: Archieve HST optical image of Abell 2626.

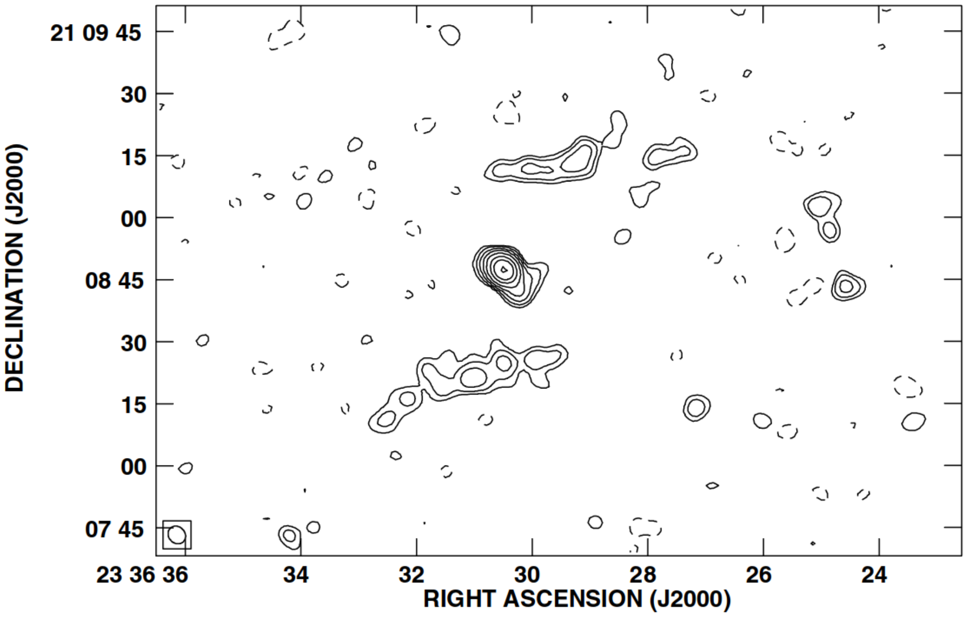

Figure 1.5: 1.5 GHz map of A2626 Gitti et al. (2004). The resolution is 4.5"x3.9". The rms level is 0.03 mJy/beam. The map shows the emission from the core and a couple of radio bars.

1.4.1 Previous studies of Abell 2626

The firsts studies of A2626 were focused on the dynamics of its components. By combining the first X observations obtained by $Einstein$ with optical spectroscopy, Mohr et al. (1996), and Cava et al. (2009) later, discovered that A2626 hots at least two sub-cluster, whose line-of-sight velocities differs by 2500 km/s. They identified a sub-cluster A centered at a velocity of <cz>=16533 ± 141 km/s and a sub-cluster B at <cz>=19164 ± 138 km/s. The sub-clusters differ also by virial mass and X-rays luminosity, so they classified A2626 as a pre-merging cluster.

The cluster radio emission has been the object of several studies. It was studied by Gitti et al. (2004) from VLA archival data at 1.5 GHz, who discovered that the cluster hosts an unusual, diamond-like, radio extended emission. The emission is associated to the inner region of the cluster, within 100 kpc. They argued that the diffuse emission may be a mini-halo, and they succeeded to reproduce its brightness with a theoretical model which accounts for the origin of radio mini–halos as related to electron re-acceleration by magneto-hydrodynamic (MHD) turbulence, which is amplified by compression in the cool cores (Gitti

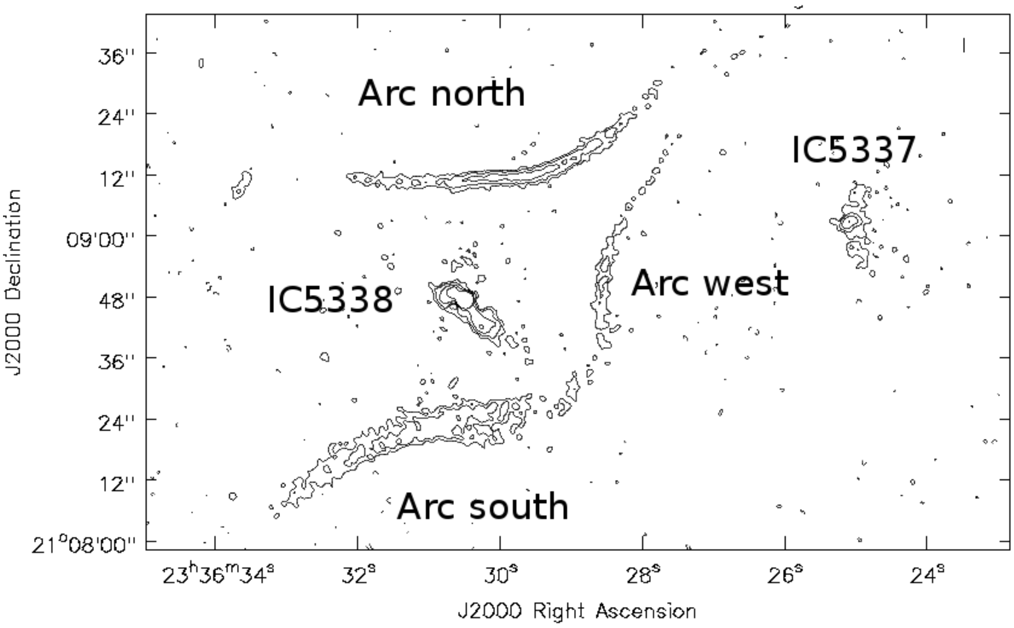

Figure 1.6: VLA 1.4 image of A2626. The RMS level is 0.01 mJy/beam and the resolution is 1.7"x1.6" (Gitti 2013)

et al. (2002), Gitti et al. (2004)). They noticed the presence of a couple of radio "bars" (e.g. Fig. 1.5) and they estimated a mean spectral index α ~-2.5 for the diffuse emission.

The radio sources in A2626 have been the subject of accurate studies.Gitti (2013) observed the cluster with the Very Large Array (VLA) at 1.4 and 4.8 GHz with unprecedented resolution and sensitivity. At 1.4 GHz the bars were fully resolved and appeared as radio sources detached from the core (Fig. 1.6), characterized by a peculiar morphology that resembles that of "arcs". They observed also a third arc, located at west between IC5338 and IC5337. Finally, Kale and Gitti (2017) analyzed an observation of the cluster performed with the Giant Metrewave Radio Telescope (GMRT) at 610 MHz of the cluster at 610 MHz, discovering a fourth arc located at east (Fig. 1.7). By combining their maps with the 1.4 GHz map of Gitti (2013) they obtained a spectral index map of the arcs. They discovered that the arcs have a steep spectral index α ~-3.
Rizza et al. (2000) carried out the first study of A2626 in the X-rays band focused on the interactions between the radio plasma and the hot ICM. They found evidences of enhanced X-ray emission spatially coincident with the radio source. Later, Wong et al. (2008) studied the thermal X-rays emission of the cluster by combining CHANDRA and XMM-Newton observations. In their meticulous

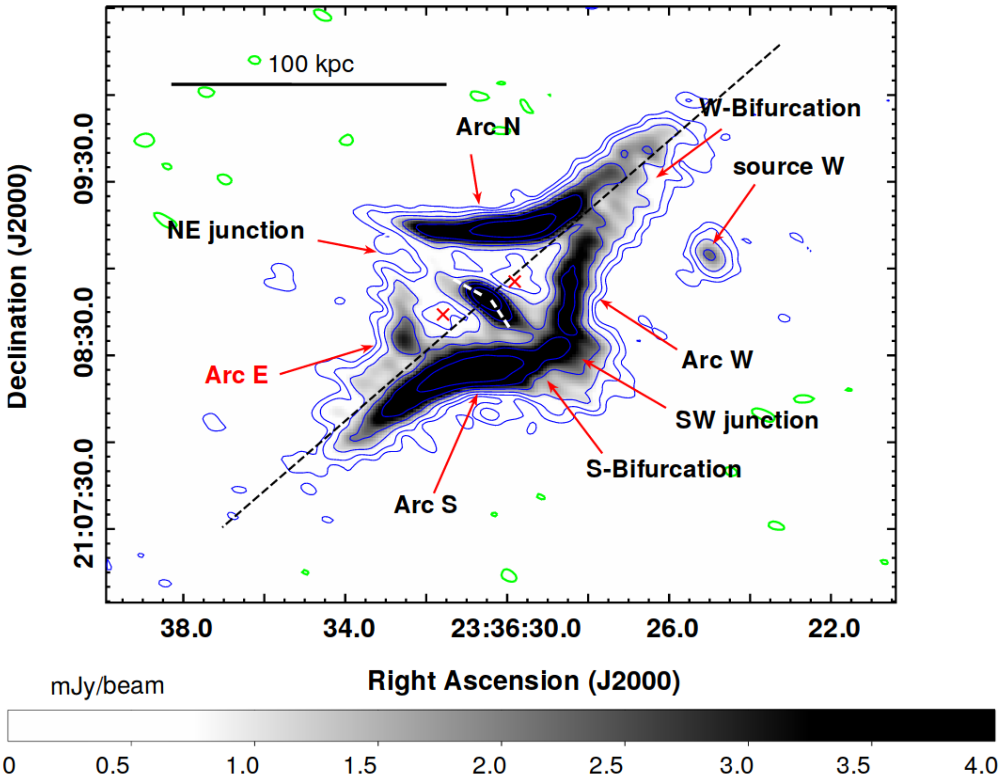

Figure 1.7: GMRT 610 MHz image of A2626. The RMS level is 0.08 mJy/beam and the resolution is 8.5"x4.4" (Kale and Gitti 2017)

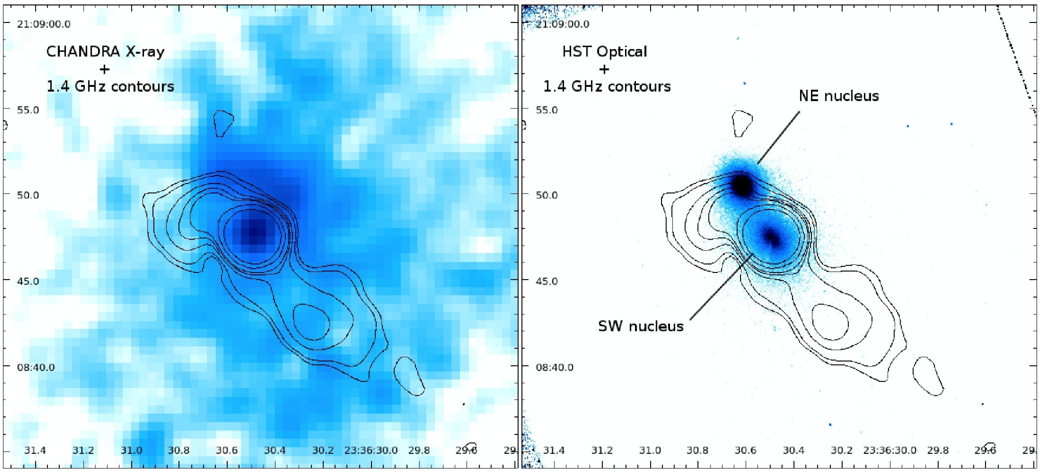

Figure 1.8: Overlay of *Left:* CHANDRA image of the core of IC5338 with the VLA 1.4 GHz contours (Gitti 2013); *Right:* HST image of the double core of IC5338 with the 1.4 GHz contours (Gitti 2013);

study they examined the properties of the sub-clusters and the inner emission. They discovered that the core of the cD galaxy produces both hard and soft X-rays emission, but they did not find clear evidence of an interaction between the radio arcs and the thermal plasma.

1.4.2 The cD galaxy IC5338

A double nuclei cD elliptical galaxy, IC5338, is sitting at the center of the cluster. From high-resolution VLA images Gitti (2013) recognized that there is an unresolved radio core coincident with the southern nucleus of the central cD galaxy. The radio source exhibits a small jet-like feature which extends south-west. The radio structure extends up to 5 kpc and its total flux density is 17.7 ± 0.5 mJy at 1.4 GHz and 9.6 ± 0.3 mJy at 5.5 GHz. The southern radio nucleus corresponds to a bright point source in X-rays emission in the 0.5-2 keV and in the 2-7 keV bands, while the northern nucleus shows no radio emission and fain X-rays emission in the soft band 0.5-2 keV (e.g. Fig. 1.8) (Wong et al. 2008).

1.4.3 The radio arcs system

The arcs are a system of elongated radio sources located around IC5338. In Tab. 1.2 we report a summary of the radio properties of the arcs. The arcs exhibit several features:

- they does not have the same flux density. In order of decreasing surface brightness there is the arc south, north, west and finally the east one (Kale and Gitti 2017);
- they do not exhibit polarized emission (Gitti 2013);

Source	Size [kpc^2]	$S_{0.6GHz}$ [mJy]	$S_{1.4GHz}$ [mJy]	$\alpha_{0.6}^{1.4}$
Arc north	152	101±10	7.0±0.4	-3.2±0.1
Arc south	120	154±15	9.9±0.5	-3.3±0.1
Arc west	152	49.6±5	3.4±0.2	-3.2±0.1
Arc east	79	14.4±1.5	0.7±0.1	-3.6±0.2

Table 1.2: Summary of the radio properties of the arcs (Kale and Gitti 2017).

- the arcs north and south are surprisingly symmetric. This symmetry is not observed between the arc east and west;
- arcs south and west are connected by a junction (e.g. Fig. 1.7), whereas arcs north ans east are detached;
- they all have extremely steep spectrum (Kale and Gitti 2017);

Since their discovery (Gitti et al. 2004), the nature of the bars/arcs has been a puzzle. Their symmetrical positions on each side of the core suggest that they are radio bubbles, but their thin, elongated shapes are unlike those typically observed in cool core clusters. They may represent radio emitting plasma injected by the central source during an earlier active phase, which has then propagated through the cool core region in the form of buoyant sub- sonic plumes (e.g. Churazov et al. (2000)). However, such plumes are expected to have a torus-like concavity, contrarily to the observed shape in A2626. Furthermore, by comparison to radio lobes and bubbles associated with other cool core dominant radio galaxies, one might expect these to be regions of reduced X-ray emission surrounded by bright rims. In fact, previous ROSAT observations failed to find strong X-ray deficit in the cool core of A2626 (Rizza et al. 2000).
Wong et al. (2008) argues that the lack of clear correlation between the radio arcs and any structures in the X-ray images may indicate that they are thin tubes parallel to the plane of the sky, or that the radio plasma is mixed with the X-ray gas, rather than displacing it.

They suggest that jet precession might also provide an alternative explanation of origin of the north and south arcs. A pair of precessing jets, originated inside the core of IC5338, may be able to leave a couple of collimated trails of re-accelerated relativistic plasma when stopped at a *working surface* in the ICM.

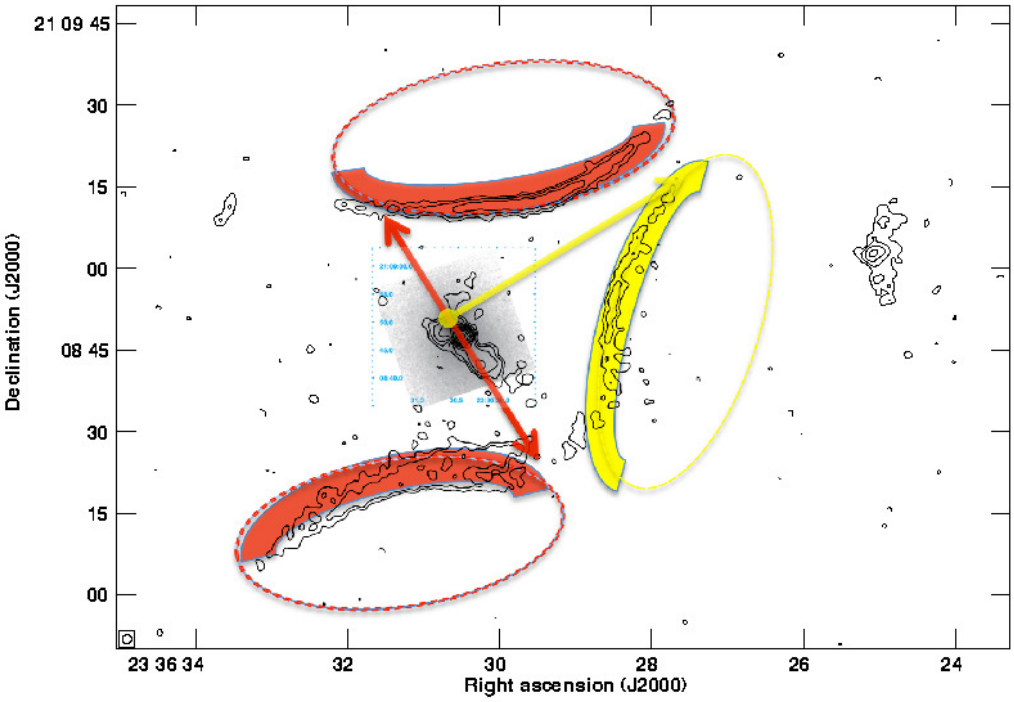

Figure 1.9: Sketch of the jet-precession model. In this picture, that preceded the discovery of the fourth arc (2017), the north-south arcs and the western arc are thought to be originated by two different couple of jets.

The impressive arc-like, symmetric morphology of these features, highlighted by the high-resolution radio images reported in Gitti (2013) and Kale and Gitti (2017), may support this interpretation, but the presence of four arcs makes the interpretation even more puzzling, because another pair of jets would be necessary to originate the arcs east and west (e.g. Fig. 1.9).

The radio arcs have an elongated morphology and steep spectral index. These characteristics are similar to those of cluster radio relics associated with particle re-acceleration due to shocks (Feretti et al. 2012). The combined shape of the arcs suggests that they could trace the symmetric fronts of a single elliptical shock originating inside the core. However, their concavity is not what one would expect from a shock propagating from the center. If they are cluster radio relic-like sources, the observed concavity suggests that four distinct shocks are propagating towards the center from different directions. However,CHANDRA observations failed to detect any obvious X-ray edge ascribable to shock fronts. Furthermore, relic sources are typically strongly polarized (Feretti et al. 2012), whereas no significant polarized flux is detected Gitti (2013). The relativistic electrons responsible for the diffuse emission may also have been re-accelerated by turbulence generated by the sloshing of the cool core gas (e.g. Mazzotta and Giacintucci (2008), ZuHone et al. (2013)).

However, it is possible that the complex morphology of the A2626 radio source may result from a combination of the scenarios presented above.

1.4.4 The head-tail galaxy IC5337

This is the second luminous galaxy of the cluster after IC5338 and it exhibits evidence of interactions with the ICM. It is classified as S0 galaxy in optical band and as Head-tail radio galaxy because of the shape of its radio emission, which clearly shows a bright central nucleus and a pair of diffuse radio tails. Due to its disrupted morphology it was classified as a *Jellyfish galaxy* by Poggianti et al. (2016)

Wong et al. (2008) discovered that it hosts a X-ray point source located on the galaxy center, and diffuse soft-X emission, which correlates with the radio emission. They observed also another point source located in the southern tail, which is not associated with any known galaxy.

They finally note that the shape of IC5337 resembles a bow shock, which means that the galaxy is moving through the ICM toward the center of the cluster.

The interpretation of the kinematics of IC5337 is complicated by an ambiguity in the literature concerning its radial velocity. There are two optical determinations of the radial velocity that give values that are consistent with the velocity of other galaxies in the center of Abell 2626, including the cD galaxy IC 5338. Huchra et al. (1999) give a velocity of 16485 ± 37 km/s, which is consistent with the velocity of IC5338. On the other hand, Mohr et al. (1996) measured an optical velocity of 18903 ± 39 km/s, assigning the galaxy to the southern sub-cluster. If this is correct, then IC5337 may follow the dynamics of the sub-cluster, thus moving from southwest to northeast. However this would be inconsistent with the X-ray morphology, which suggest that the galaxy is moving from east to west.

Chapter 2

Data reduction of the JVLA dataset

In this chapter we report the accurate processes that we performed to calibrate the new JVLA observations at 3.0 and 5.5 GHz before proceeding with the scientific analysis, and a brief explanation of the basis of radio interferometric data reduction.

2.1 Radio astronomy and Interferometry

Radio astronomy is a branch of astronomy that studies celestial objects at radio frequencies. The initial detection of radio waves from an astronomical object was made in the 1930s, when Karl Jansky observed radio emission at 1.4 GHz coming from the Milky Way. The radio window extends from about 10 MHz to 100 GHz (from 0.02 mm to 30 m). These limits are dictated by the composition of the atmosphere (CO_2 , O_2, H_2O molecules) which absorbs photons with wavelengths lower than 0.02 mm and by the ionosphere, which reflects back into space photons with wavelengths longer than 30 m (e.g. Fig. 2.1). Moreover, the atmosphere ,especially the ionosphere, emits radio noise that can seriously degrade the sensitivity of ground-based radio observations. As the frequency increases, opacity gets higher, causing bigger distortions to observations. For these reasons the best sites for observing, especially at higher frequencies, are exceptionally high and dry locations.

Unlike other branches of astronomy in which photons are so energetic to produce the photoelectric-effect, radio astronomy makes use of the Fraunhofer diffraction to detect radiation: the radio emission of source, that is located at infinite distance from the observer, is collected as a signal $g(x)$, called *grading*:

$$g(x) = F(x)e^{-i\phi(x)}e^{-i\omega t} \tag{2.1}$$

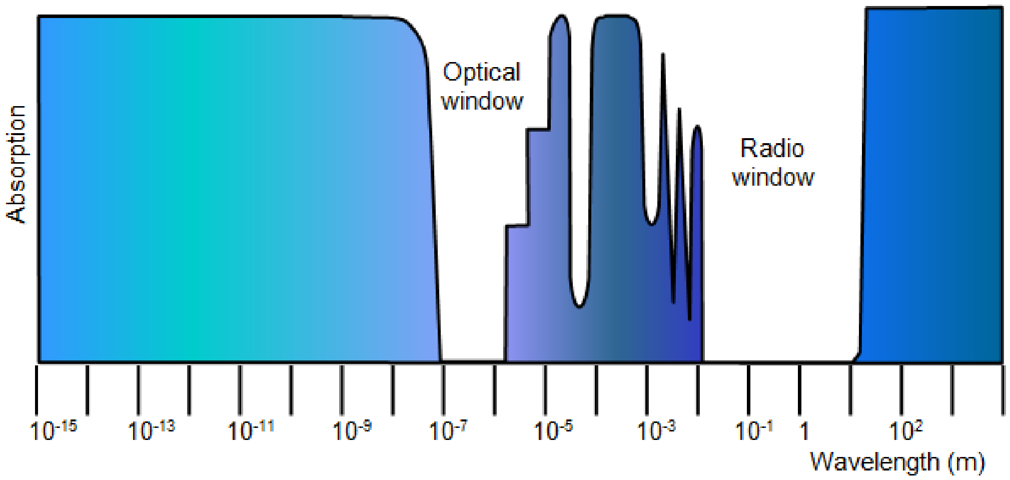

Figure 2.1: Atmospheric windows of the astrophysical observations.

where $F(x)$ and $\phi(x)$ are the amplitude and the phase of the signal. The Fraunhofer diffraction tells us that real electric field $E(\psi)$ of the source is the Fourier transformation (FT) of the observed grading $g(x)$:

$$E(\psi) \sim \int_{-\infty}^{+\infty} g(u) e^{-2\pi i u \psi} du \tag{2.2}$$

The passage through the FT entails that the real shape of the brightness distribution on the sky plane $E(\theta, \psi)$ is radically different on the grading plane $g(u, v)$: a delta distribution on the sky plane, as a point-like source, becomes a planar distribution on $g(u, v)$, whereas a Gaussian-like distribution, like a diffuse radio source, changes its width according to the *similarity property* of the FT.
The radio telescope is basically a radio antenna, where the radio waves are collected by a metallic dish and are focused on the receiver, called feed. To maximize his sensitivity the feed is usually kept at low temperatures by a cryostat. Due to the centimeter-scale of the radio wavelengths it is possible to substitute the full mirror of a classic filled parabolic antenna with a metallic net-like surface with a "gap" between the mash that must be smaller than 1/20 of the observed wavelength. This technical expedient reduces the weight of the dishes, and their economic cost, making possible to build larger radio telescope.
Each radio telescope is characterized by a diffraction figure called power pattern or beam which is usually expressed in polar coordinates P(θ, ϕ). This represents the measure of the instrumental response to the observation of a point-like source. The beam maxima are known as lobes; a distinction is usually made between the main lobe, where the antenna is most sensitive, and the minor lobes

or sidelobes. The angle subtended by the half power level of the main lobe is called *Half-Power Beam Width* (HPBW) and it is a measure of the instrument resolving power θ:

$$\theta = 1.22\frac{\lambda}{D} \tag{2.3}$$

where λ is the observed wavelength and D is the diameter of the mirror. To improve the resolution at fixed λ one should increase D. Unfortunately the size of the dish cannot exceed a maximum value for structural and economic reasons, so the resolution of the single-dish radio telescopes is limited. This problem was resolved by the introduction of the interferometric technique.
Interferometers are arrays of several antennae working together exploiting the interference principle between coherent waves, thus realizing an "unfilled aperture telescope". The basic component of the interferometer is the *baseline*, a couple of antennae at distance b, which signal is composed to create a *visibility* $V_{ij}(u, v)$ (e.g. Fig. 2.2). The fringe visibility $V(u, v)$ is defined as a function where u and v represents the coordinates of a baseline projected on a plane perpendicular to the line of sight called (u,v) plane (Fourier plane, or UVplane). The visibility function can be written as the Fourier transform of the sky brightness B(x,y):

$$V = V_0 e^{I\phi} \propto \int\int_{-\infty}^{\infty} B(x,y)\mathrm{e}^{-2\pi i(ux+vy)}\,\mathrm{d}x dy \tag{2.4}$$

where V_0 is defined as the amplitude,in other words the intensity of the signal, and ϕ is the phase, which indicates the position in the sky of the source. This relationship connects the Fourier plane with the space of real brightness.

The signals collected by every antenna are processed by a mainframe, the *correlator*, which combine every possible combination of baseline of the interferometer. In order to reconstruct a coherent wavefront from the signals of several antennae the correlator has to know exactly the *geometric delay* τ, that is the time elapsed between the reception of the same coherent wave front from each antenna.
In a single observation the total number of collected visibilities is:

$$N_{tot} = [\frac{N_A(N_A-1)}{2}] \times [\frac{T_{tot}}{t_i}] \times [n_{ch} \cdot n_{spw}] \times 4 \tag{2.5}$$

where N_A is the number of antennae in the interferometer, T_{tot} is the duration of the observation, t_i is the *integration time*, which is the time necessary for the correlator to process a single coherent wavefront, thus representing the resolution in time of the observation, and $[n_{ch} \cdot n_{spw}] \times 4$ is the extent of the receiver band. Every radio telescope has several receiver bands and each of them is divided in n_{spw} *spectral windows*, which are divided in n_{ch} channels. Moreover, each receiver can measure both the *total intensity*, through the *parallel hands* signal

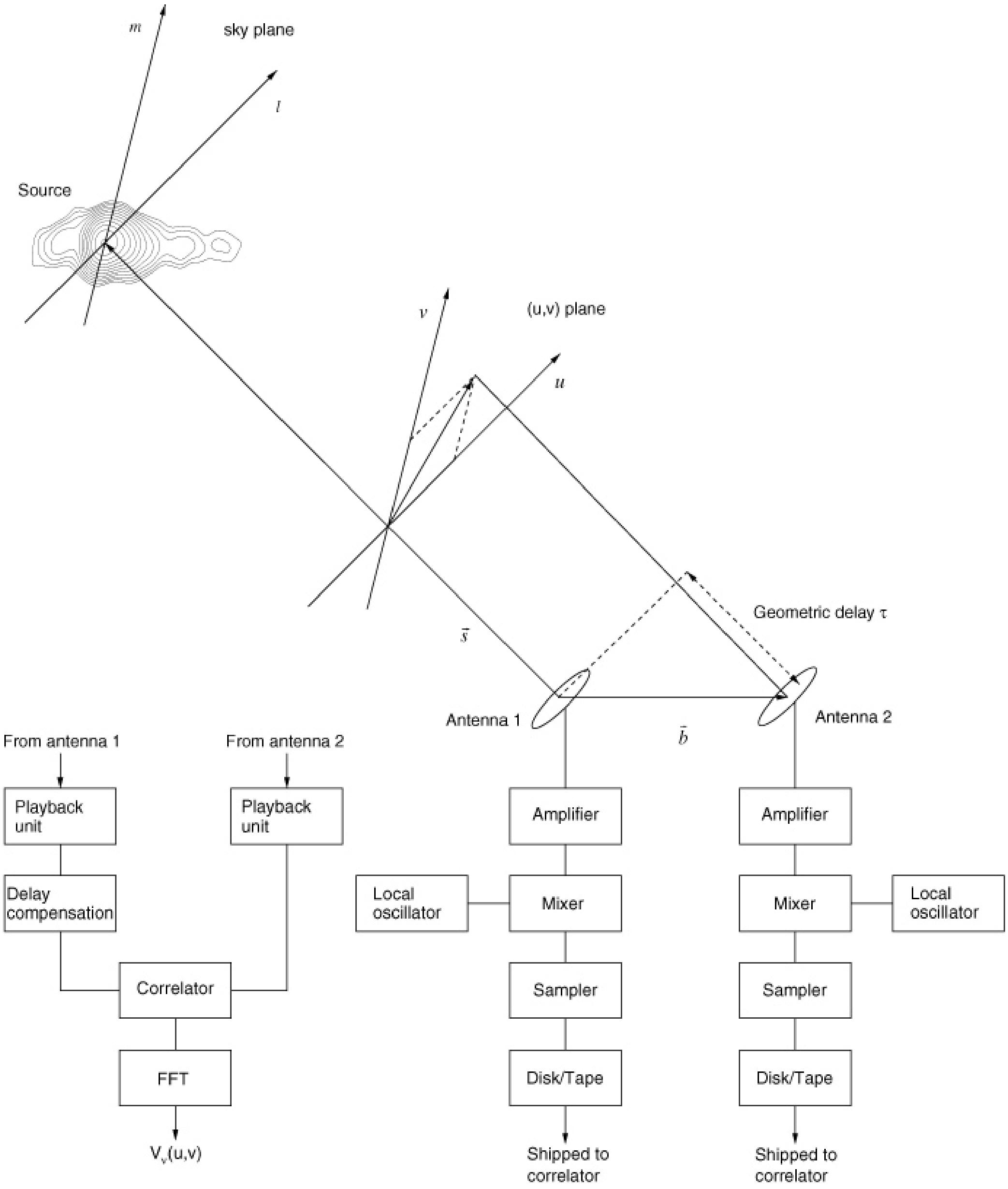

Figure 2.2: How a typical baseline works: the signal of the wavefront is collected by the antennae and the signal of each antenna is elaborated to reduce the noise, then it is composed in a single visibility $V_{ij}(u,v)$ by the Correlator (Middelberg and Bach 2008).

RR and LL, and the *polarized emission* as *cross-hands* signal RL and LR.
The real advantage of the Interferometer respect the single Dish comes from the different gradind $g(x)$ of the emitting field $E(\phi)$:

$$g_{int}(x) = \varPi(D) * [\delta(x - b/2) + \delta(x + b/2)] \tag{2.6}$$

where $\varPi(D)$ is the grading of the single antenna with aperture D and b is the distance between each antenna. This different grading entails a beam $P(\phi)$:

$$P(\phi) = sinc^2\left(2\pi\frac{b}{\lambda}\psi\right) cos^2\left(2\pi\frac{D}{\lambda}\psi\right) \tag{2.7}$$

That means that the width of the beam, and therefore the resolution power of the interferometer, is driven by the baseline length b, rather than by the dish radius D as in Eq. 2.3. Therefore, there are three scales which are important in interferometric observations:

- the smallest observable spatial scale, or resolution: $\theta_{min} = 1.22\lambda/b_{MAX}$ where b_{MAX} is the longest baseline of the interferometer;
- the largest observable spatial scale: $\theta_{MAX} = 1.22\lambda/b_{min}$ where b_{min} is the shortest baseline of the interferometer. This scale contributes to determine the sensitivity to the diffuse emission of the interferometer;
- the field of view, or FOV: $\theta_{FOV} = 1.22\lambda/D$;

With single-dish observations it is possible to sample the emission coming from all the spatial scale ranging from zero to $\lambda\ /D$. On the other hand, with interferometric ones it is possible to sample only the emission coming from the spatial scales between $\lambda\ /\ b_{min}$ and $\lambda\ /b_{max}$. To reconstruct the zero spacing information, that would collect the whole flux of a radio source, it is possible to combine single dish and interferometric observations of the same source.

2.2 Karl G. Jansky Very Large Array

The Karl G. Jansky Very Large Array (VLA) (Fig. 2.3) is a radio astronomy observatory located on the Plains of San Agustin, New Mexico, at more than 2000 meters above the sea level and it is a component of the National Radio Astronomy Observatory (NRAO). The radio telescope comprises 27 independent antennae, each of which has a dish diameter of 25 meters and weighs 209 metric tons.

Figure 2.3: the Karl G. Jansky Very Large Array

The antennae are distributed along the three arms of a track, shaped in a Y configuration, (each of which measures 21 km long). Using the rail tracks that follow each of these arms the antennae can be physically relocated to a number of prepared positions, allowing aperture synthesis interferometry with up to 351 independent baselines. So, the array acts as a single antenna with a variable diameter. The angular resolution that can be reached is between 0.2 and 0.004 arcseconds. There are four commonly used configurations, designated A (the most extended) through D (the most compact, when all the dishes are within 600 m of the center point) (e.g. Fig. 2.4). The observatory normally cycles through all the various possible configurations (including several hybrids) every 16 months; the antennae are moved every three to four months. Moves to smaller configurations are done in two stages, first shortening the east and west arms and later shortening the north arm. This allows for a short period of improved imaging of extremely northerly or southerly sources. The frequency coverage is 74 MHz to 50 GHz (400 to 0.7 cm). The Array Operations Center (AOC) for the VLA is located on the campus of the New Mexico Institute of Mining and Technology in Socorro, New Mexico. The AOC also currently serves as the control center for the Very Long Baseline Array (VLBA), a Very Long Baseline Interferometr (VLBI) array of ten 25-meter dishes located from Hawaii in the west to the U.S. Virgin Islands in the east that constitutes the world's largest dedicated, full-time astronomical instrument. In 2011, a decade long upgrade project had resulted in the VLA expanding its technical capacities by factors of as much as 8,000.

The 1970s era electronics were replaced with state-of-the-art equipment. To reflect this increased capacity, VLA officials asked for input from both the scientific community and the public in coming up with a new name for the array, and in January 2012 it was announced that the array would be renamed the "Karl G. Jansky Very Large Array".On March 31, 2012 the VLA was officially renamed in

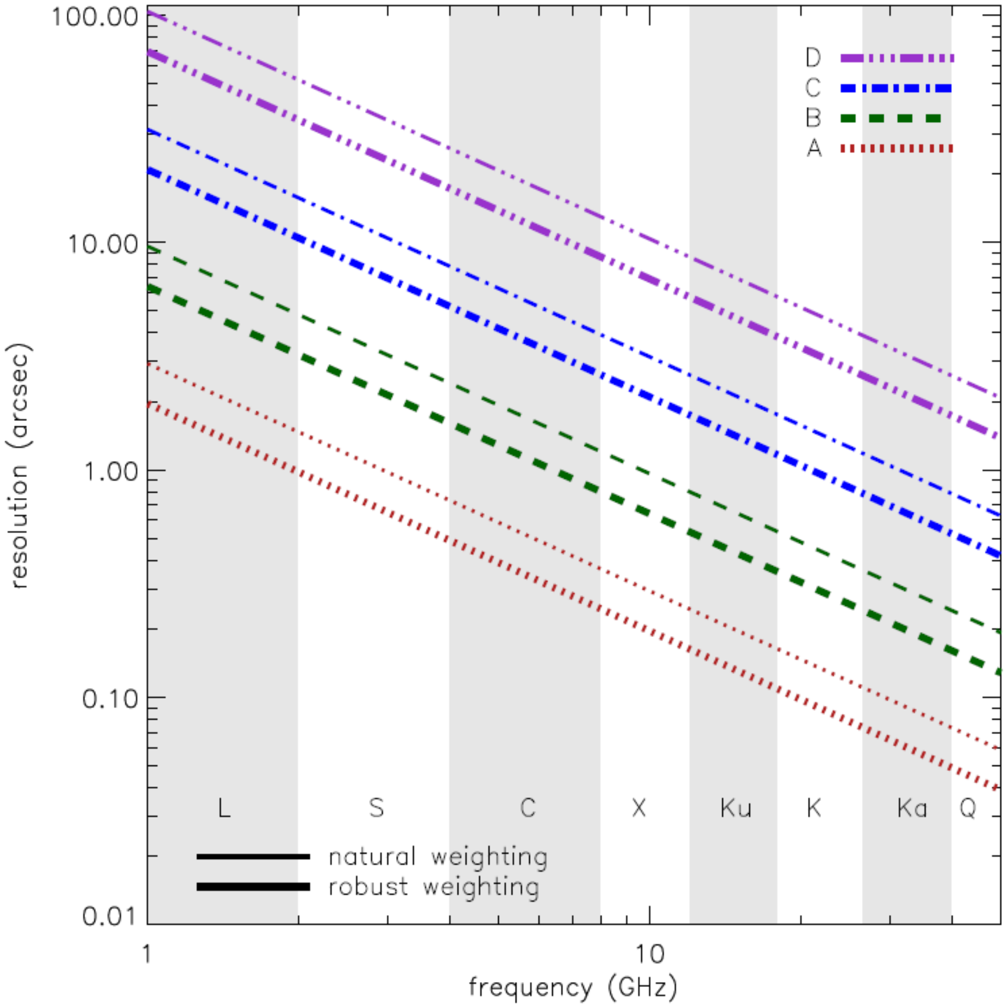

Figure 2.4: Resolution power of each receiver band of the JVLA in the four configurations.

a ceremony inside the Antenna Assembly Building. Astronomers using the VLA have made key observations of black holes and protoplanetary disks around young stars, discovered magnetic filaments and traced complex gas motions at the Milky Way's center, probed the Universe's cosmological parameters, and provided new knowledge about the physical mechanisms that produce radio emission. These are some of the most important scientific discovery made by this instrument:

- Ice on Mercury;
- Radio atmospheres around stars;
- A New Type of Astronomical Object: "Microquasars" in Our Own Galaxy;
- studies of Shrouded Center of the Milky Way;
- Channels, changes, and inner parts of Superfast Cosmic Jets;
- the First "Einstein Ring" Gravitational Lens;
- Radio waves from Gamma Ray Bursts that helps locate them;
- Carbon Monoxide disk in galaxy in early universe;
- Black holes apparently form before galaxy bulges;
- Pebble-sized chunks show first stages of planet formation;
- Billion-light-year-diameter "Hole in the Universe";

2.3 A-priori calibration

2.3.1 Basic steps of radio data reduction

The calibration is a necessary step of every scientific analysis. A dataset is composed by a huge number of visibilities (as explained by Eq. 2.5), but each of them is corrupted by errors that may come from the hardware of the receivers or external interferences. Also the ionosphere, which interacts with the radio waves, may produce alterations on the phase of the visibilities. The aim of the calibration is to correct these errors, that may jeopardize the scientific studies. The whole calibration was made with the software CASA 4.6, a package of tasks and subprograms which allows the reduction from an initial raw dataset to the final image of the radio source.

The difference between the visibility observed by a baseline i-j at time t, $V_{ij}^{Obs}(u, v, \nu)$ and the true visibility $V_{ij}^{True}(u, v, \nu)$ may be written as:

$$V_{ij}^{True}(u, v, \nu) = G_i G_j V_{ij}^{Obs}(u, v, \nu) e^{i[\theta_i(t) - \theta_j(t)]} \tag{2.8}$$

where

$$G_i G_j = b_{ij}(t)[B_i(\nu, t) B_j^*(\nu, t)] g_i(t) g_j(t) \tag{2.9}$$

The visibility is expressed as a function of frequency ν and spatial wave numbers u e v. The others terms are the *complex gains* $G_i G_j$, the corrections which are necessary to correct the visibilities. They include the amplitude gains g_i, the phase gains θ_i, the complex bandpass B_i and the baseline therm b_{ij}. Except for the last one, the others gains are evaluated separately for each antenna, because the calibration is based on the hypothesis that corrections may be factorized on each antenna of the baseline. The aim of the calibration is to estimate each gain for each visibility of the dataset.

The calibration process requires the use of the *calibrators*, radio source whose radio properties are known *a-priori*, that the observer has to include in every observation. CASA includes a library of model visibilities for the principal calibrators in several radio bands.

Therefore, a standard radio observation must include:

- **Target:** the subject of the scientific study. The calibration aims to remove every phase or amplitude errors that may compromise the scientific analysis. If the target angular dimension exceeds the field of view of the radio telescope is possible to combine several observations in a mosaic to cover the whole structure.

- **Amplitude Calibrator:** its purpose is to calibrate the flux. It is the first calibrator used in the calibration to calculate the first corrections on phase and amplitude. It is also known as Flux Density calibrator or primary calibrator. The Amplitude calibrator must be a strong, point-like source with a constant flux in time. If those conditions are satisfied, so the chosen calibrator is a point-like source with a delta-like surface brightness distribution on the sky-plane, then its visibilities will have a planar distribution on the UVplane, thus resulting in constant phase and amplitude;

- **Phase Calibrator:** its purpose is to compute the phase gains for the target. It is also called secondary calibrator. Like the amplitude calibrator, it should be a strong point-like source, in order to have visibilities with constant phase. However, it can be a variable source, on condition that the variability time-scale is longer than the observation time;

- **Polarization Calibrator:** its purpose is to calibrate the response of the receivers to the polarized emission. An ideal receiver divides perfectly the incoming radiation in two components, the Left , L, and the Right, R, orientation, that are used to reconstruct components of the total intensity emission RR and LL and the polarized emission RL and LR. Unfortunately, an interferometer is made of real receivers that have a defective response. The polarization calibrator should be a radio source of well-known polarized flux density, that allows to correct the response of the receivers by comparing the predicted flux with the observed one;

- **Bandpass Calibrator:** usually the Amplitude calibrator is used also as Bandpass calibrator. Every receiver suffer from a systematic loss in signal amplitude in the channels located at the edges of every spectral windows. This effect can be corrected by comparing the amplitude measured in these channels with the model amplitude at the related frequencies;

An observation is divided in *scans*, i.e. chunks of the total observation time that are used to observe a single source. The target and the phase calibrator must be observed alternately in several scans to ensure that the phase gains of the target can be time-extrapolated from the phase gains of the calibrator. The other calibrators do not have restrictions on the observation order.

The radio data reduction is an iterative operation. It starts with the *editing* of the visibilities of the calibrators, then the amplitude calibrator is calibrated by comparing its visibilities with the model. If the calibration is corrected, thus its corrected visibilities resemble as much as possible the model ones, then the gains for the others calibrators are computed from the gains of the amplitude calibrator. If even the corrected visibilities of the phase calibrator are acceptable, then the corrections for the target visibilities are estimated by time-interpolating the gains solutions of the calibrator. After the first calibration the target may require an additional step of editing, followed by a second application of the corrections. Finally the target is *self-calibrated* in order to obtain phase and amplitude corrections on time intervals that are shorter than the intervals of the time-interpolation which produced the first gains, thus further improving the calibrations.
Therefore, the basic steps of the calibration of a JVLA dataset are:

- **Editing:** raw datasets are usually contaminated by anomalies, that may come from technical problems of the receivers or external radio frequency interferences (RFIs). The purpose if the data editing is to remove them, by flagging the bad visibilities from the dataset. The data flagging is a delicate operation. On the one hand, removing too many visibilities lead to losses of sensitivity, on the other hand, a conservative editing may not remove all

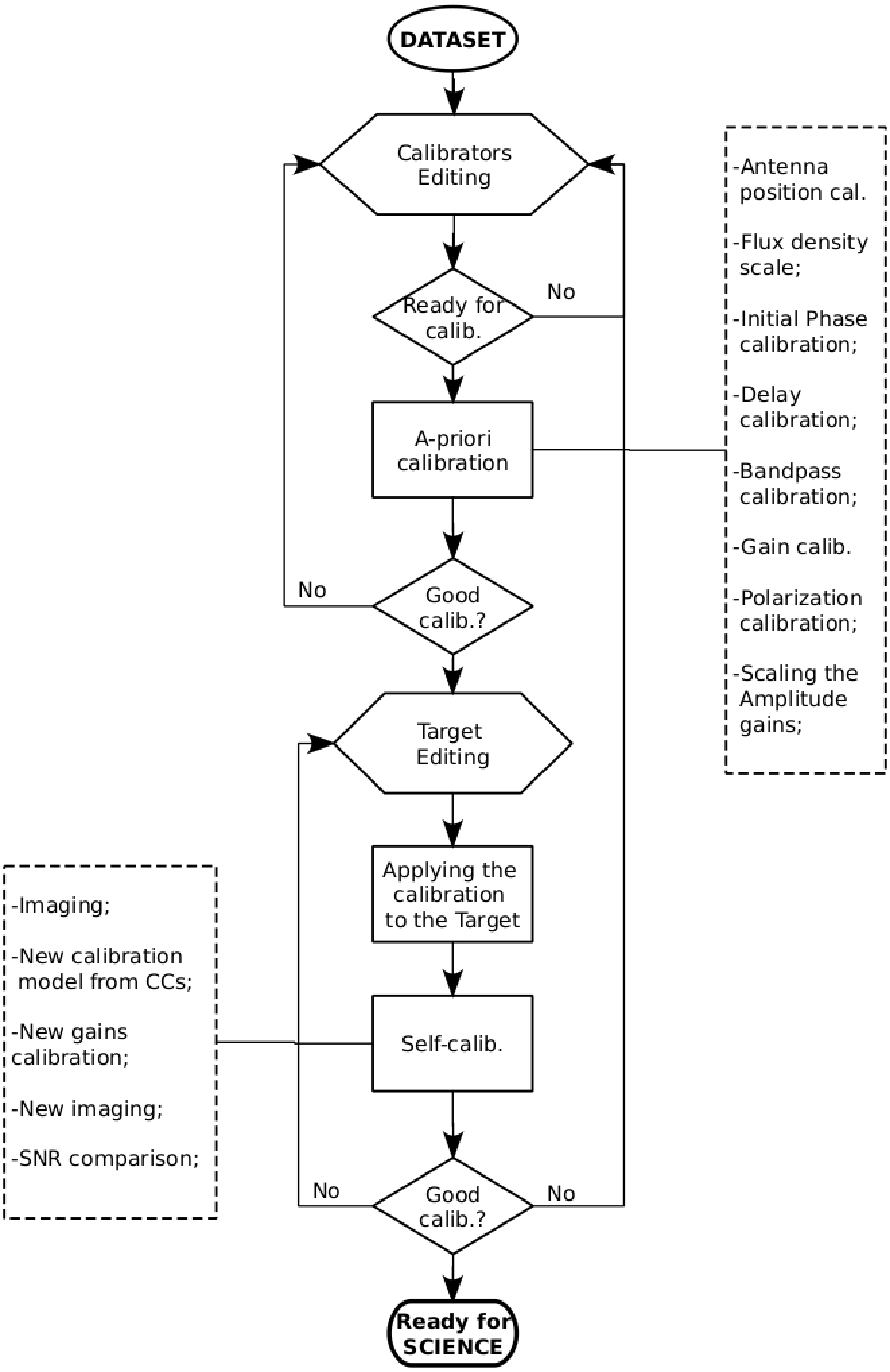

Figure 2.5: Flow diagram of a Radio dataset calibration

the problems and consequently jeopardize the calibration. Moreover recognizing the bad visibilities from the good ones may be difficult, especially for diffuse sources on a large field, because it is not possible to recognize *a-priori* the visibilities of the target from the ones of a bright background source. Because of all these reasons, the editing is usually repeated many times, in order to improve the calibration at any iterations.
CASA provides many algorithms that remove automatically the worst visibilities of the dataset, but it is always recommended to carry out the flagging manually. A solid strategy to remove every anomaly is comparing multiple plots of the same dataset in any possible combination of parameters which characterize a visibility, that are amplitude, phase, time , position in UVplane (UVwave) and frequency. Often there are discrepancies which are crystal clear in a certain plot, but otherwise they are not visible in others. Due to the complexity of a JVLA dataset, the editing requires lot of patience and time to be completed properly;

- **A-priori Calibration:** the part of the calibration which is carried out using only the calibrators. It is composed of:
    - **Antenna position correction:** correction on the exact distance between the antennae, which is fundamental to compute the geometric delay for every coherent wavefront. It can be obtained directly from the NRAO server or manually through the $baseline - based$ calibration. It provides the b_{ij} therm of the final corrections.
    - **Flux Density scale:** it is necessary to provide a flux density value for the amplitude calibrator. For the JVLA the flux density scale at most frequencies was determined from WMAP observations of planet Mars, which was transferred to a small number of amplitude calibrators. For this reason, flux density and the visibility distribution on the UVplane of these sources are well-known (e.g. the model for the emission of 3C48 at 5.5 GHz in Fig. 2.6). The initial amplitude of the sources is expressed in non-physical units, but it is possible to evaluate the conversion factor to the physical ones by comparing the predicted amplitude of the flux calibrator with its observed value.
    - **Initial Phase Calibration:** the reason for this step is to average over the (typically small) variations of phase with time of the flux/bandpass calibrator, before solving for the bandpass solution itself. Depending upon frequency and configuration, there may be significant gain variations between different scans of the calibrator, particularly if the scans are executed at different elevations. One can solve for an initial set of antenna-based gains, which will later be discarded, in order

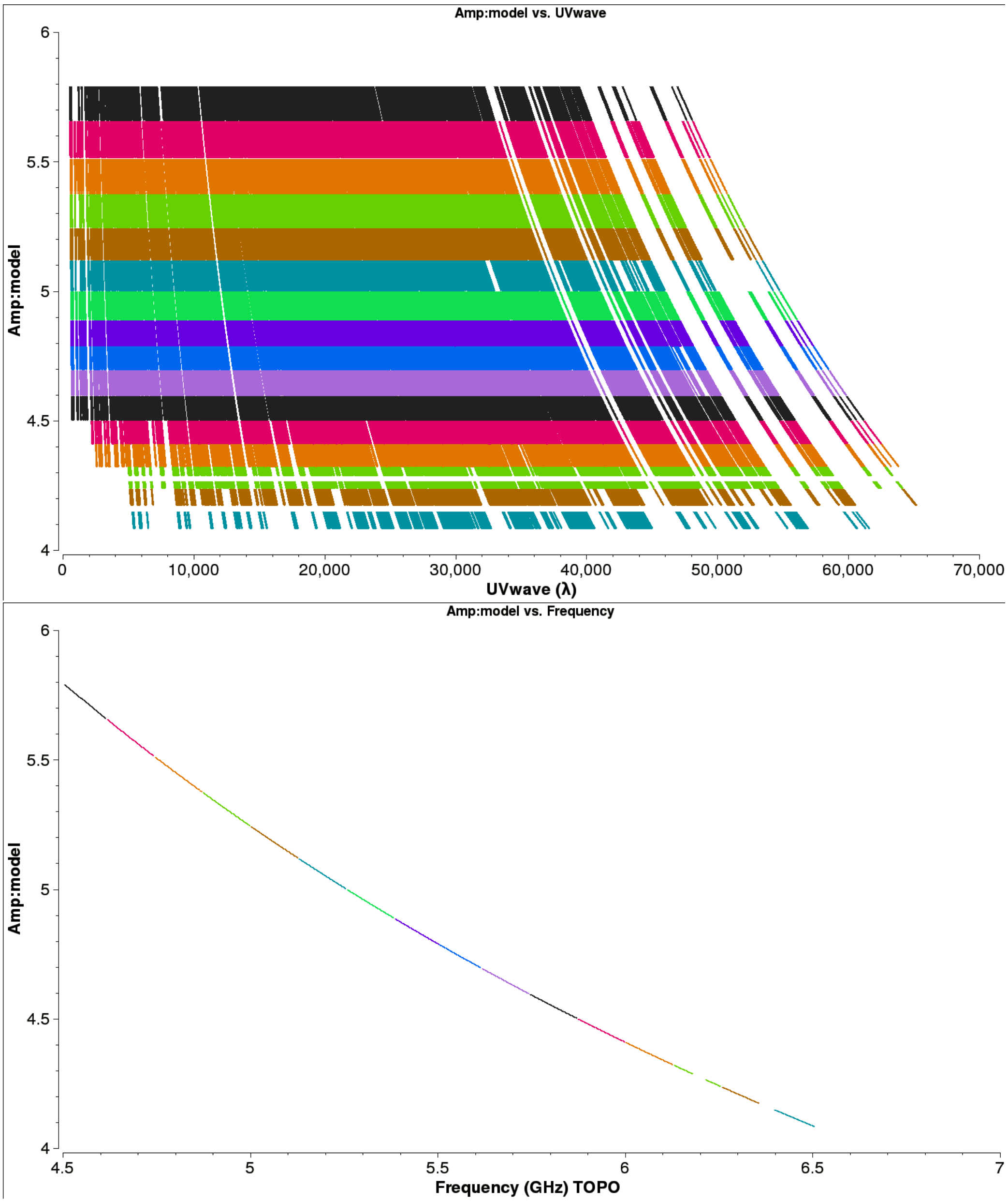

Figure 2.6: Amplitude vs UVwave (Top) and Amplitude vs Frequency (Bottom) plot of the model of 3C48. the flux density calibrator, that we used for the calibration of the C-band dataset.

to moderate the effects of variations from integration to integration and from scan to scan on the bandpass calibrator. While amplitude variations with time will have little effect on the bandpass solutions, it is important to solve for phase variations with time to prevent decorrelation when vector averaging the data for computing the final bandpass solution;

- **Delay Calibration:** the first stage of bandpass calibration involves solving for the antenna-based delays which put a phase ramp versus frequency channel in each spectral window. Each delay is solved for each antenna relative to a reference antenna, which should be selected carefully. The reference antenna would be in the center of the array and it would have a good response all over the observation. This is not a full global delay, but gives one value per spectral window per polarization.

- **Bandpass Calibration:** this step solves for the the complex bandpass B_i and it is needed to reconstruct the amplitude of the signal in certain frequencies, after it was filtered by the spectral response of the radio telescope. The edge channels of every spectral windows has a systematic weaker response than the other channels, so the observed visibilities with the respective frequencies will exhibit a lower amplitude than expected.

- **Gain Calibration:** finally the amplitude and phase gains g_i and θ_i are derived for the phase and polarization calibrators. The flux density gains are determined from the amplitude gains of the flux calibrator, whereas the absolute phase is determined from the phase gains of the reference antenna, which are defined as zero, on the assumptions that the calibrators are point-like source.

- **Polarization Calibration:** the flux collected by a baseline ij is composed by four components, the parallel-hand correlations for the total flux intensity R^iR^j and L^iL^j, and the cross-hand correlations for the polarized flux R^iL^j and L^iR^j, where R and L are the *Right-hand* and *Left-hand* component of the emission, that are measured by the two orientation of the circular feed. Even the most technical perfect feed corrupts each component with a small fraction of the flux of the other, because its mechanical width makes it able to receive both component even it was designed to receive only one of them. This is the *Instrumental Polarization* and these errors are known as *leakage* (D-terms). They influence the observed flux as:

$$R^i_{obs} = R^i_{True} + D_L L^i_{True} \tag{2.10}$$

$$L^i_{obs} = L^i_{True} + D_R R^i_{True} \tag{2.11}$$

In other words the measured R-flux is equal at the real one plus a little percentage of the L-flux, and vice versa. Unfortunately the D-terms propagate in the correlations as:

Parallel-Hands:

$$\begin{aligned}(R^iR^j)_{obs} &= (R^iR^j)_{True} + (R^iL^j)_{True}D^i_L + (L^iR^j)_{True}D^j_L + \\ &+ (L^iL^j)_{True}D^i_LD^j_L \\ (L^iL^j)_{obs} &= (L^iL^j)_{True} + (L^iR^j)_{True}D^j_R + (R^iL^j)_{True}D^i_R + \\ &+ (R^jR^i)_{True}D^i_RD^j_R\end{aligned}$$

Cross-Hands:

$$\begin{aligned}(R^iL^j)_{obs} &= (R^iL^j)_{True} + (R^iR^j)_{True}D^j_R + (L^iL^j)_{True}D^i_L + \\ &+ (R^jL^i)_{True}D^i_LD^j_R \\ (L^iR^j)_{obs} &= (L^iR^j)_{True} + (L^iL^j)_{True}D^j_L + (R^iR^j)_{True}D^i_R + \\ &+ (R^iL^j)_{True}D^i_RD^j_L\end{aligned} \tag{2.12}$$

For RR and LL the first terms, that are the true amplitude of the signal, are greater than the others the D-terms are negligible. On the other hand, the leacked parallel-hands terms in RL and LR are comparable with the true amplitude because they both represent a few percentage of the total flux. So, in order to measure the true polarization flux, they have to be removed. The Polarization calibration is developed in two steps: first the D-terms are solved by comparing the measured polarized flux with the polarized flux of a unpolarized source (as the phase calibrator), then the corrections on the position angle are computed from the polarization calibrator.

- **Scaling the Amplitude gains:** the flux densities of the phase and polarization calibrators are estimated from the flux density of the amplitude calibrator, assuming that the ratio between the flux densities is equal to the ratio between the amplitude gains of each source.

Table 2.1: New JVLA data analysed in this work (project code:14B-022 PI M.Gitti)

Central frequency [GHz] Band name	5.5 C	3.0 S
Observation Date	19-Oct-2014	14-Dec-2014
Frequency Coverage (GHz)	4.5-6.5	2.0-4.0
Array Configuration	C	C
On source Time	44 m 25 s	62 m 45 s

2.3.2 Calibration of the new JVLA datasets

In our work we analyzed two dataset at different frequencies from the same project (see tab. 2.1). In both the observations we used the same calibrators:

- 3C48 as flux and bandpass calibrator;
- J0016-0015 as phase calibrator;
- 3C138 as polarization calibrator;

The aim of these observations was the detection of the faint steep spectrum emission that would come from the arcs. Therefore, they were scheduled during the C-array configuration cycle of the JVLA, in order to maximize the sensitivity of the observations. In Fig 2.7 are reported the UVplane coverage of the observations, which show that the visibilities are clustered inside 4000 UVlenghts.
Both datasets required an accurate editing of the visibilities. We report a summarize of the calibration of each dataset:

- **5.5 GHz dataset:** this was the first dataset that we analyzed. The first time the editing was done only manually, removing the RFIs, that were especially present in the last spw, and the baselines that gave an erroneous response. We tried to develop the most conservative editing possible, by removing several baseline, channels and even some chunks of observation time, but avoiding to flag entire spectral windows (Fig. 2.10 shows the flag in the frequency that we were forced to do). The first maps that we obtained did not exhibit any trace of reliable diffuse emission, so this dataset was superficially studied at the first time. After we tested the automatic flag algorithms on the 3.0 GHz dataset, we tried the same procedures on this dataset, with unexpected results. The improve in the editing resulted in an enhancement of the sensitivity, thus allowing to observe the extended emission around the core;

- **3.0 GHz dataset:** this band is well-know to host the RFIs produced by the radio communication systems. For this reason was not a surprise to observe prominent RFIs in our dataset, as the one that was observed at 2.4 GHz (e.g. Fig. 2.12). In order to minimize the effect of the RFIs, the observation schedule must include an additional scan of the flux calibrator at 5.5 GHz. This observation is used by the JVLA technical observers to remove most of these interferences. Unfortunately, many of these RFIs survived this first calibration and corrupted the dataset. We were forced to remove the first pair of spw from every source to remove the most dangerous interferences (e.g. in Fig. 2.12 the corrected visibilities start at 2.4 GHz whereas the raw dataset cover from 2.0 to 4.GHz). Unfortunately, the visibilities were plenty of other small RFIs that required a more meticulous approach to be removed properly. We decided to try the automatic flag algorithms of CASA, `RFLAG` and `TFLAG`. These algorithms are designed especially to remove RFIs by flagging those visibilities that are located at more than a prefixed number of σ from the mean distribution in time or frequency. We found out that many interferences affect more the LL and the LR component than the others. Unfortunately, the heavy editing that we were forced to develop degraded the sensitivity to the polarized emission at 3.0 GHz.

The results of the calibration can be appreciated in Fig. 2.10-2.13, where we report the visibilities of A2626 before and after the editing and the calibration.

2.4 Imaging and Self-Calibration

2.4.1 Imaging

After the data reduction we proceeded to create the maps of the sources. The principle of the imaging, also called *clean&restore*, is that every diffuse radio source can be analyzed as a composition of multiple point-like sources (clean components, or CC). In each cycle the CCs are subtracted from the *dirty image*, which is the FT of the UVplane, to create the *residual map*, until only the *noise* (RMS) is left. Then the CCs, which have been convolved with a clean beam without secondary fringes, are gridded on the residual map to reconstruct the surface brightness of the radio source.
In CASA the imaging is performed by the task `CLEAN`, which offers many parameters to improve the final result. For our work we used the clean algorithm MS-MFS (multi-scale and multi-frequency) proposed by Rau and Cornwell (2011), a modified version of the Clark-Hogbom method (Högbom 1974) for the clean

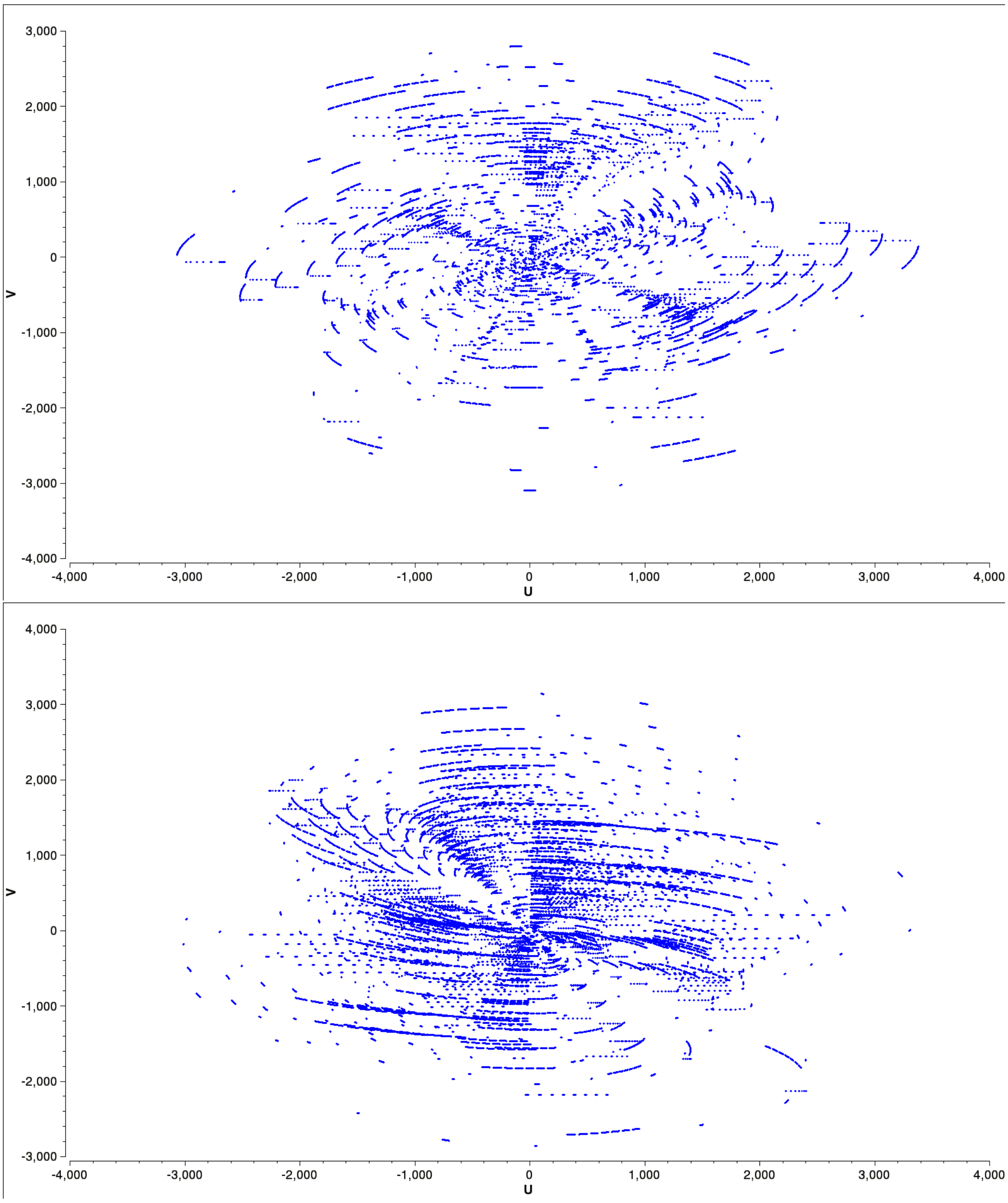

Figure 2.7: UVplane coverage of the observations in C (top) and S (bottom) band.

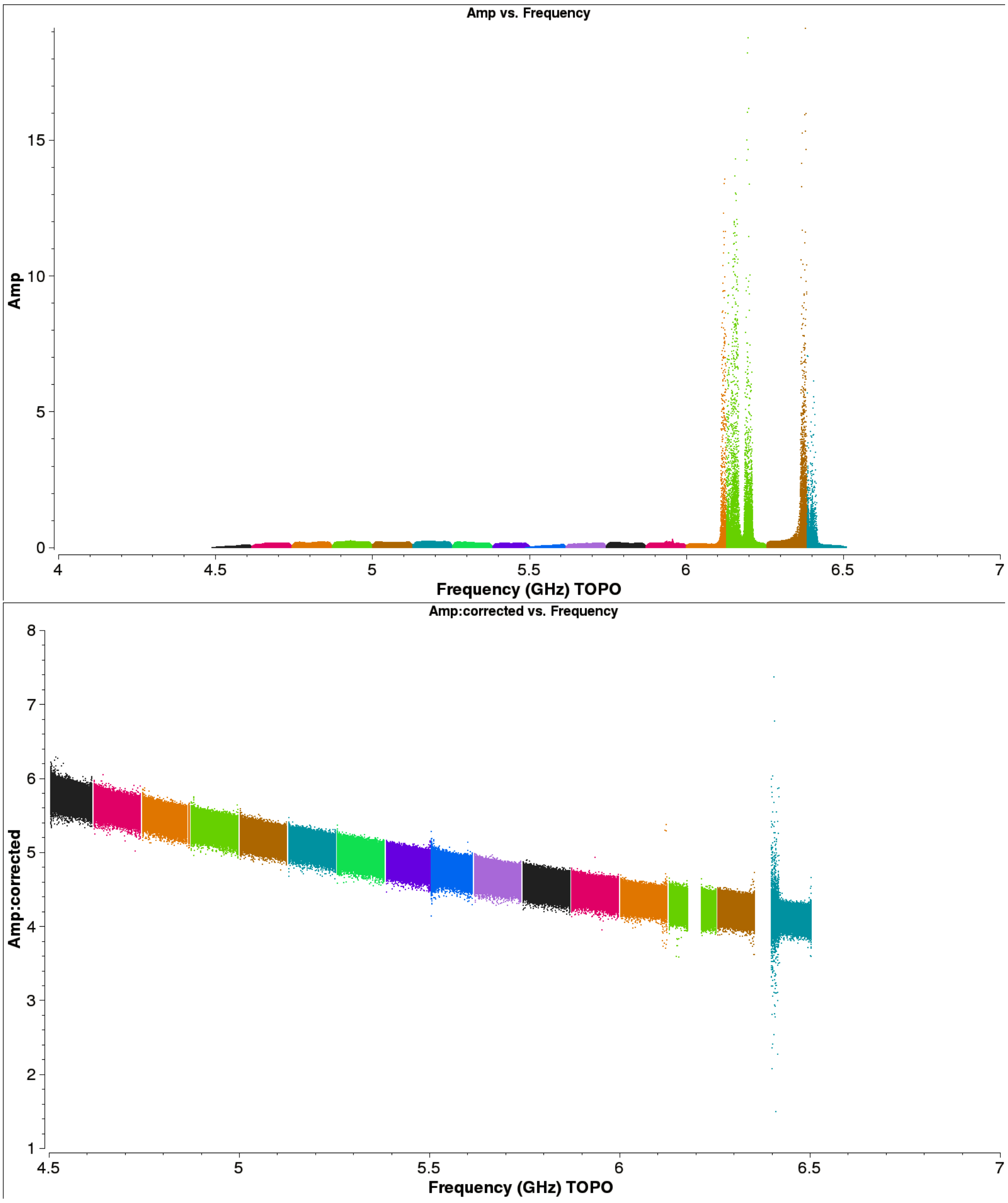

Figure 2.8: Amplitude vs Frequency plot for the Flux Calibrator 3C48 at 5.5 GHz before (top) and after (bottom) the calibration. Notice the change in amplitude level.

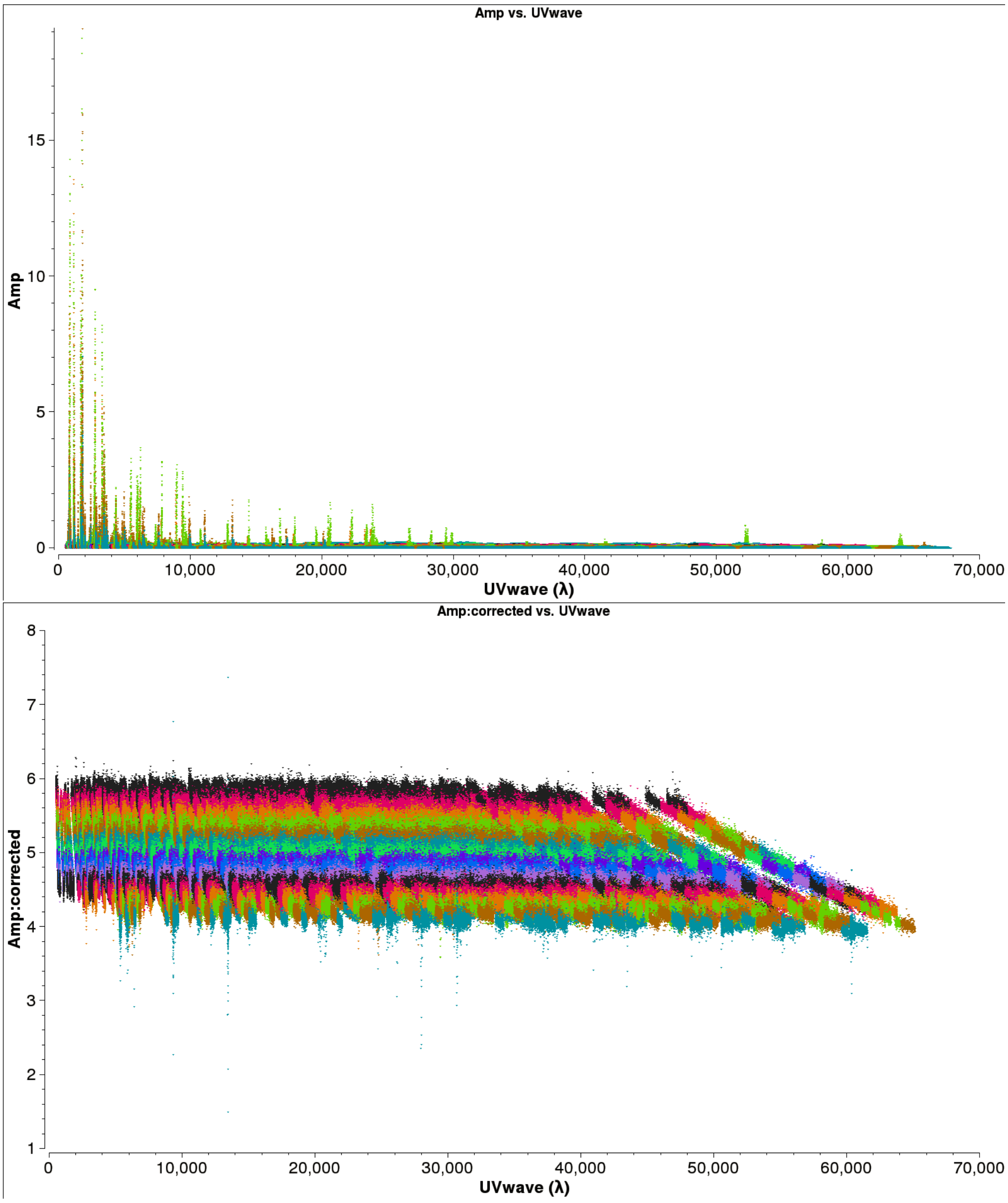

Figure 2.9: Amplitude vs UVdist plot for the Flux Calibrator 3C48 at 5.5 GHz before (top) and after (bottom) the calibration. Notice the change in amplitude level and the shape of the distribution, which resemble the theorical model in Fig. 2.6.

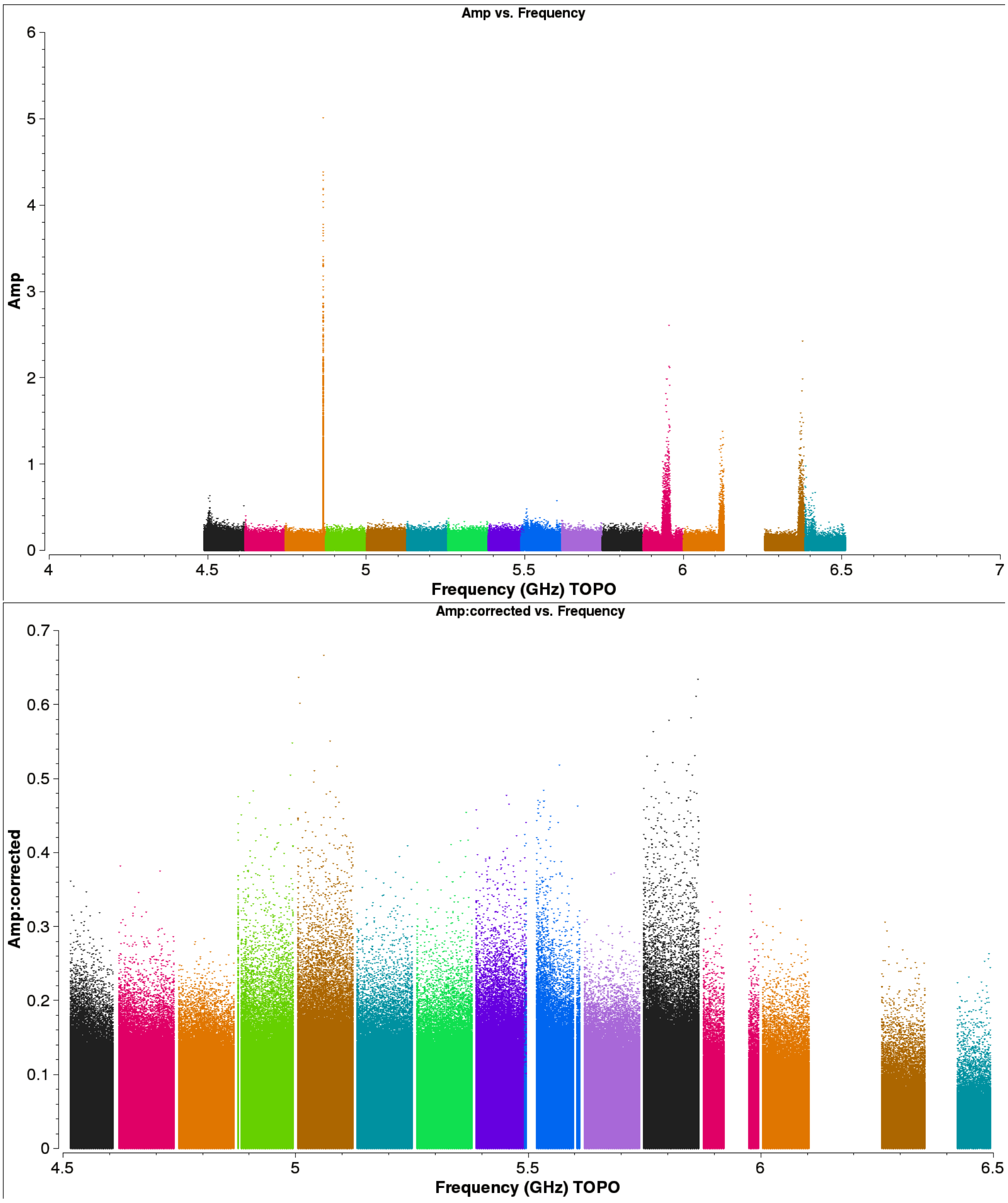

Figure 2.10: Amplitude vs Frequency plot for A2626 at 5.5 GHz before (top) and after (bottom) the calibration. Notice the change in amplitude level and the frequency chunk that we removed due to the presence of RFI.

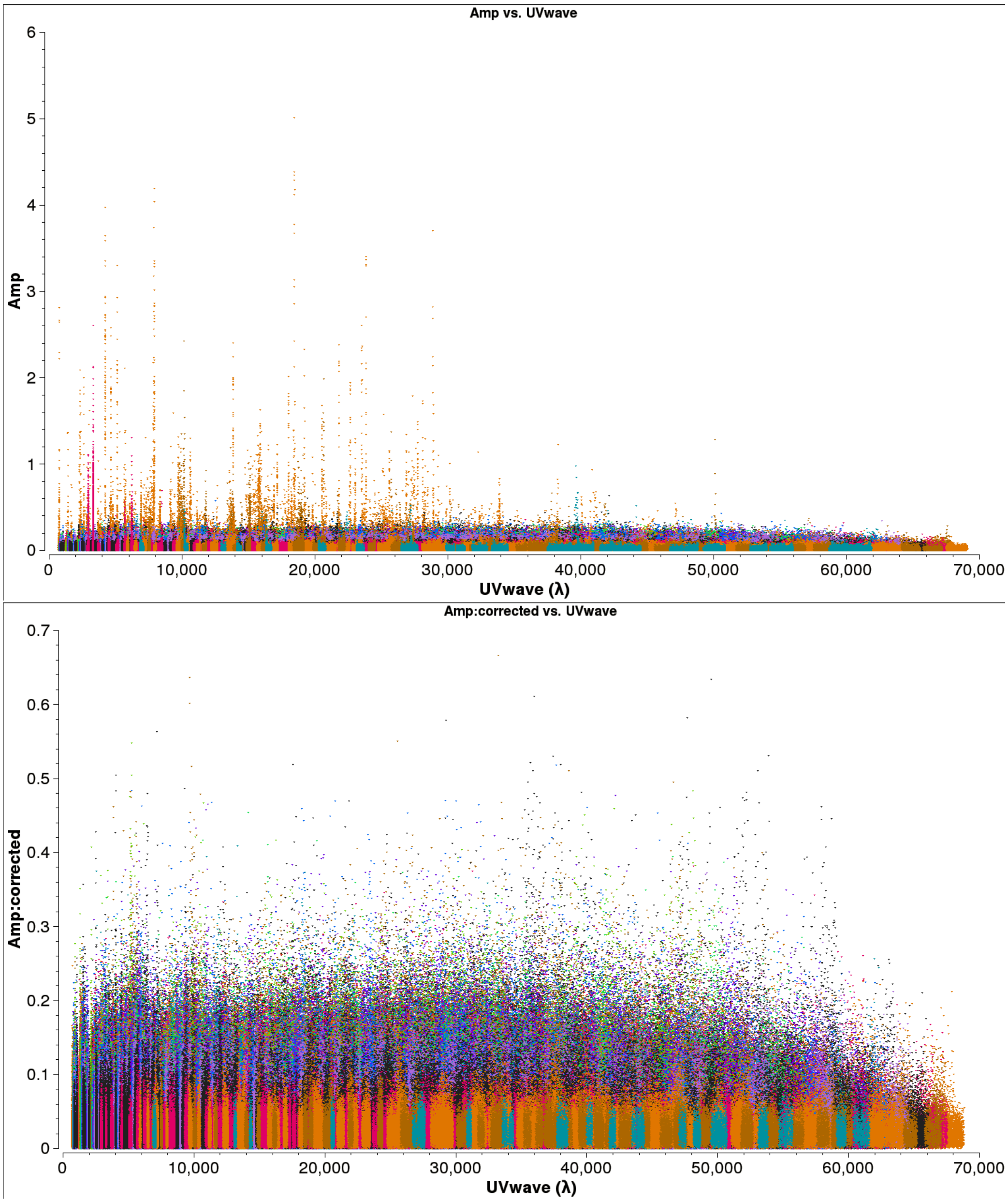

Figure 2.11: Amplitude vs UVdist plot for A2626 at 5.5 GHz before (top) and after (bottom) the calibration. Notice the change in amplitude level and the frequency chunk that we removed due to the presence of RFI.

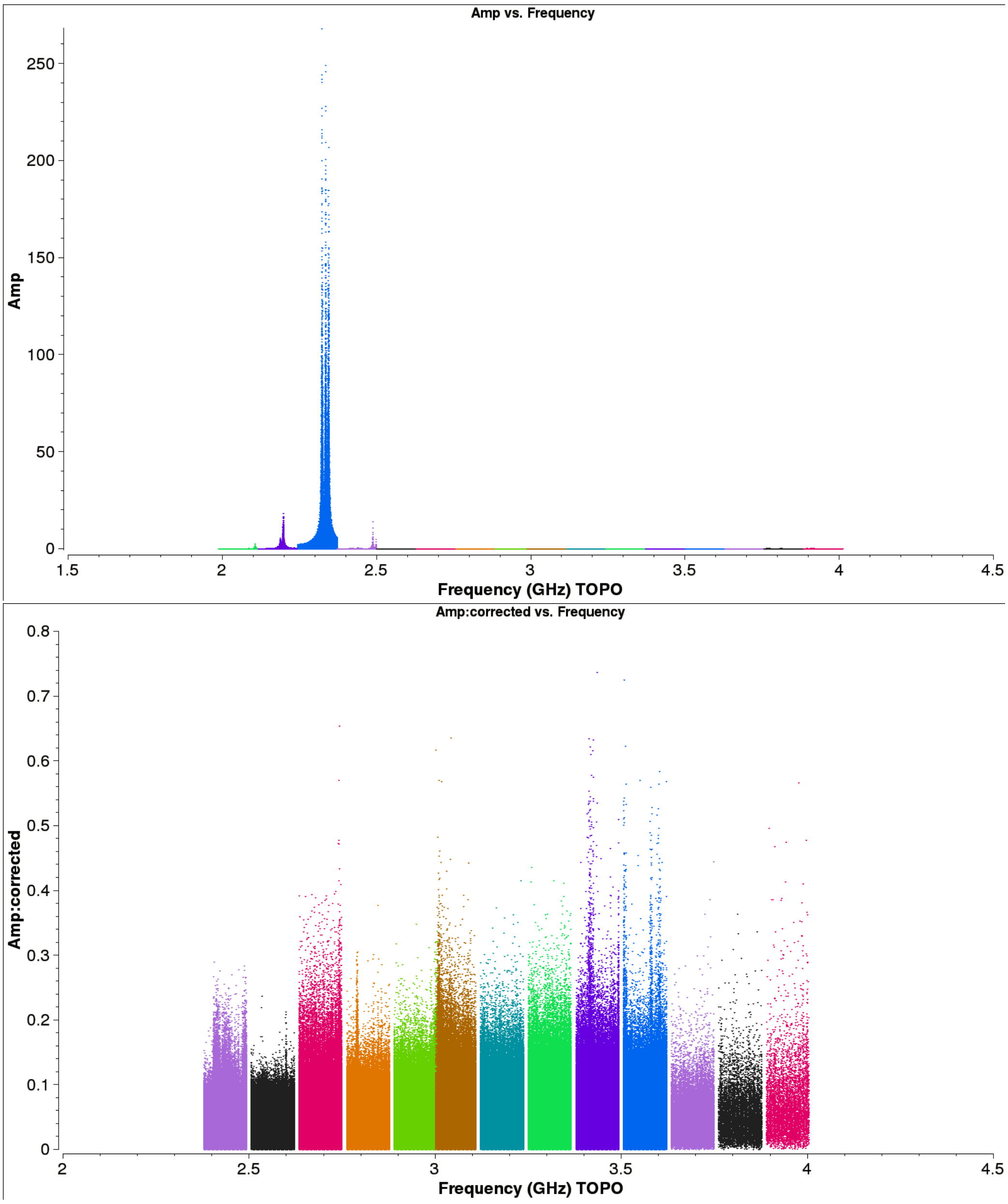

Figure 2.12: Amplitude vs Frequency plot for A2626 at 3.0 GHz before (top) and after (bottom) the calibration. Notice the change in amplitude level and the frequency chunk that we removed due to the presence of RFI. It is important to notice that, even if the RFI at 2.3 GHz (blue) looks like its is dominating the signal, each one of the other spectral windos had a signal above 10 mJy before the editing.

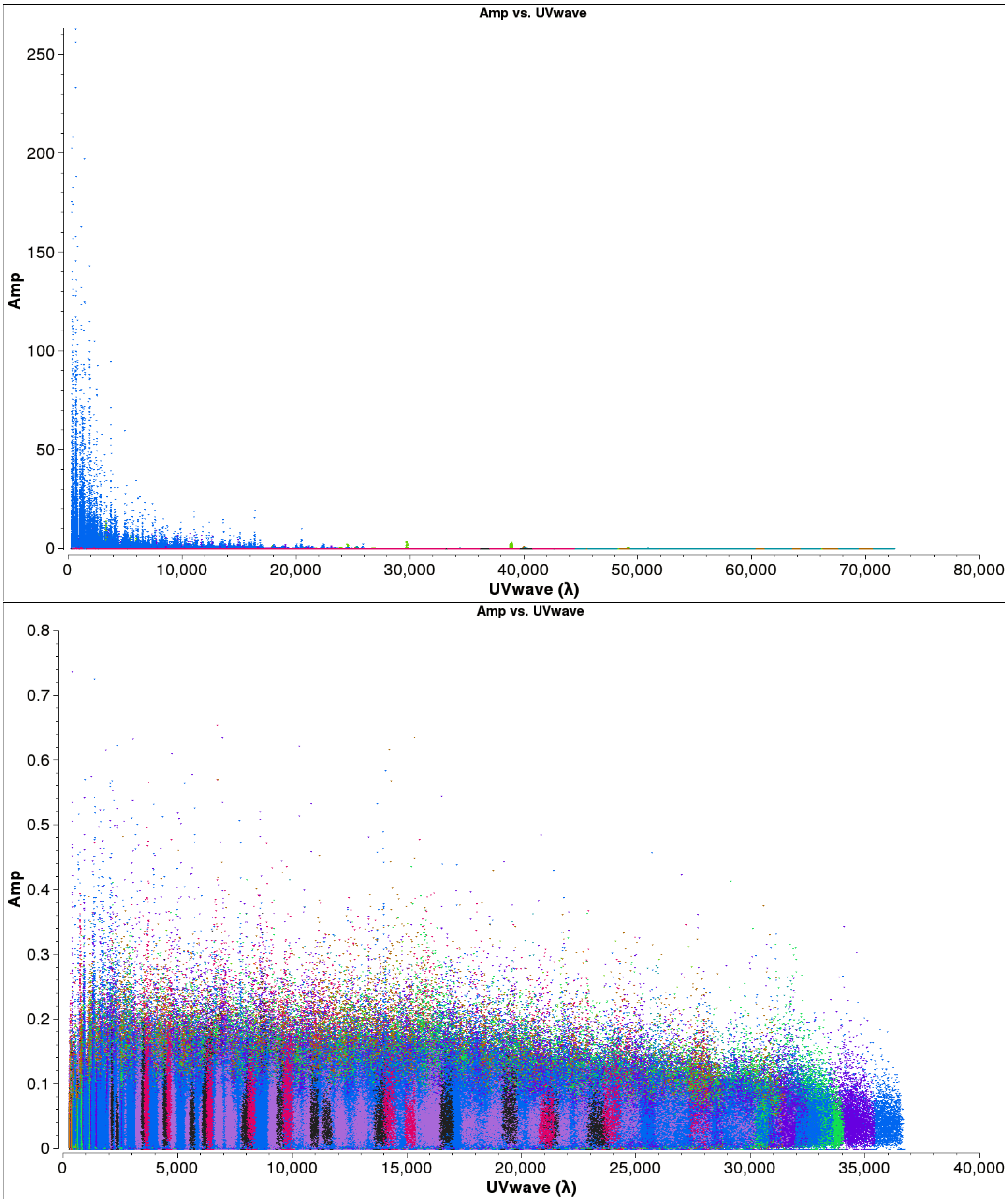

Figure 2.13: Amplitude vs UVdist plot for A2626 at 3.0 GHz before (top) and after (bottom) the calibration. Notice the change in amplitude level.

of radio images. The MS-MFS algorithm models the wide-band sky-brightness distribution as a linear combination of spatial and spectral basis functions, and performs image-reconstruction by combining a linear-least-squares approach with iterative χ^2 minimization. This method extends and combines the ideas used in the MS-CLEAN and MF-CLEAN algorithms for multi-scale and multi-frequency deconvolution respectively, and can be used in conjunction with existing wide-field imaging algorithms.
The most important parameters of CLEAN are:

- `Cellsize/Imsize`: these parameters define the size and the resolution in pixel of the image. `Cellsize` defines the dimension of a pixel in arcsec, while `Imsize` defines the size of the image in pixels. The correct sampling of the surface brightness depends on the Nyquist theorem, that states that the sufficient condition for a sampling to capture all the information from a continuous signal is that the sample rate would be at least one half of the signal period. In the case of the imaging the signal period is the beam width, that has to be sampled by a certain number of pixel. If one set the pixels to be greater than half of the beam, the image will not be sampled properly, degrading the resolution and causing a flux loss. On the other hand, a over-sampling does not produce errors in the image, but it will increase dramatically the computation time required to complete the task. We adopted a `Cellsize` equal to one fifth of the beam size. The `Imsize` should be the Field-of-View (FOV) of the observation, which is derived from the size of the antenna. `Imsize` and `Cellsize` compose the dimension of the image as:

$$FOV = 1.22\frac{\lambda}{D} \simeq \text{Size [arcsec]} = \texttt{Imsize}\ \text{[pixel]}\cdot\texttt{Cellsize}\ \text{[arcsec/pixel]} \tag{2.13}$$

- `niter/gain/threshold`: these parameters control the flow of the clean. `niter` defines the number of iterations, `gain` sets the fraction of the flux density in the residual image that is removed and placed into the clean model at each minor cycle iteration, and finally `threshold` defines a limit for the residual flux density, which will arrest the clean if it is reached. The threshold value is usually equal to the noise level σ_{RMS}, which is requested in the proposal of the observation, that depends on the observation time $\Delta\tau$ and the bandwidth $\Delta\nu$, as:

$$\sigma_{RMS} \propto \frac{T_{sys}}{\sqrt{\Delta\tau\Delta\nu}} \tag{2.14}$$

where T_{sys} is the *antenna temperature*, a measure of the noise produced by the hardware of the receiver, that is known from the technical properties of the radio telescope. The clean finishes when one of these criteria are met: it may completes the number of iteration defined by `niter`, it may clean residual until it reaches the threshold or it may simply not converge. A final RMS which is greater than the threshold means that the number of iterations was too small and it should be increased. Otherwise, a clean that do not converge implies that the parameters were incorrect or there were others problems in the input visibilities;

- `Stokes/psfmode:` it is possible to produce images in total and polarized intensity. To produce maps of total intensity we set `stokes=I` and `psfmode=clark` , while the polarization maps required `stokes=IQU` and `psfmode=clarkstokes`. When `psfmode=clarkstokes` the clean produces the vector map of the linear polarization in addition to the intensity map;

- `Interactive:` the clean results depend dramatically on the choice of the regions (boxes) where the algorithm collects the CCs. The success of the task depends on the signal-to-noise ratio (SNR) of the target, so bright sources are easily reconstructed by the clean, otherwise regions with faint diffuse emission could be distorted, or removed, if the clean is set to work on the wrong boxes. To avoid this problem, it is possible to place the boxes manually before each cycle of clean by setting `interactive=True`, otherwise the clean will work on the whole FOV. In interactive mode CASA will display the residual of the image after every cycle, so it is possible to control execution of the procedure in real time. The interactive boxing process has usually three steps: at the beginning the boxes should be placed only on the brightest sources, then they are extended on the diffuse emission. When the the task has collected the CCs of these component properly the remaining iterations should be carried out on a final box that covers the whole map.

- `Weighting/Robust:` when an image is produced the visibilities are multiplied by a factor, called weight, before they are gridded on the UVplane. The weight w_i is defined as:

  $$w_i = \frac{\omega_i}{1 + W_k f^2} \tag{2.15}$$

  where

  $$f^2 = \frac{(5 \cdot 10^{-R})^2}{\frac{\sum_k W_k^2}{\sum_i \omega_i}} \tag{2.16}$$

  ω_i is the inverse variance for all selected data, W_k is thee *gridded weight* and R is the value set by the parameter `Robust`. By changing the robust the clean changes its response on the visibilities, depending on their value of UVrange. The parameter weighting allows three modes: `BRIGGS` by the name of the inventor of the algorithm [1], where the weight is decided by the sub-parameter `ROBUST`, `NATURAL` or `UNIFORM`. In `UNIFORM` mode the clean uses the same weigh on every UVrange, so the image will be affected more by the longest baselines. This results in a better resolution but a worse sensitivity to the diffuse emission. On the other hand, the `NATURAL` mode enhance the response of the shortest baselines, deteriorating the resolution but improving the sensitivity. The Briggs mode allows to achieve every intermediate results between the `NATURAL` and the `UNIFORM` response by setting the Robust. `ROBUST=+2` will produce a weighting close`NATURAL` , `ROBUST=-2` corresponds to the `UNIFORM` mode. Every other weight is achieved by setting Robust between -2 and +2.

- `Nterms:` this parameter set the order of the polynomial which is used by the MS-MFS algorithm to reconstruct the spectrum of each component:

$$I_m^\nu = \sum_{t=0}^{N_t-1} \omega_\nu^t I_t^{sky} \text{ where } \omega_\nu^t = \left(\frac{\nu-\nu_0}{\nu_0}\right)^t \tag{2.17}$$

where N_t is the order of the Tylor series expansion set by `nterm`, ν_0 is the reference frequency of the observed band and I_t^{sky} represents a multi-scale Taylor coefficient image defined as:

$$I_\nu^{sky} = I_{\nu_0}^{sky}\left(\frac{\nu}{\nu_0}\right)^{I_\alpha^{sky}+I_\beta^{sky}log\left(\frac{\nu}{\nu_0}\right)} \tag{2.18}$$

where I_α^{sky} is the the average spectral index and I_β^{sky} is the spectral curvature. The motivation behind this choice of interpretation is the fact that synchrotron emission is usually observed, and modeled, as a power law distribution across frequencies. The optimal value of `nterm` depends strongly on the source: a bright radio source which exhibits a good RMS could be processed setting `nterm`=1, but when faint diffuse emission regions are involved the `nterm`=2-3 could be a better choice. By setting `nterm`>1 also the computation times increase exponentially, but in addition to the total intensity map the clean produces also a spectral index map, with relative errors (`nterm`=2) and a spectral curvature map (`nterm`=3).

- `Gridmode:` when the extension of the image is comparable with the FOV the curvature of the sky (W-term) is not negligible. The effects of the curvature affect those visibilities far away from the phase center, and they can

---

[1] http://www.aoc.nrao.edu/dissertations/dbriggs/

be corrected by using the W-Projection algorithm (Cornwell et al. 2008). This mode is activated by setting `gridmode=wprojection`: with this setting the program will use many planes to parametrize the sky curvature. The number of planes used is defined by the subparameter `wprojplanes`, which can be set on -1 to calculate the optimal number of planes to use.

- `Multiscale`: if the target shows emission on various scales it is possible to improve the response on these scale by setting the multiscale. The input of multiscale is an array of values (in pixel) which would stand for the emission scales. Since (usually) the emission scales of emission are unknown *a-priori*, the best way to find them is to repeat the clean many times by adding a new scale every time. A solid way to start is to set `multiscale=[0,5]`, which means that the clean will enhance the point-like (scale 0) and the beam-like components (scale 5, if the `cellsize` was set to be one fifth of the beam), then to add other components if thy are needed. If the multiscale is set wrong it may produce no improvements or it may modify the morphology of the source, which is the worst case scenario.

As the calibration process, also the imaging required an accurate study. Since we were interested in faint extended radio sources, the final results depended radically on the `CLEAN` parameters. So, we tested many combination of `nterms`, `MULTISCALE` and weighting and we compared the results.
We favoured the `NATURAL` or `ROBUST 0` clean to maximize the sensitivity of our maps. In our analysis we found many bright sources near A2626, whose secondary lobes dominated the map at the point that the faint emission of the arcs almost disappeared. So, in order to remove their fringes properly, we were forced to expand the `Imsize` beyond the FOV to cover an area of 32'x32' and we used the `nterms=2` (e.g. Fig 2.15). For each dataset we performed clean on various scales, attempting both `nterm` 1 and 2 to verify the improvement.
We found that setting robust $\neq 0$ when `nterm` > 1 produces unavoidably the divergence of the clean, and that combining `nterm`>1, wide-field gridding and multi-scale clean increases the computation times up to 30 hours, but it was indispensable to remove properly the beam artifacts around the bright unresolved sources. In order to complete the cleans despite the long computation times we used `Interactive=False`, which revealed to be reliable in restoring the morphology of the source. The final RMS of the maps produced with

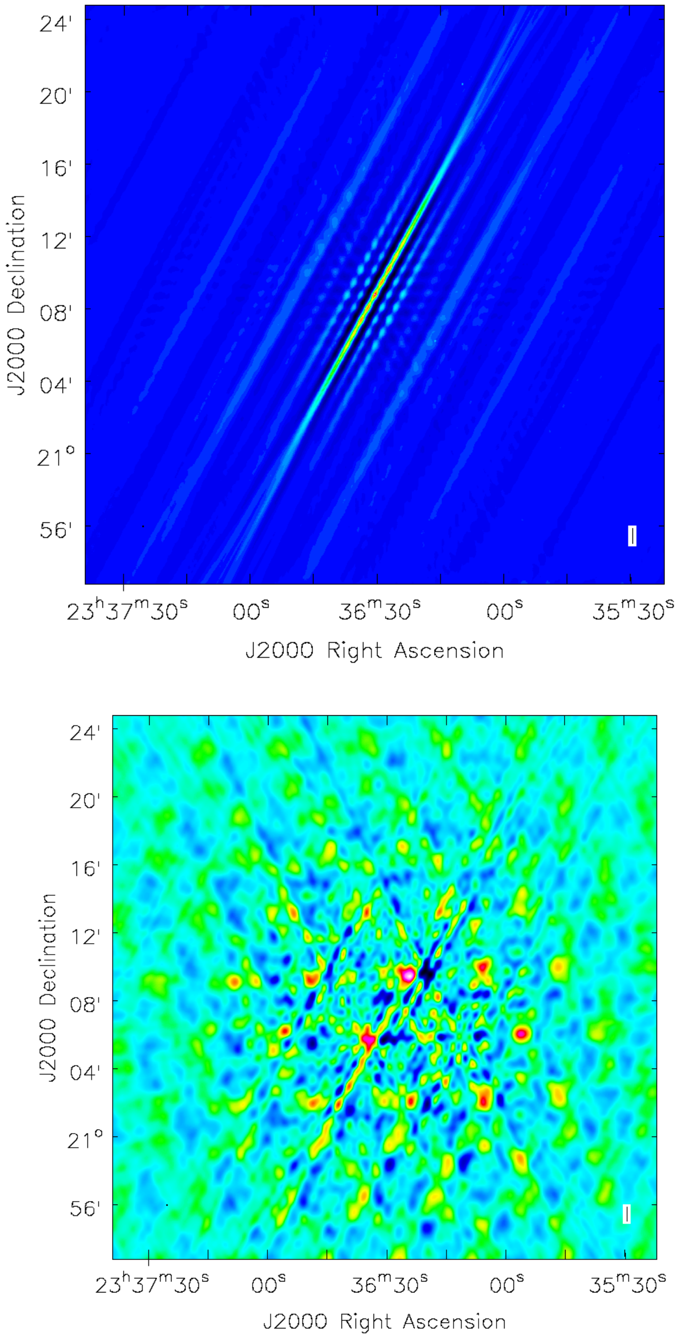

Figure 2.14: Some examples of what happen when the clean goes wrong. The top panel is the result of wrong setting of `MULTISCALE`, and the bottom one is an attempt to combine the `nterms` 2 with the `NATURAL` weighting: the mean flux density of the whole map is over 2000 Jy/beam, which means that the clean had amplified tremendously the real amplitude of the signal.

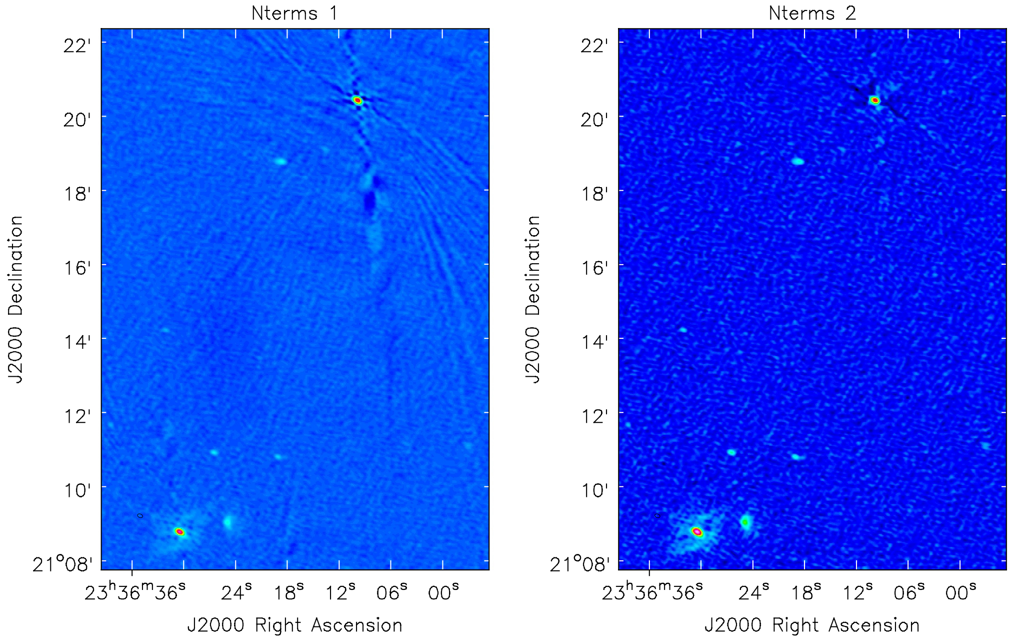

Figure 2.15: Result of a `ROBUST 0` clean with `nterms 1` (Left) and `nterms 2` (Right). The `nterms 2` clean improves dramatically the removal of the Beam artifacts, especially around the bright source located at North-West. The absence of these artifact improves, in turn, the sensitivity of the map, making the diffuse emission of A2626 more clear.

	Δt	RMS [μJy beam^{-1}]
C-band	300s	14.08
	150s	11.9
	120s	10.8
S-band	300s	74.6
	150s	73.7
	120s	72.9

Table 2.2: Improvement of the self-calibration on the dataset. We report the RMS values after every cycle of self-cal. The RMS level of the S-band is high because the imaging between each cycle was developed in `nterms=1` to reduce the computation time: for this reason the RMS level is affected by the secondary lobes of the background sources.

`Interactive=False` was comparable with the RMS of the maps that we produced interactively, and sometimes even smaller than it.
We developed also the polarized emission cleaning at 3.0 GHz. By setting `stokes=IQU`, we produced maps of every Stokes component I, U and Q. The Polarized intensity map P was computed from the U and Q maps as:

$$P = \sqrt{U^2 + Q^2} \tag{2.19}$$

whereas the Polarization vector map χ was obtained as:

$$\chi = \frac{1}{2} arcsec \left(\frac{U}{Q} \right) \tag{2.20}$$

2.4.2 Self-calibration

The A-priori calibration produces gains for the target by time-interpolating the corrections that were obtained for the phase calibrator. For this reason, these corrections are solid only on time-scales that are larger than the duration of the phase calibrator scans. But the ionosphere, which is the main cause of phase errors, can vary on time scales that are much smaller than these. The self-calibration is carried out to resolve this issue, by producing phase correction on short time scales Δt, based only on the target visibilities, thus improving its calibration. It is extremely useful when the target has weak extended emission on large scales. The self-calibration is able to improve the phase as though the amplitude gains.

The passages of a *Self-calibration cycle* are:

1. Imaging: by setting `usescratch=True` the `CLEAN` stores automatically the CCs and creates a model of the source from them. To ensure that the target model is based on the real emission of the source, the imaging between each cycle of self-calibration should not be too incisive, but it should instead be focused on collecting only the brightest CCs, that surely belong to the target.

2. Obtaining the new gains: it is possible to compute a new set of phase gains from the model, on a `solution interval` Δt that should be smaller than the duration of the phase calibrator scan;

3. Applying the calibration: the new gains are applied on the visibilities to obtain the self-calibrated dataset;

4. New Imaging: by creating a new map it is possible to estimate the improvement that was produced by the self-calibration.

A dataset may require multiple cycles of self-calibration. If the RMS level of the first image (the one that is used to produce the model of the source) is higher than the level of the image produced in the last step, it is possible to repeat the cycle. To improve the effect of the self-calibration each set of gains should be computed on a smaller Δt than the previous one. After several cycles, the RMS may stop to decrease, or it can even begin to increase, which means that the self-calibration is finished. The last model can be used also to compute the last set of amplitude gains.
We performed the self-calibration on both datasets, but for the 3.0 GHz dataset we includes also the U and Q emission in the model, in order to self-calibrate also the polarized emission. We report the results in Tab. 2.2. During the self-calibration of the 5.5 GHz dataset we were forced to remove the spw 13, which was yet reduced by the previous editing.

Chapter 3

Results of the new JVLA observations

After the data reduction and the imaging we proceeded with the scientific analysis of the radio emission of A2626. The aim of this work is to understand the physical process that created the radio arcs, whose properties differ from those of the common diffuse radio source observed in galaxy clusters. The reference model proposed is the jet-precession model by Wong et al. (2008), outlined in Chapter 1, which is based on the morphology of the arcs but it requires a quantitative confirmation. This confirmation may come from the radio spectral index map. Qualitatively, if the values of the spectral index of each arc show a clear variation trend along the arcs, then we can argue that they were created gradually by a moving source of relativistic plasma, like a precessing jet.

Starting from the total intensity maps (Fig. 3.2-3.7) we created the spectral index map of the cluster (Fig. 3.10-3.14). We combined the new observations at 3.0 and 5.5 GHz with the previous ones at 1.4 GHz and 4.8 GHz, that were presented in Gitti (2013), to compute the spectral index of the radio sources of A2626 in various configurations of resolution and sensitivity. Finally, we analyzed the variation of the spectral index (Fig. 3.16-3.18) on these maps.

3.1 The new JVLA maps at 3.0 and 5.5 GHz

We produced several maps with different resolutions and sensitivities. During the clean we were able to test the effectiveness of the MS-MFS algorithm in the imaging of the diffuse emission. We produced several maps by setting `UNIFORM`, `ROBUST 0` and `NATURAL` weighting, with various combination of `nterms`, `UVTAPER` and `MULTISCALE`. We were able to use `nterms=2` only with the `ROBUST 0` weighting, otherwise the clean failed to reconstruct the surface brightness. After several attempts, we adopted the largest value of multiscale

Table 3.1: List of Total Intensity maps

Figure	Frequency [GHz]	Weighting	`nterm`	Beam size [arcsec]	RMS [μJy beam^{-1}]
3.1	5.5	`UNIFORM`	1	2.8 x 2.7	16.1
3.2	5.5	`ROBUST 0`	2	3.2 x 2.8	8.0
3.3	5.5	`NATURAL`	1	4.9 x 4.4	8.6
3.5	3.0	`UNIFORM`	1	7.5 x 8.5	40.1
3.6	3.0	`ROBUST 0`	2	8.7 x 5.8	20.4
3.7	3.0	`NATURAL`	1	13.1 x 8.5	18.5

considering that that the spatial scale of the diffuse emission was comparable with the resolution of our map, so we set `MULTISCALE=[0,5]` in each map to improve the outcome of the clean. We report in Tab. 3.1 the properties of each map. In each map the contours level are at -3,3,6,12,24·RMS. For the name of the components of the radio emission we refer to Fig. 1.6.

3.1.1 5.5 GHz (C-band) maps

In the 5.5 GHz maps (Fig.3.1-3.3) we reached an unprecedented level of sensitivity, with an RMS of ∼8 $\mu Jy/beam$ in every map, that is the value that was requested in the observation proposal. Due to the high sensitivity, we detected the faint extended emission of IC5338 and IC5337, that was yet unobserved at this frequency.

The `UNIFORM` map exhibits the cores of IC5338 and IC5337. There are several small patches of emission around IC5338, but they are likely to be residuals of the primary beam. The `ROBUST 0` (Fig.3.2) exhibits the radio cores of the galaxies, but also a couple of jet-like features around the core of IC5338 and the emission of the trail of IC5337. The jet-like features coincide with the jets observed in 2013 at 1.4 GHz in the high resolution map (Fig. 1.6, Gitti (2013)), but they are degraded by the lower resolution of our map. Finally, the `NATURAL` maps shows evidence of extended emission around the core of IC5338. In the comparison between the diffuse emission at this frequency and the position of the arcs at 1.4 GHZ (Fig.3.4), the emission seems to connect each arc to the core of the cluster.

Finally we report that the flux of the core of IC5338 in this band differs from the values measured in Gitti (2013). We measure 6.2±0.2 mJy while they report a flux density of 9.6±0.3 mJy. After many tests on the flux scale calibration of each observation we tend to exclude that this difference is given by a dif-

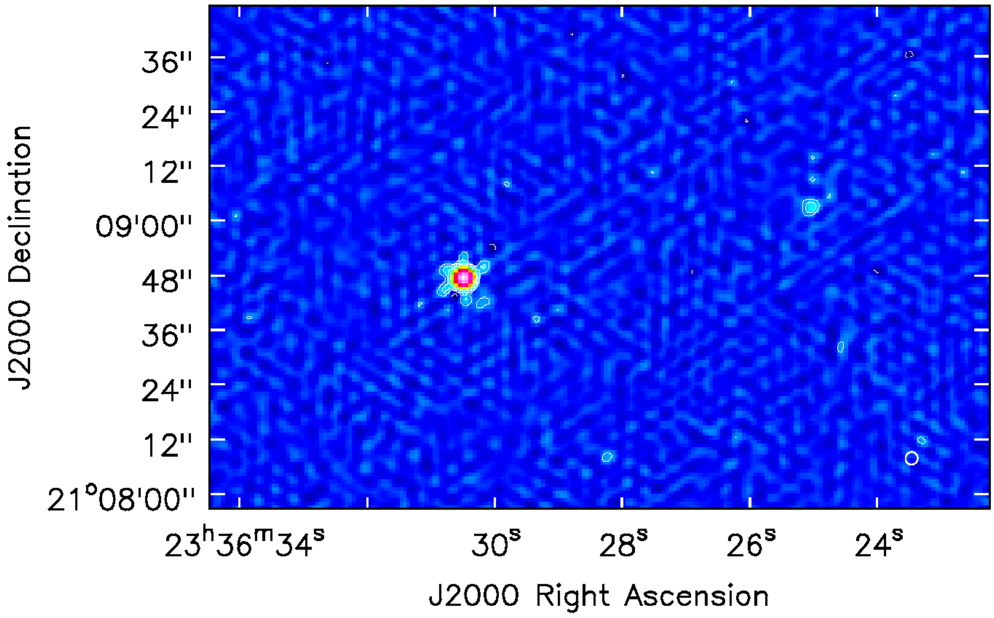

Figure 3.1: 5.5 GHz image obtained by setting `UNIFORM`, `nterms=1`. The beam size is 2.8''x2.7''. The RMS is 16.1 μJy beam^{-1} and the contours levels are -3,3,6,12,24·RMS.

ferent response of the interferometer, but we argue that it may be a probe of an intrinsic variability of the radio emission of the core. The observations were performed, respectively, in 2009 and 2013, thus we argue that the radio core has a variability time-scale shorter than four years. This is typically observed in the active radio galaxy (e.g. Barvainis et al. 2005). The diffuse emission of IC5337, that was observed only at 1.4 GHz, shows sign of a curvature (Fig. 3.2) which is clear in Fig. 1.6. The shape of its emission hints that the relativistic plasma of the galaxy is interacting with the hot medium of the cluster, which exercises a pressure equal to:

$$P = \rho_{ICM} V_{gal}^2 \tag{3.1}$$

where ρ_{ICM} is the density of the ICM and V_{gal} is the velocity of the galaxy respect to the cluster. This pressure, which is also called *Ram Pressure*, is able to warp the cold gas of a galaxy and the deformation of the plasma depends on the direction of the motion (Feretti et al. 1992). The morphology that we observed agrees with the result of Cava et al. (2009), that stated that this is a $jellyfish$ galaxy, a class of galaxies which cold gas is being stripped out by the interaction with the ICM.

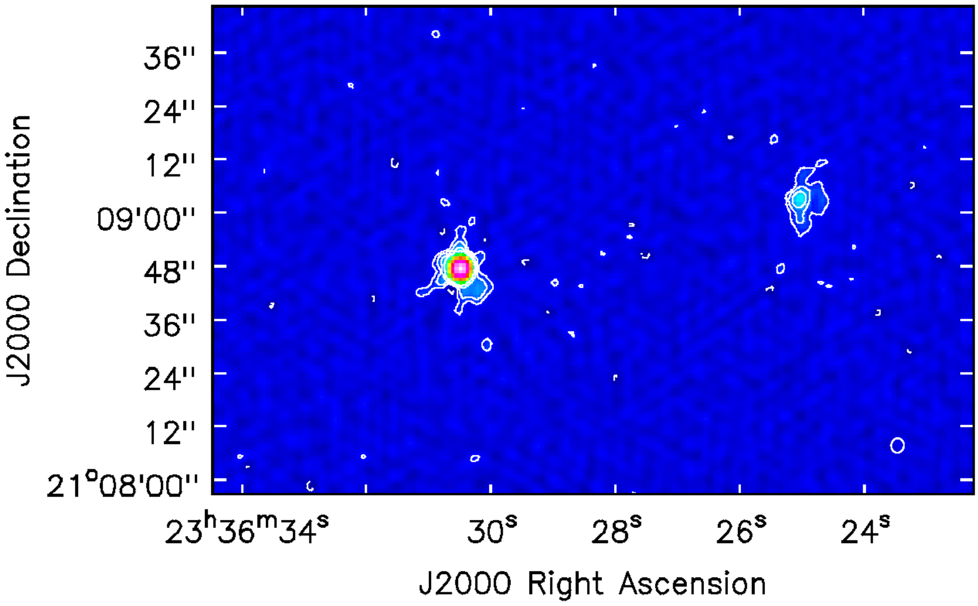

Figure 3.2: 5.5 GHz image obtained by setting `ROBUST 0`, `nterms=2`. The beam size is 3.2''x2.8''. The RMS is 8.0 μJy beam^{-1} and the contours levels are -3,3,6,12,24·RMS.

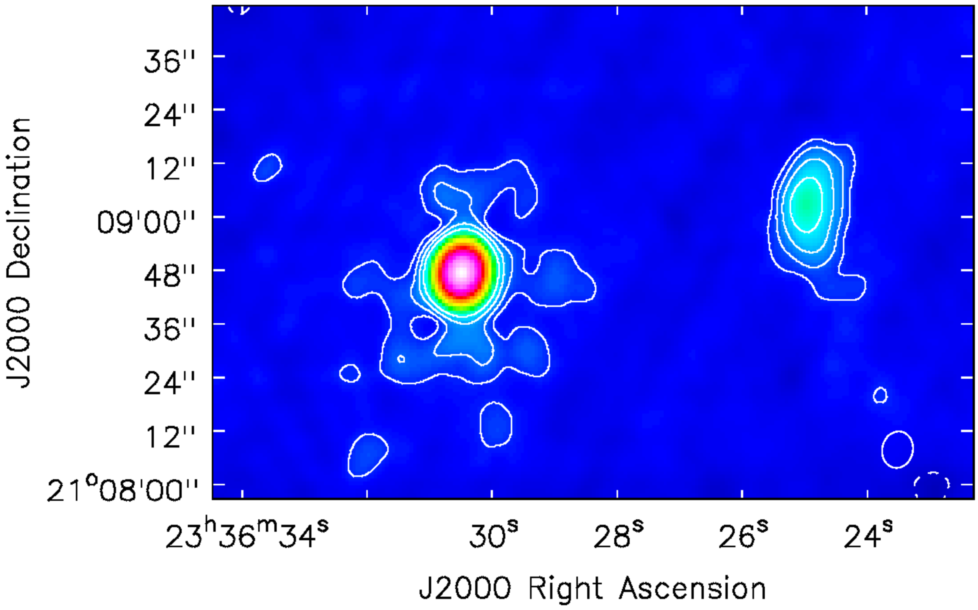

Figure 3.3: 5.5 GHz image obtained by setting `NATURAL`, `nterms=1`, `UVTAPER=[0,20]`. The beam size is 4.9''x4.4''. The RMS is8.6 μJy beam^{-1} and the contours levels are -3,3,6,12,24·RMS.

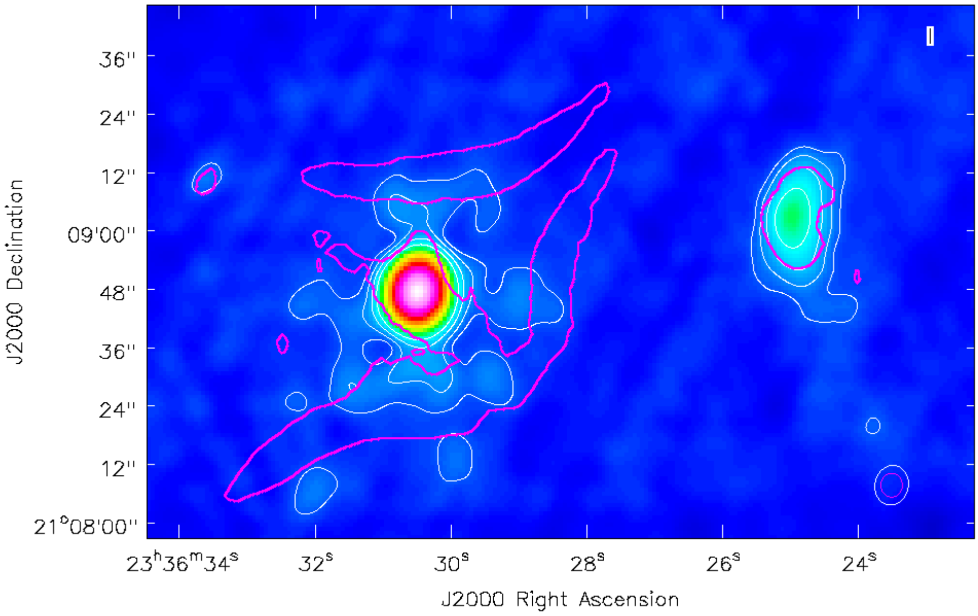

Figure 3.4: Comparison of the diffuse emission at 5.5 GHz (white) and 1.4 GHz (magenta).

3.1.2 3.0 GHz (S-band) maps

The 3.0 GHz dataset required a drastic editing which affected dramatically the final sensitivity of the maps. The maps have a RMS>18 μJy beam^{-1}, whereas the observation was requested to achieve a RMS= 7 μJy beam^{-1}. Nevertheless, we succeed to detect the arcs in both the `NATURAL` (Fig.3.7) and the `ROBUST 0` (Fig.3.6) maps. At this frequency, due to the low resolution, we could not resolve the jets from the core. In the `UNIFORM` map there are no clear evidence of extended emission around IC5338, but instead IC5337 exhibits diffuse emission with curved shape, in agreement with the previous results. In the `ROBUST 0` map (Fig. 3.6) the emission comes from several patches that coincide with the position of the arcs, furthermore we detect emission also from the eastern part of the cluster, where Kale and Gitti (2017) detected a fourth arc at 610 MHz. The `NATURAL` map (Fig. 3.7), due to the high sensitivity to the diffuse emission, displays the extended structure of the cluster, which is composed only by the core and an extended emission characterized by a diamond-like shape. It is interesting to notice that the 6 σ contour denotes a *S-like* morphology where the north and south arcs and the inner emission are assembled together, suggesting that they are only one diffuse radio source. The results of the polarization estimates do not provide strong constrains. We measure a polarized flux of 0.2±0.1 mJy from the

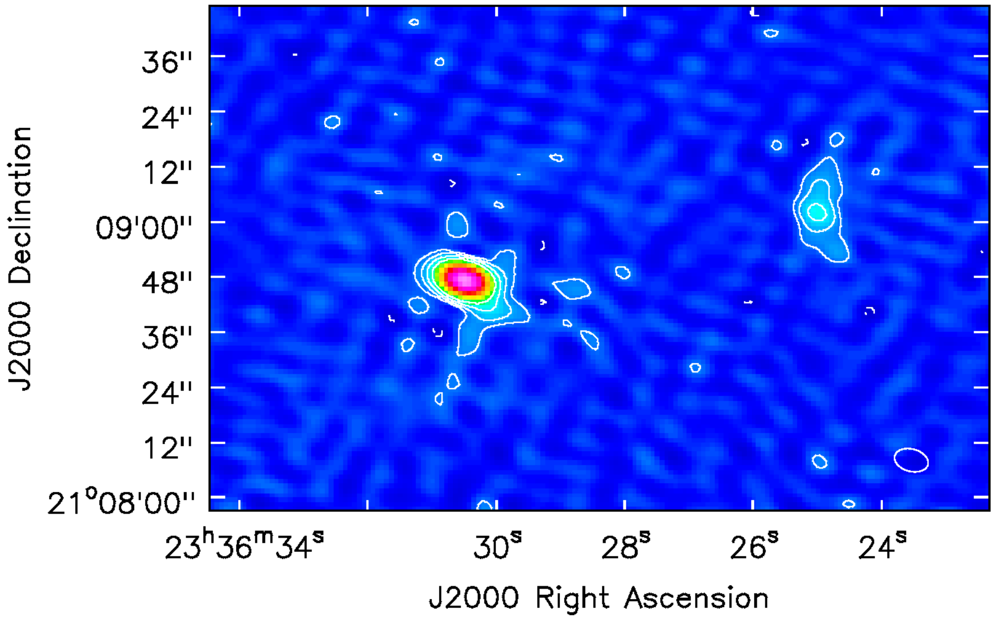

Figure 3.5: 3.0 GHz image obtained by setting `UNIFORM`, `nterms=1`. The beam size is 7.5"x8.5". The RMS is 40.1 μJy beam^{-1} and the contours levels are -3,3,6,12,24·RMS.

core, which corresponds to a polarization fraction of $\sim 2\%$, whereas the others components appeared to be not polarized. We believe that the severe editing that we conducted on the visibilities reduced the sensitivity to the polarized emission. We could only find an upper limit to the polarized emission fraction. The polarized intensity map P has an RMS σ_P of 27.3 μJy beam^{-1}, so, the peak of the surface brightness of the arcs I ~180 μJy beam^{-1} would have a polarization fraction$> 3\sigma_P/I \simeq 0.4$ to be obsersed above the 3σ level. It is important to notice that we were forced to use the `NATURAL` weighting to detect the arcs, but, due to the low resolution, our polarization map suffered from the *beam depolarization effect*, which further decreased the sensitivity to polarized emission.

3.1.3 Flux densities estimates

We report the flux densities of the radio sources of the cluster on each map in Tab. 3.2. Our results point out that the radio emission of A2626 is totally dominated by the core of IC5338.

In order to estimate the synchrotron spectra of each component, we compared their flux densities at 1.4, 3,0 and 5.5 GHz. The spectral index between two

Table 3.2: Flux Density values for each map.

Weighting	Component	Flux density [mJy]
	5.5 GHz maps	
`UNIFORM` (Fig. 3.1)	Total	6.7±0.2
	Core+jets	6.7±0.2
	IC 5337	0.2±0.1
`ROBUST 0` (Fig. 3.2)	Total	7.4±0.2
	Core+jets	6.0±0.2
	IC 5337	0.5±0.1
`NATURAL` (Fig. 3.3)	Total	8.2±0.2
	Core+jets	6.2±0.2
	IC 5337	0.5±0.1
	3.0 GHz maps	
`UNIFORM` (Fig. 3.5)	Total	12.1±0.5
	Core+jets	11.7±0.4
	IC 5337	1.6±0.3
`ROBUST 0` (Fig. 3.6)	Total	14.6±0.4
	Core+jets	12.0±0.4
	Arc Noth	0.4±0.1
	Arc South	0.5±0.1
	Arc West	0.5±0.1
	IC 5337	1.5±0.1
`NATURAL` (Fig. 3.7)	Total	16.5±0.5
	Core+jets	10.9±0.3
	Arc Noth	0.7±0.1
	Arc South	0.8±0.1
	Arc West	0.4±0.1
	IC 5337	2.2±0.1

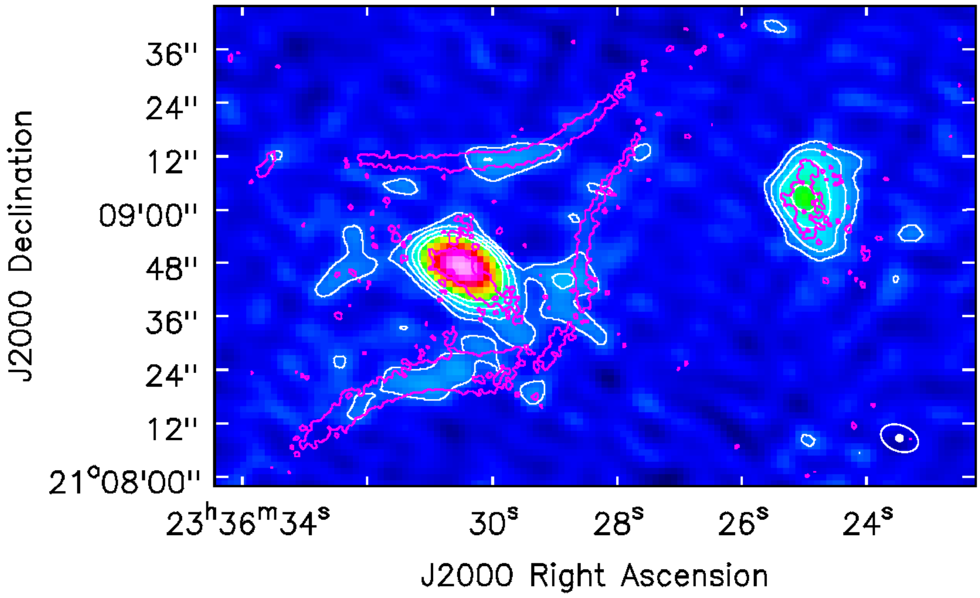

Figure 3.6: 3.0 GHz image obtained by setting `ROBUST 0`, `nterms=2`. The beam size is 8.7"x5.8". The RMS is 20.4μJy beam^{-1} and the contours levels are -3,3,6,12,24·RMS. The purple contours are the 3σ level of the 1.4 GHz map by Gitti (2013)

observed frequencies ν_1 and ν_2 is defined as:

$$\alpha_{\nu_1}^{\nu_2} = \frac{log(S_2) - log(S_1)}{log(\nu_2) - log(\nu_1)} \pm \frac{1}{ln(\nu_2) - ln(\nu_1)} \sqrt{\left(\frac{\sigma_1}{S_1}\right)^2 + \left(\frac{\sigma_2}{S_2}\right)^2} \tag{3.2}$$

where $S_1 \pm \sigma_1$ and $S_2 \pm \sigma_2$ are the flux densities measured at, respectively, ν_1 and ν_2.

The fluxes were measured on map that were created purposely for these estimates (see Appendix B), because, due to the different UVplane coverage, the JVLA and VLA observation were not intrinsically comparable. The adapted maps were produced by setting the same UVrange (0-40 kλ), restoring beam ($13''.1 \times 8''.5$ arcsec) and baseline weighting (`NATURAL`). Then we measured the flux of each components on the same regions, enclosed by the 7σ contours of the 1.4 GHz map. The results are reported in Tab.(3.3). In Tab. 3.4 we report also the monochromatic radio power P_ν of the sources:

$$P_\nu = 4\pi D_L^2 S_\nu (1+z)^{-\alpha-1} \tag{3.3}$$

that may be written as:

$$P_\nu = 1.1 \cdot 10^{17} \left(\frac{D_L}{[\text{Mpc}]}\right)^2 \left(\frac{S_\nu}{[\text{mJy}]}\right) (1+z)^{-\alpha-1} \text{ Watt Hz}^{-1} \tag{3.4}$$

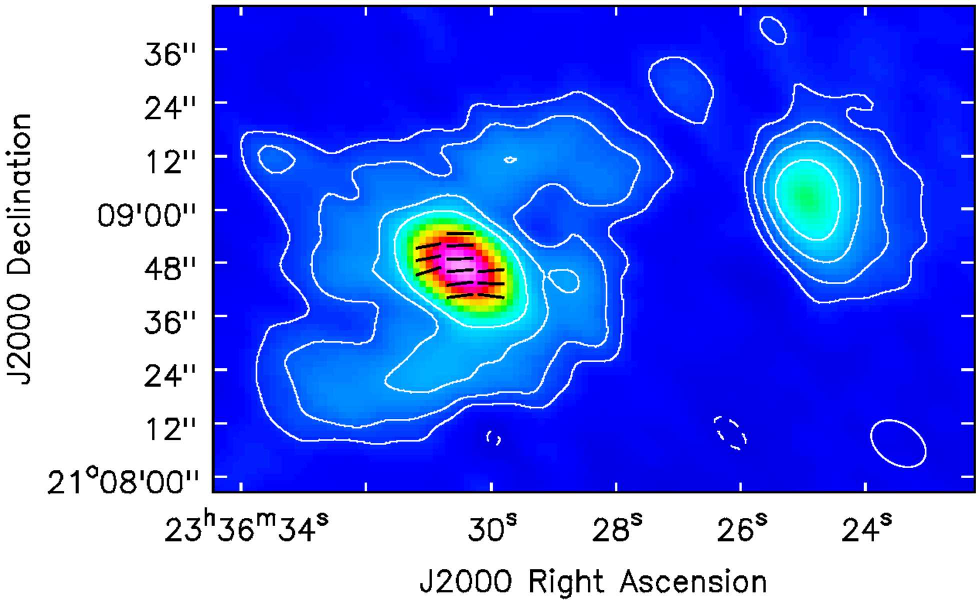

Figure 3.7: 3.0 GHz image obtained by setting `NATURAL`, `nterms=1` and `UVTAPER=[0,20]`. The beam size is 13.1"x8.5". The RMS is 18.5 μJy beam^{-1} and the contours levels are -3,3,6,12,24·RMS. In black there are the vectors of the polarized emission.

Table 3.3: Synchrotron spectra of the radio sources of A2626

Source	$S_{1.4}$ [mJy]	$S_{3.0}$ [mJy]	$S_{5.5}$ [mJy]	$\alpha_{1.4}^{3.0}$	$\alpha_{3.0}^{5.5}$	$\alpha_{1.4}^{5.5}$
Core+jets	18.6±0.6	10.6±0.3	7.2±0.2	-0.7±0.1	-0.7±0.1	-0.7±0.1
Arc North	5.8±0.2	0.7±0.1	-	-2.8±0.1	-2.2±0.2	-3.1±0.2
Arc South	7.6±0.2	1.1±0.1	-	-2.5±0.2	-2.7±0.2	-3.1±0.2
Arc West	1.6±0.1	0.3±0.1	-	-2.2±0.1	-2.4±0.2	-2.5±0.2
Total	42.2±1.2	17.5±0.5	8.0±0.2	-1.2±0.1	-1.3±0.1	-1.2±0.1
IC5337	1.8±0.2	1.1±0.2	0.4±0.1	-0.6±0.1	-1.7±0.1	-1.0±0.1

Table 3.4: Monochromatic radio power of the radio sources of A2626

Source	$P_{1.4}$ [10^{22} Watt Hz^{-1}]	$P_{3.0}$ [10^{22} Watt Hz^{-1}]	$P_{5.5}$ [10^{22} Watt Hz^{-1}]
Core+jets	12.2	6.9	4.7
Arc North	4.3	0.5	-
Arc South	5.5	0.8	-
Arc West	1.1	0.2	-
Total	28.5	11.8	5.4
IC5337	1.2	0.7	0.3

where D_L is the luminosity distance of the cluster, S_ν is the flux density at the frequency ν and $(1+z)^{-\alpha-1}$ is the *k-correction* term (Petrosian and Dickey 1973).

When no emission is detected at 5.5 GHZ, we estimate an upper limit of the spectral index, based on the flux density difference between the flux peak at 3.0 GHz and the 3σ level at 5.5 GHz.

The total emission of A2626 is dominated by the core up to 1.4 GHz, whereas the contribute of the arcs increases from 10% at 3.0 GHz t0 $\sim 40\%$ at 1.4 GHz (e.g. Fig. 3.8). The core has a flat radio spectrum, as it is expected from a compact radio core. The nucleus is defined as the region of the radio source where the plasma stops to auto-absorb the synchrotron emission, and begins to emit with a flat spectrum. The intrinsic variability of the core encourages us to rely more on the spectral index evaluated between 3.0 and 5.5 GHz than the other, due to the shorter period between the observations. On the other hand, the steep spectrum of the arcs is in agreement with the results of Kale and Gitti (2017). They argued that the arcs have a spectral index $\alpha = -3$ between 0.6

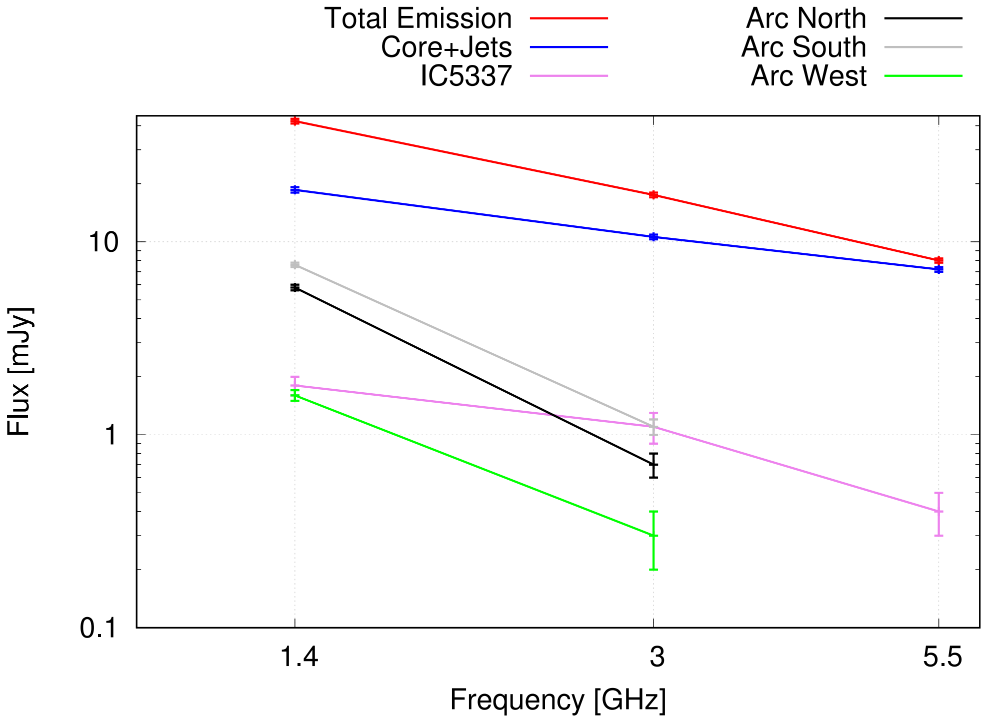

Figure 3.8: Radio spectra of the components reported in Tab. 3.3

Table 3.5: Estimated properties of the residual diffuse emission

	1.4 GHz	3.0 GHz	5.5 GHz
S_ν [mJy]	8.6	4.8	0.8
P_ν [10^{22} Watt Hz^{-1}]	5.7	3.4	0.6
	$\alpha_{1.4}^{3.0}$=-0.7	$\alpha_{3.0}^{5.5}$=-2.9	$\alpha_{1.4}^{5.5}$=-1.7

and 1.4 GHz, so, based on our results, we can suppose that the radio arcs have a steep spectrum from 0.6 to 3.0 GHz.

Finally, by subtracting the flux of each component from the total flux, we evaluated the contribute of the residual diffuse emission at each frequency, that may correspond to the putative mini-halo discussed by Gitti (2013). We report its estimated properties in Tab.3.5.

3.2 Spectral Index maps

By combining multi-frequency maps of the same objects it is possible to create a *spectral index map*. Spectral index images of the diffuse radio sources represent a powerful tool to understand their formation and evolution, and their connection to the cluster processes. Systematic variations of the radio spectral index can be associated to changes of the local magnetic field strength and/or modifications of the energy spectrum of the synchrotron electrons (Brunetti et al. 2001), which is intrinsically related to the radiative time of the population.

In a spectral index map the value of each pixel is the outcome of Eq. 3.2, where the flux densities of each pixel are evaluated on the total intensity maps. We computed the spectral index only with the pixels whose surface brightness value was above the 3σ level to exclude low-significance regions. This imposition produced a systematic effect on the maps. Due to the similar RMS of the total intensity maps, the edges of the emission regions have the same flux densities at each frequency, thus they appear to have an extremely flat spectral index. So we rejected the edges from the following analysis. This operation was carried out with the CASA task `immath`, which performs mathematical operations between images.

We used four datasets to produce the spectral index maps: the new JVLA observations at 5.5 and 3.0 GHz and the VLA observations at 4.8 and 1.4 GHz. Due to the different UVplane coverage, we were forced to degrade the VLA observations to compare them with the JVLA ones. This operation produced a loss of the information on the small spatial scales, therefore we focused our analysis on the

Table 3.6: List of spectral index maps

Figure	Frequencies [GHz]	Weighting	Beam size [arcsec]	UVrange [Kλ]
3.9	1.4_{VLA}-3.0_{JVLA}	`NATURAL`	13.1x8.5	0-40
3.10	1.4_{VLA}-3.0_{JVLA}	`ROBUST 0`	8.7x5.8	0-40
3.11	1.4_{VLA}-5.5_{JVLA}	`ROBUST 0`	3.2x2.9	0-68
3.12	1.4_{VLA}-4.8_{VLA}	`ROBUST 0`	1.6x1.5	0-170
3.13	1.4_{VLA}-5.5_{JVLA}	`NATURAL`	13.1x8.5	0-40
3.14	3.0_{JVLA}-5.5_{JVLA}	`NATURAL`	13.1x8.5	0-40

large scale extended emission. Due to the visibilities loss, the RMS level of the 1.4 GHz maps increased from $\sim$12 μJy beam^{-1} to 29 μJy beam^{-1}.
The available datasets allowed us to investigate the spectral properties of the arcs (Fig. 3.9-3.10), the inner diffuse emission (Fig. 3.13-3.14) and the jet-core complex of IC5338 (Fig. 3.11-3.12). In Tab. 3.6 we report the properties of each spectral map. See Appendix B for the input maps of each spectral index map.

In the `NATURAL` spectral index maps (Fig. 3.9) we identified two main sub-structures: the arcs, which have a steep spectrum, and the inner emission, which is dominated by the core, with a flat spectral index. The steep spectra of the arcs agree with the results of Kale and Gitti (2017), who measured a spectral index $\alpha \sim -3$ between 610 MHz and 1.4 GHz.
The spectral maps of the core of IC5338 (Fig. 3.11 and 3.12) highlights an interesting feature of this radio source. The jet-like structures, that we observe in Fig. 3.2, have a steep spectrum -2.0<α<-1.5 between 1.4 and 5.5 GHz, whereas a typical radio lobe have a spectral index of -0.7 (Meisenheimer et al. 1997). This suggests that the jets are the relics of a previous AGN activity of IC5338.
Finally, the spectral maps of the diffuse emission between 1.4, 3.0 and 5.5 GHz (Fig. 3.13 and 3.14) hint the presence of an extended radio source between the arcs and the core, with a spectral index $\alpha \sim -1.5$. Due to the low resolution, we cannot exclude that the emission is correlated with the arcs.

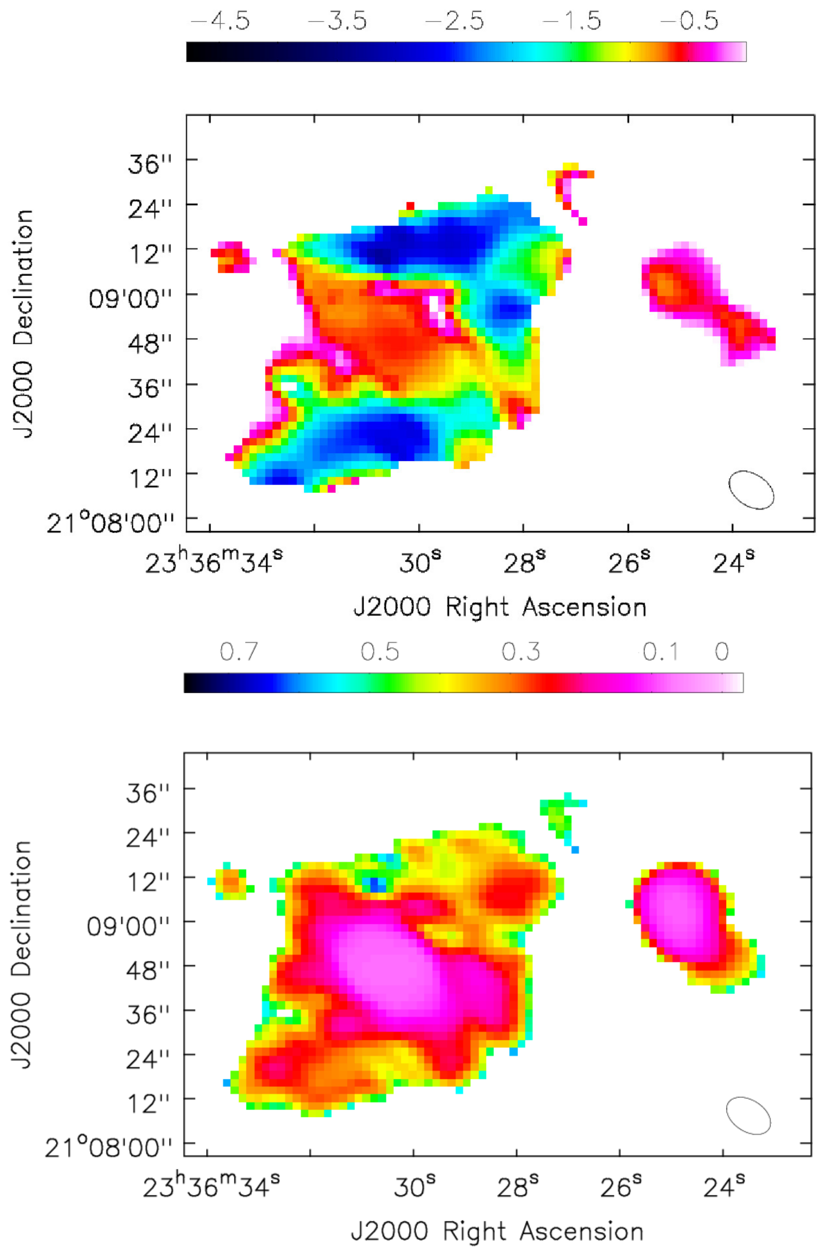

Figure 3.9: *Top:* 1.4-3.0 GHz spectral index map.*Bottom:* Relative error map

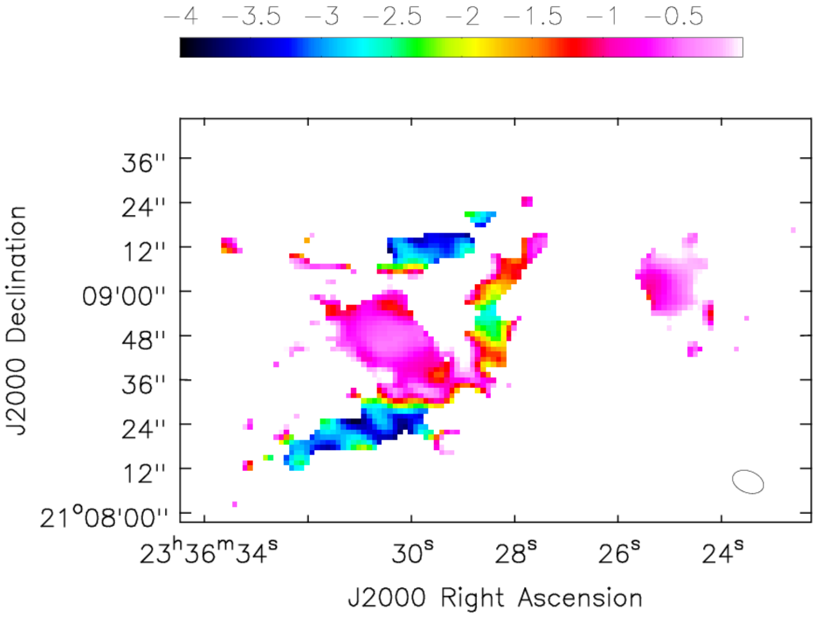

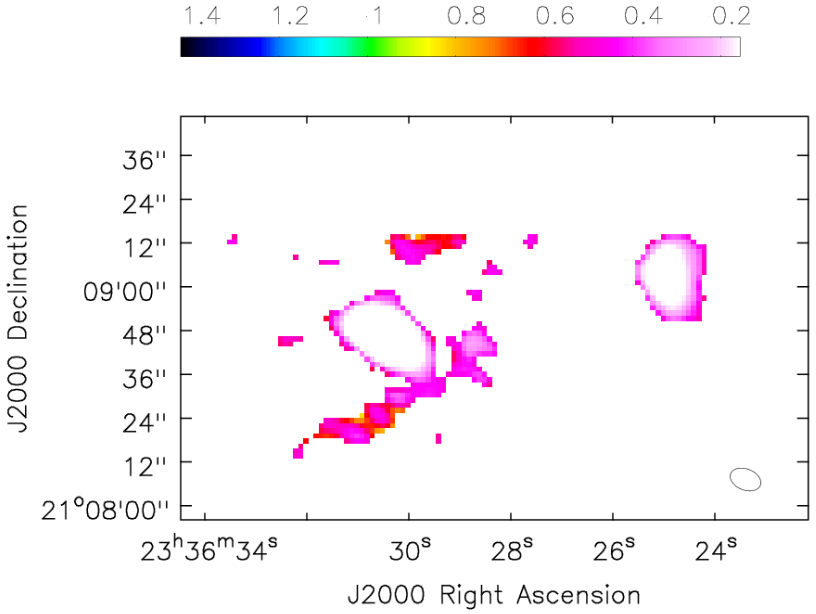

Figure 3.10: *Top:* 1.4-3.0 GHz spectral index map.*Bottom:* Relative error map

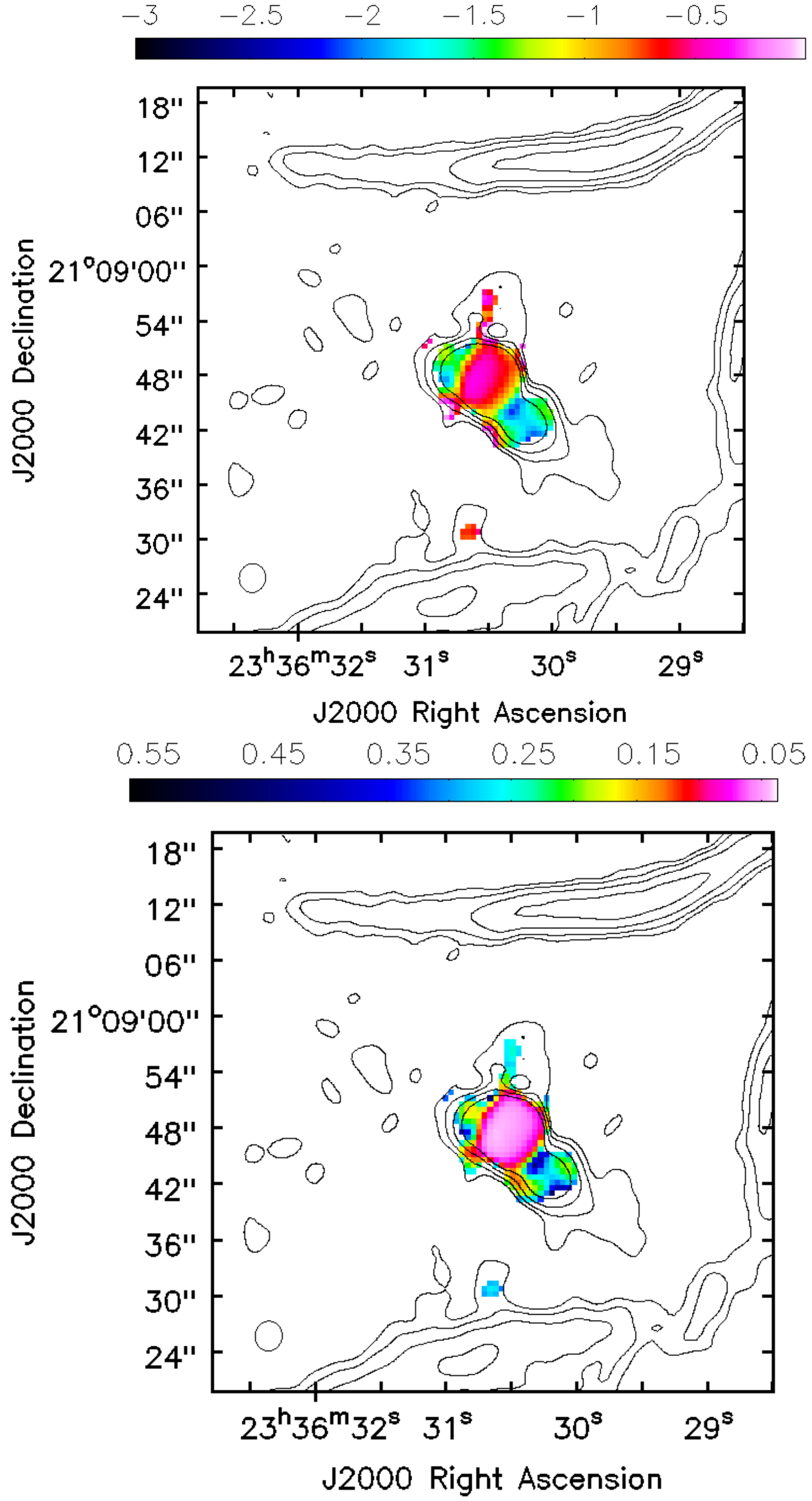

Figure 3.11: *Top:* 1.4-5.5 GHz spectral index map with 1.4 GHz contours.*Bottom:* Relative error map

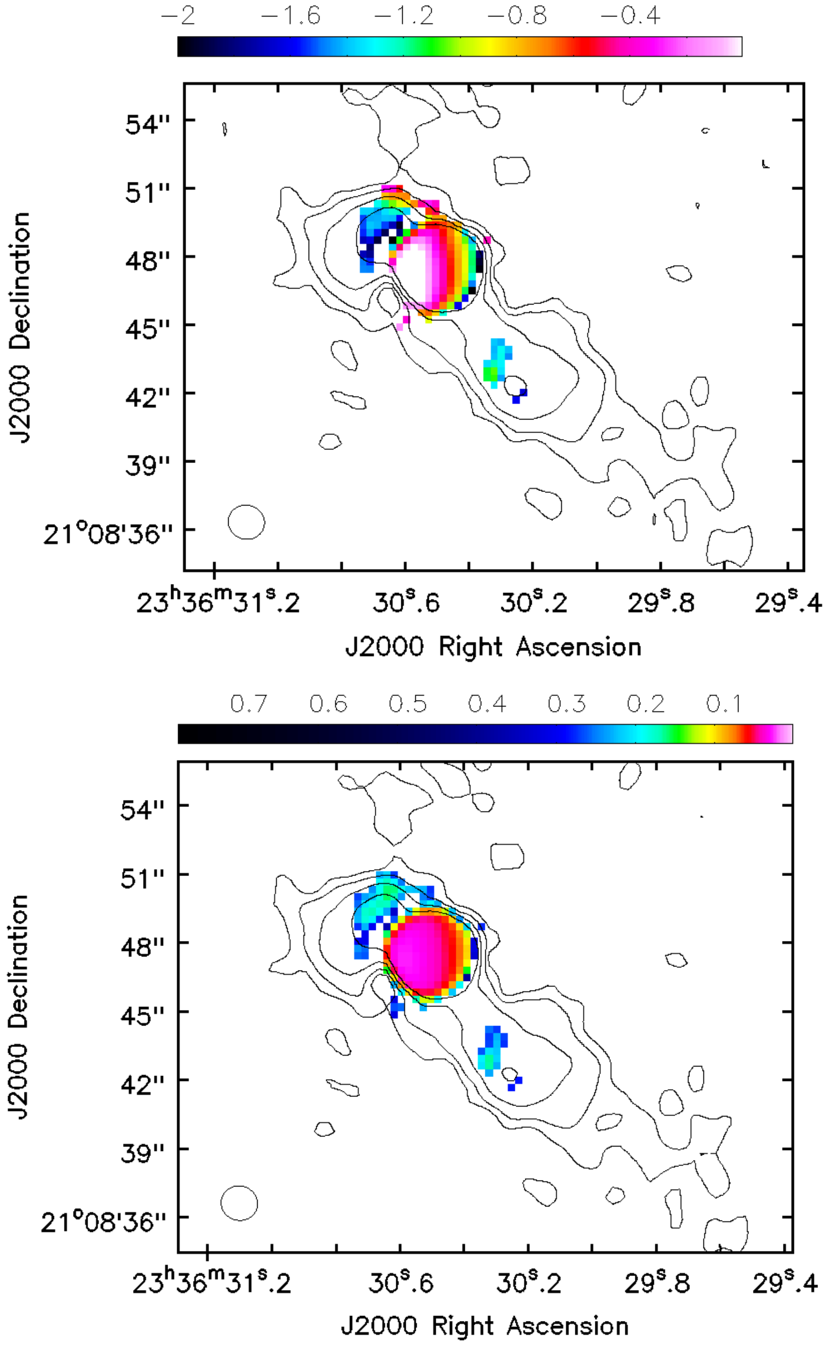

Figure 3.12: *Top:* 1.4-4.8 GHz spectral index map with 1.4 GHz contours.*Bottom:* Relative error map

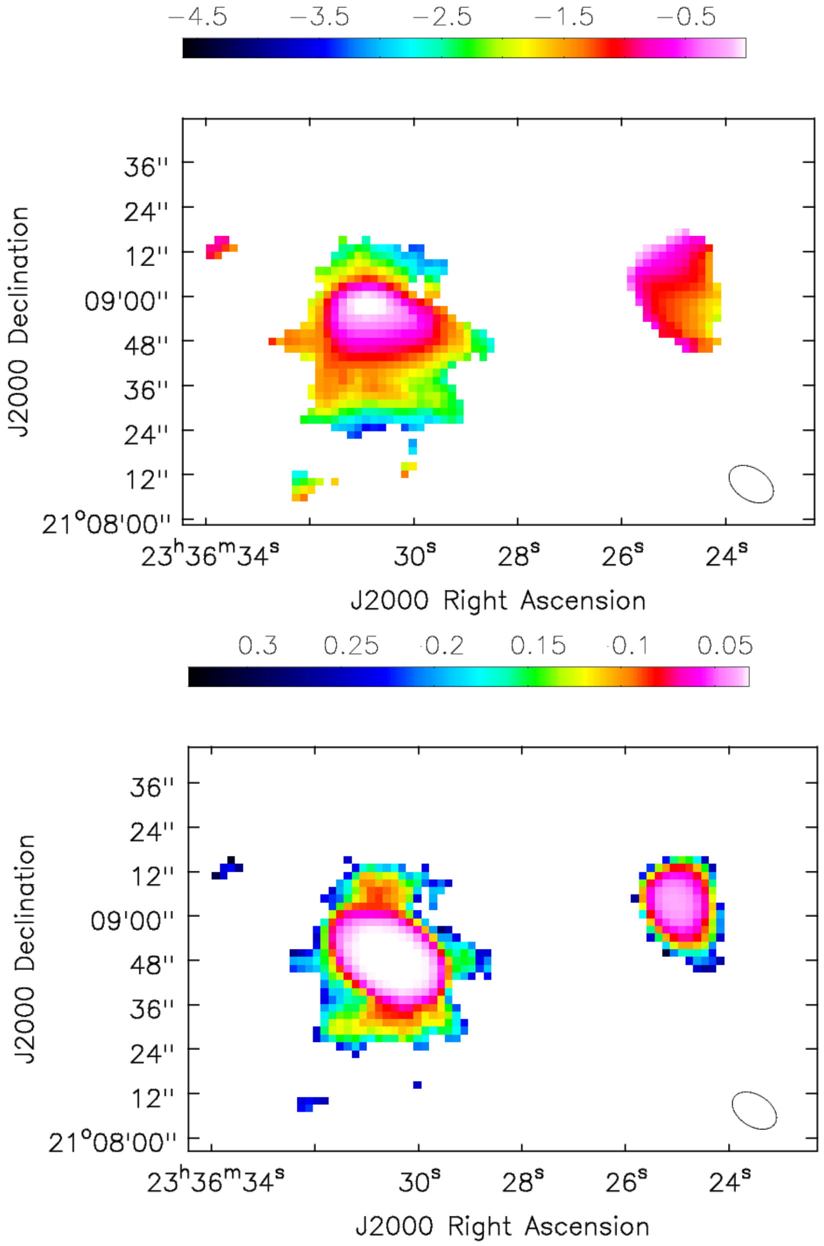

Figure 3.13: *Top:* 1.4-5.5 GHz spectral index map.*Bottom:* Relative error map

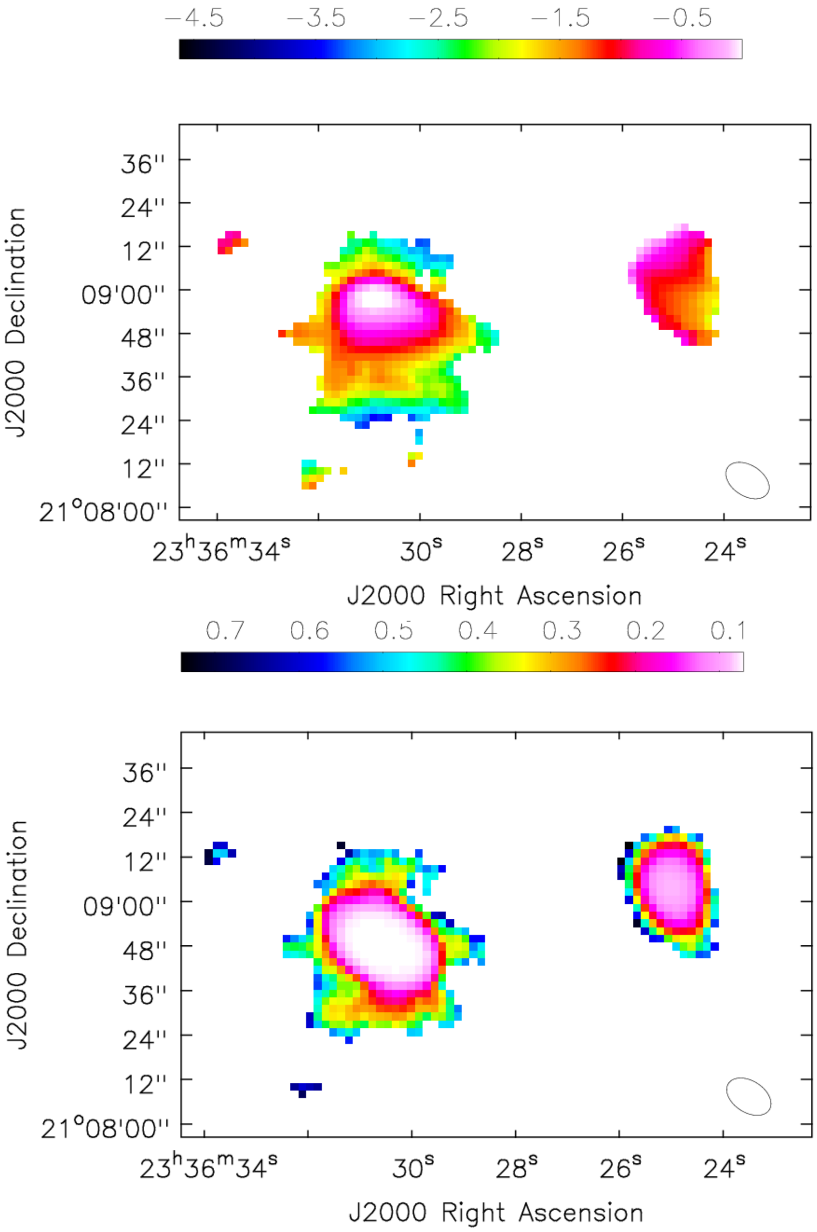

Figure 3.14: *Top:* 3.0-5.5 GHz spectral index map.*Bottom:* Relative error map

3.2.1 Observed flux density-spectral index trends

We estimated the variation of the spectral index and the flux density along the arcs as a first test of jet-precession model. According to this model, we would observe a clear steepening trend of the spectral index, as result of the different radiative age of each chunk of the arcs, where the flattest spot would coincide with the brightest part of each arc, because it would be in the proximity of the freshly reaccelerated hot-spot.

We initially sampled the arcs regularly in elliptical sub-regions, having the same size of the beam (e.g. Fig. 3.15). In each sample bin we measured the flux density and the spectral index, thus obtaining the emission and spectral trends along each arc. This procedure was repeated on both the `NATURAL` and the `ROBUST 0` spectral maps, keeping the same sampling order to make the two trends of each arc consistent with each other. The results are reported in Fig. 3.16-3.18.

The first important result is that the mean spectral index of the western arc is flatter than the mean values of the other arcs. Another interesting feature is the symmetry of the arcs south and north in both the morphology (e.g. Fig 1.6) and the spectral index trends.
The brightest sample of each arcs does not exhibit a clear correlation with the spectral index. Furthermore, the spectral index is almost constant along the arc. These results open to two possible explanations:

- We do non observe a clear spectral index trend because its variation is so weak that it is totally hidden by the errors on the spectral index values. We may assume the upper and lower limits of the tilt of the spectral index of each arc as extremes of the distribution;
- We do not observe a clear spectral index trend because the trend does not exist: each chunk of the arcs was created at the same time, and they are aging at the same time;

The first scenario could be compatible with the jet-precession model, otherwise the latter explanation would be in disagreement with it, because it implies that the particles of the arcs were accelerated simultaneously on the whole structures, and not gradually from an end to the other.

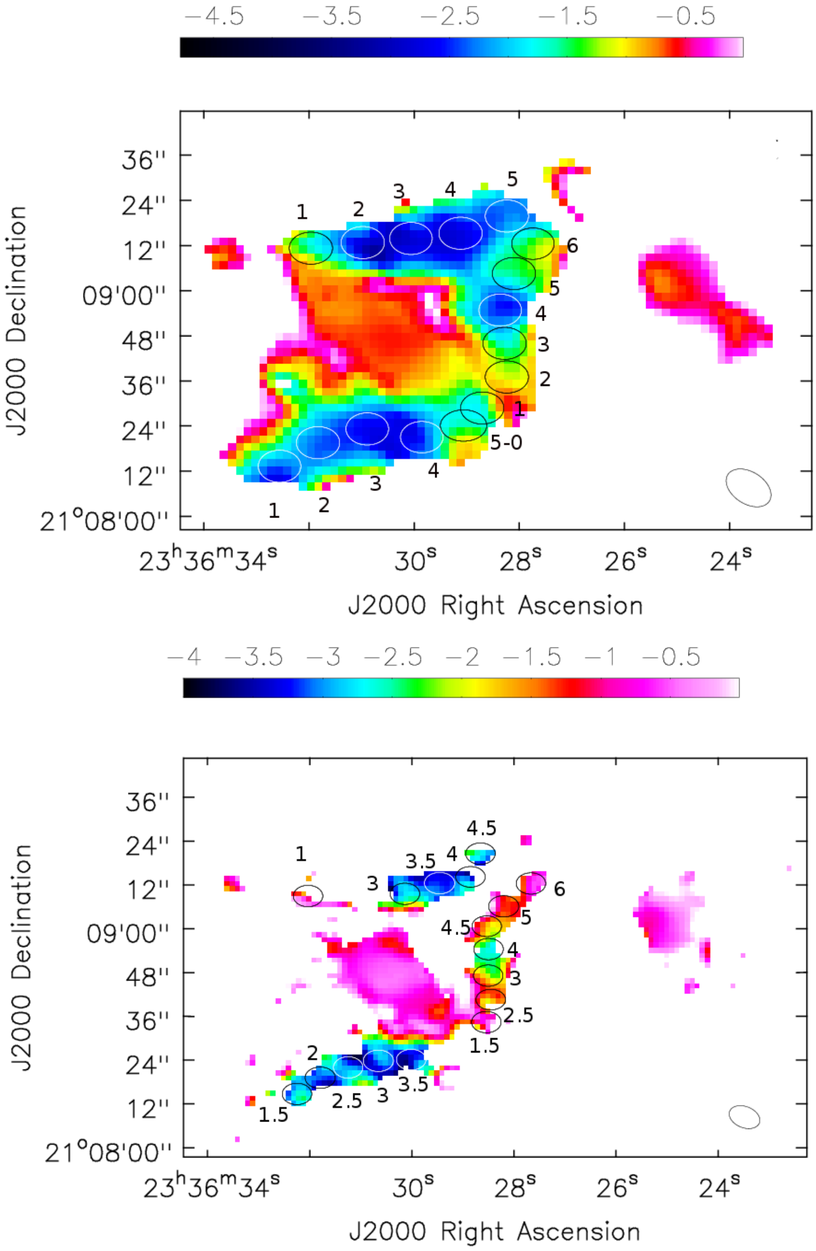

Figure 3.15: Sampling method used to produce the graphics in Fig. 3.16-3.18

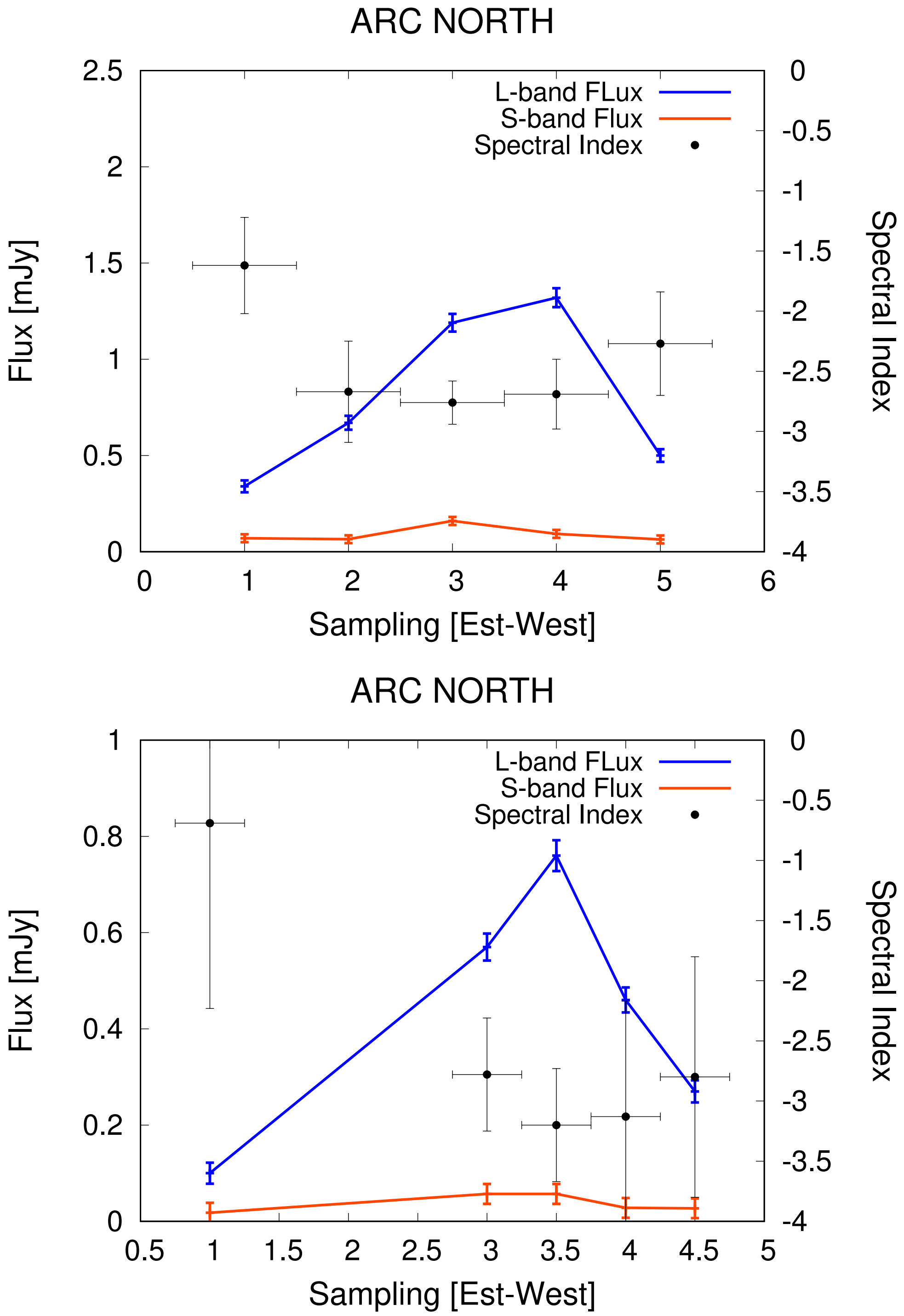

Figure 3.16: Spectral index and flux trend along the arc North. On the x-axis is shown the sampling numeration, on the left y-axis the flux scale and on the right y-axis the spectral index scale. The values are measured on: *Top:* `NATURAL` maps; *Bottom:* `ROBUST 0` maps.

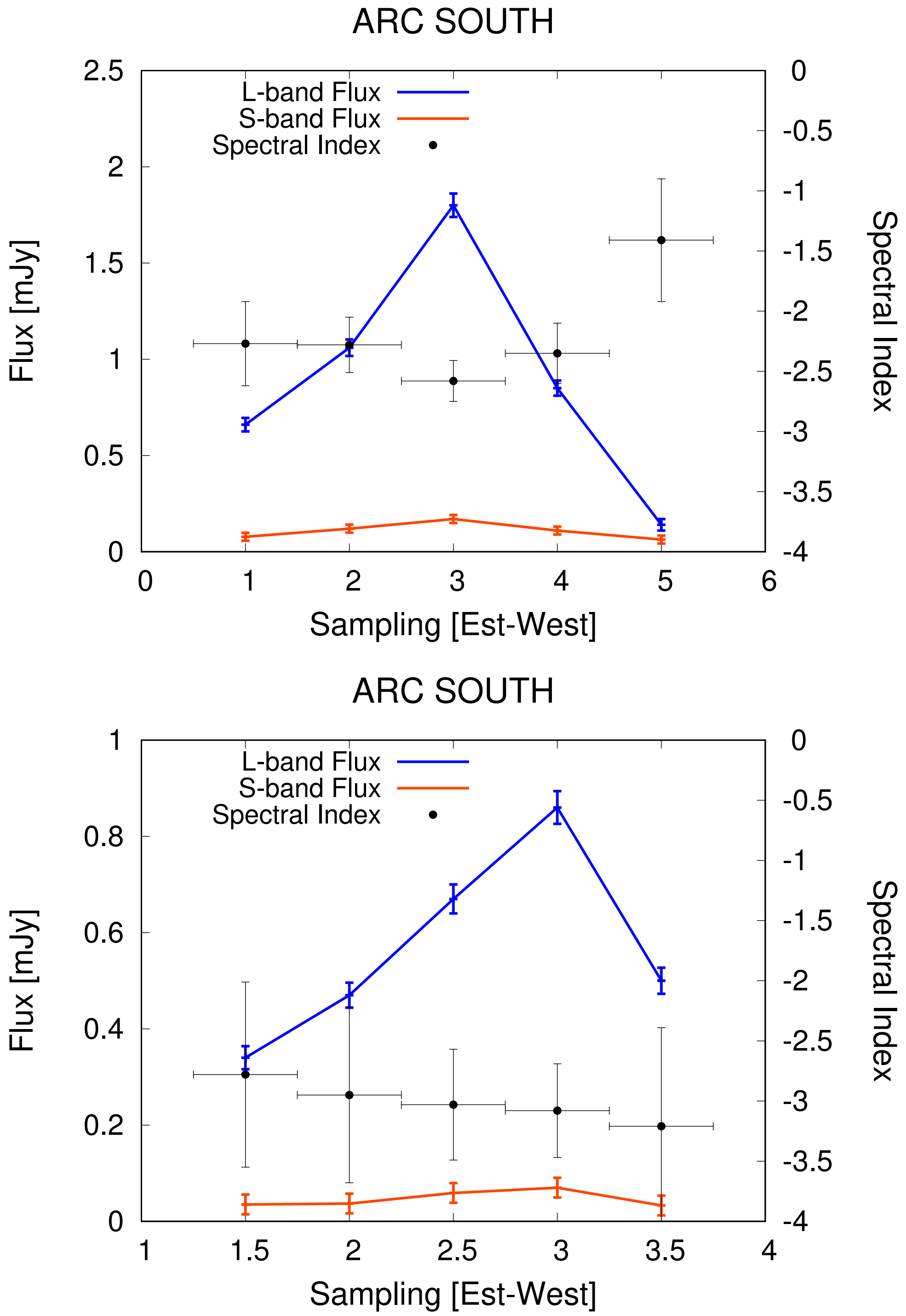

Figure 3.17: Spectral index and flux trend along the arc South. On the x-axis is shown the sampling numeration, on the left y-axis the flux scale and on the right y-axis the spectral index scale. The values are measured on: *Top:* `NATURAL` maps; *Bottom:* `ROBUST 0` maps.

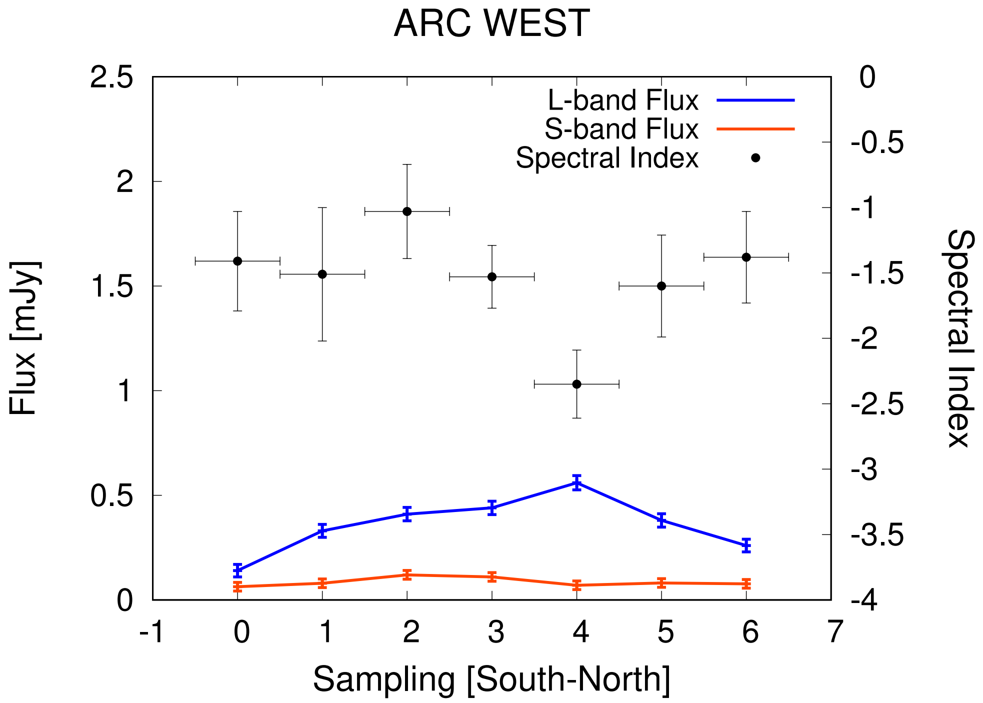

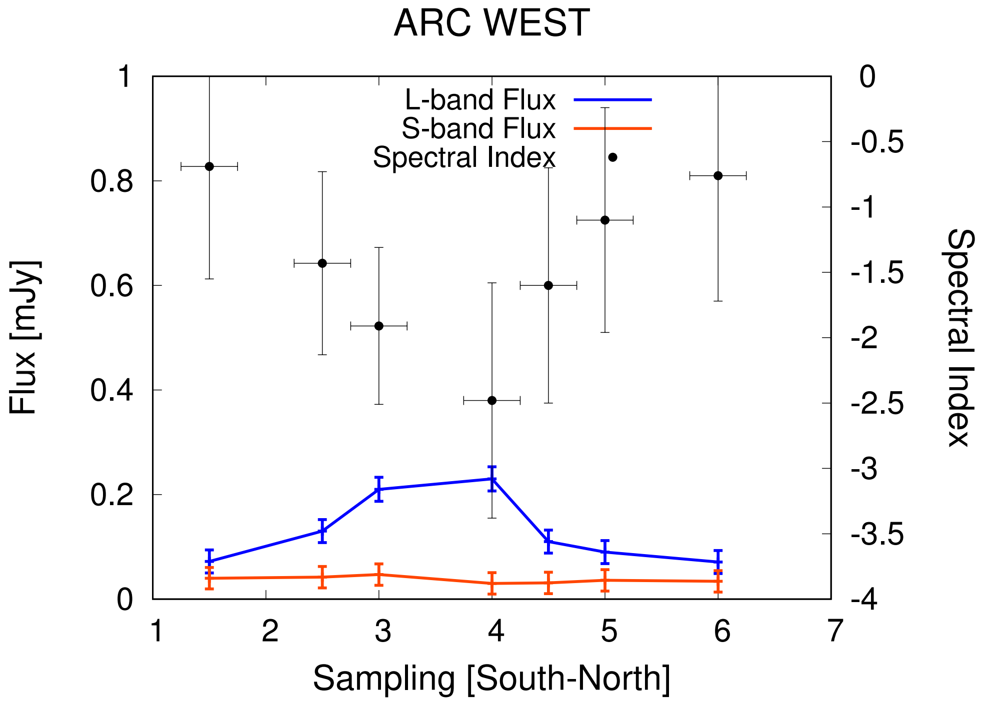

Figure 3.18: Spectral index and flux trend along the arc West. On the x-axis is shown the sampling numeration, on the left y-axis the flux scale and on the right y-axis the spectral index scale. The values are measured on: *Top:* `NATURAL` maps; *Bottom:* `ROBUST 0` maps.

Chapter 4

The thermal side of the cluster: results of the CHANDRA observation

In this chapter we present the results of the analysis of the thermal emission of A2626. The radio analysis did not clarify the origin of the arcs. For this reason we included in this work the analysis of the thermal properties of the cluster. In particular, we searched for possible correlations between the thermal and non-thermal components. Non-thermal processes can leave "traces" on the thermal properties of the ICM. Strong AGN activity by the cD galaxy can displace the thermal plasma, creating a *cavity* visible as a depression in the surface brightness distribution of the cluster (e.g. Gitti et al. 2012). On the other hand, dynamical events, as major or minor merging, can generate shocks which modify the thermal properties of the ICM (Sarazin 1986).
Wong et al. (2008) conducted a study of the X-rays emission of Abell 2626 based on CHANDRA and XMM-Newton observations. They focused on the spectral properties of the sub-clusters, that were identified by Mohr et al. (1996), probing that they are two objects separated from the main cluster. Moreover they measured the mean properties of A2626 and, from XMM-Newton (CHANDRA) data in the 0.6-10.0 (0.5-7.0) keV energy band, they estimated a cooling mass deposition rate of 2 ± 1 (3 ± 3) $M_{\odot}yr^{-1}$ with a mean temperature of 2.8 keV. Their conclusion was that A2626 is a weak cooling-flow cluster. They analyzed also the inner part of the cluster, searching for high-energy counterparts for the optical cores of IC5338 (Fig. 4.1).

They observed that only the southern core exhibits hard X-ray emission. By analyzing the surface brightness (SB) they found evidence of a surplus of the emission, which they call "tongue", that may be related with the southern core. They did not find any direct evidence of correlation between the radio emission and the surface brightness. They concluded that the arcs might be extremely

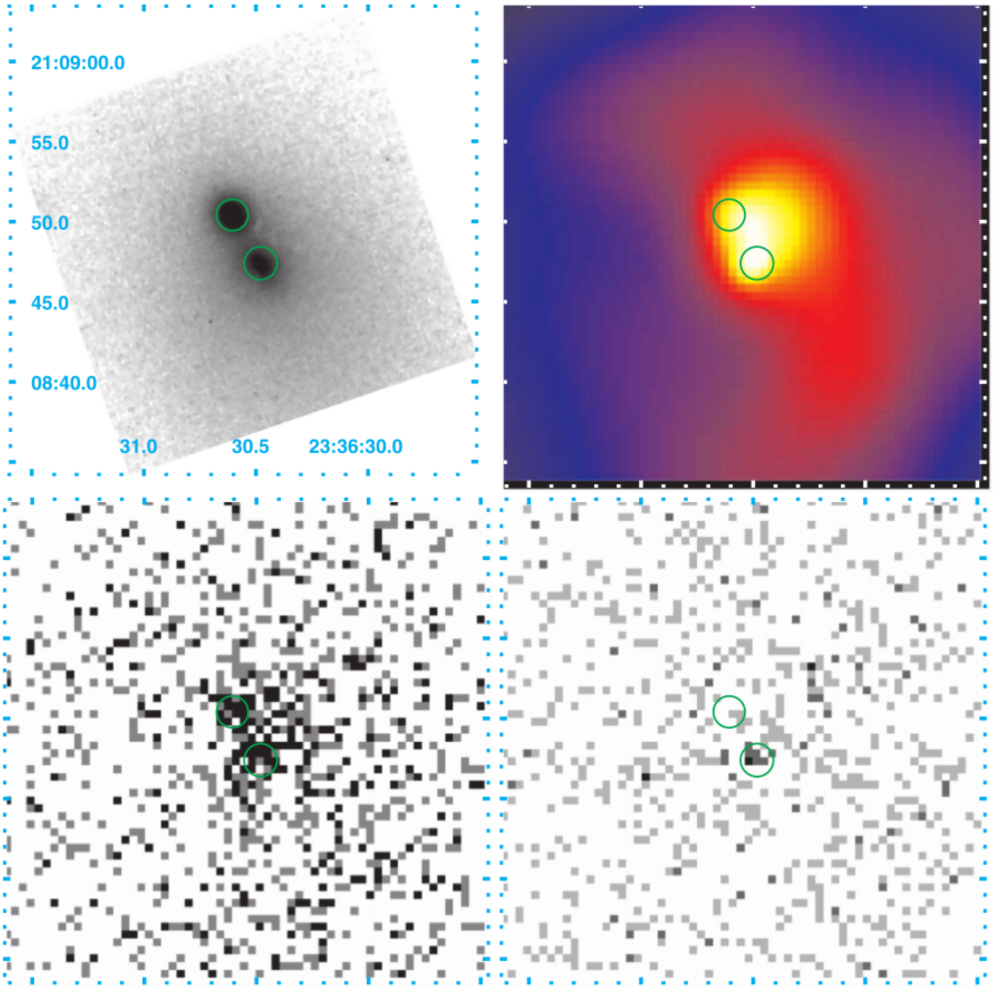

Figure 4.1: Images of the two nuclei of the cD galaxy IC 5338 in Abell 2626. All images show the same FOV of 30"x30". Top left: Optical image from HST archive. The image was taken with WFPC2 using the F555W filter. The two green circles, included in the other panels, are centered at the two optical nuclei observed by HST. Top right: Background-subtracted, exposure-corrected, adaptively smoothed CHANDRA image in the 0.3 -10 keV band. The image was smoothed to a signal-to-noise ratio of 3. The color represents the X-ray intensity from high (white-yellow) to low (dark blue). Bottom left: Raw CHANDRA image in the soft (0.3-2 keV) band. Two intensity peaks can be identified. Bottom right: Raw CHANDRA image in the hard (2 -10 keV) band. Only the southwestern nucleus corresponds to the peak in the hard band (Wong et al. 2008).

collimated, so they do not interact efficiently with the thermal plasma.
In our analysis, after a brief examination of the global properties of the cluster, we focused on the inner region. We combined advanced techniques of 2D analysis of both the spectroscopic and morphological properties, to locate any possible interesting features.

4.1 CHANDRA X-ray Observatory

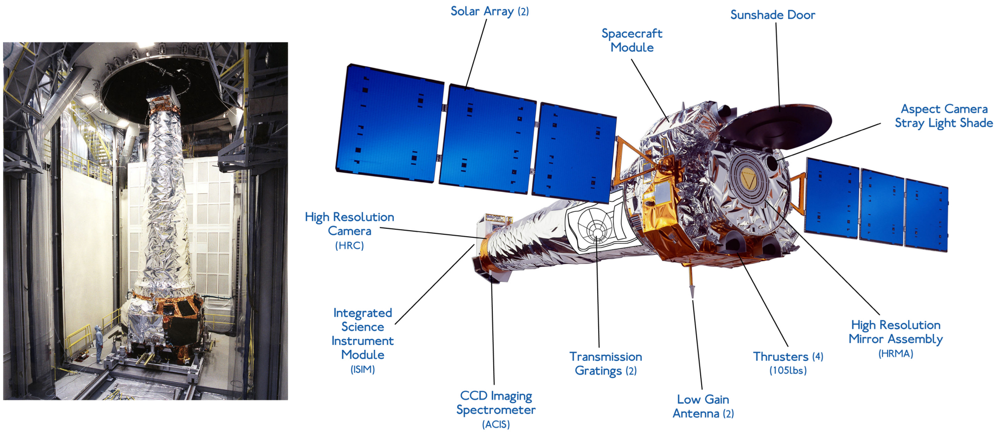

Figure 4.2: Renamed the CHANDRA X-ray Observatory after launch, the image on the left shows AXAF during pre-launch testing. The image on the right shows the instruments onboard the observatory. Credit: NASA

The CHANDRA X-ray Observatory (CXO) (Fig. 4.2) is a Flagship-class space observatory launched on STS-93 by NASA on July 23, 1999. Since the Earth's atmosphere absorbs the vast majority of X-rays, they are not detectable from Earth-based telescopes. For this reason space-based telescopes are required to make these observations. CHANDRA is an Earth satellite in a 64-hour orbit. The telescope is named after astrophysicist Subrahmanyan CHANDRAsekhar.
CHANDRA is characterized by an unrivaled resolution: between 80% and 95% of the incoming X-ray energy is focused into a one-arcsecond circle.

4.2 Data Reduction and Analysis techniques

In this section we present the procedures that were applied to the data. Our analysis progressed through several steps. We started by studying the maps of the thermal properties of the cluster by comparing them with the 2D fit of the

Table 4.1: New CHANDRA data analyzed in this work (PI C. Sarazin)

Observation Date	20-Oct-2013
ObsID	16136
Energy band (keV)	0.5-10
Detector Name	ACIS-5678
On source Time (s)	110848.61

SB and the maps of radio emission. Through these analysis, we identified an interesting feature over the South-West junction of the radio arcs. On that sector we extracted a first set of spectra to estimate the thermal profiles. These profiles hinted to the presence of a front, but with some uncertainties on the position. For this reason we developed also the SB profiles analysis, which gave us the exact position of the jump. Finally we were able to extract the spectral profile over this region to identify the nature of the front.

4.2.1 Data reduction

We developed the analysis on the newest CHANDRA observation of A2626 (details in Tab. 4.1). The data reduction was done with the CHANDRA analysis software CIAO v.4.9, by following the standard procedure[1]:

- Correcting Absolute Astronometry: to compare properly the results of the observation with other maps we need the best possible source position. These informations were acquired from an external catalogue;

- Reprocessing Data to create the LEVEL 2 Event file: the bad data (events) were removed from the initial (LEVEL 1) dataset;

- Setting the Observation-specific Bad Pixel Files: we removed the bad pixel from the events file. Setting the bad pixel file ensures that the most accurately known bad pixel list for any observation will consistently be used in the data processing.

- Filtering Light Curves

- Removing Warm ACIS Data: The ACIS focal plane temperature (FPTEMP) may vary during an observation. This variations can produce fake events in the events file which we removed.

---

[1] http://cxc.harvard.edu/ciao/threads/data.html

4.2.2 Morphological analysis

We studied accurately the SB distribution of A2626. We performed two kind of 2D analysis: the *2D double β model fit* and the *Gaussian filtering* (Sanders et al. 2016). We further extracted the surface brightness profiles in relevant sectors to analyze them with several SB models.
The 2D fit was performed with the software SHERPA v. 4.4 of the CHANDRA data analysis package CIAO. The software fits the brightness value of every pixel of a map with a model, that may be semi-analytical, as the double β model (Eq. 1.4) that we used, or mathematical, like a 2D gaussian. It provides the best fit parameters and the residual map, obtained by subtracting the model from the image. This is a very useful result, because it highlights the regions whose emission differs from the model, pointing out every over-densities, or sub-densities, in surface brightness. This technique is an alternative to the *unsharp mask*, a process for amplifying fine details in a registered image. This process consists of subtracting two images, which have been smoothed with different gaussians, to highlight any possible feaure of the SB. The Gaussian Filter analysis was proposed by Sanders et al. (2016). The filter calculates the gradient of the image assuming Gaussian derivatives. The gradient of the image is computed along the two axes by convolving the image by the gradient of a 1D Gaussian function. These two gradient images are combined to create a total gradient image. In input it requires the unsmoothed exposure-corrected background-subtracted image and a scale σ , in unit of map resolution. The filter highlights every SB discontinuity whose dimensions are comparable with the σ. This method should be more sensitive to shocks than other kind of analysis. Moreover it is possible to combine different scales to create a map where the scale sensitivity increases with the radius.
The fit of the SB radial profile is similar to the spectral profiles fit. We divided the cluster in several sectors, then we measured the SB of each of them. The SB profile analysis requires:

- Source map: map of the source obtained from the dataset;

- Background map: map of the estimated background emission, it is produced from a blank sky template, which was normalized for the exposure time of our observation;

- Exposure map: map of the CHANDRA imaging effective exposure in units of cm^{2}s. It is made by dithering an instrument map across the sky using the aspect solution (binned into an aspect histogram by the tool `asphist`).

The corrected SB Σ_N is defined as:

$$\Sigma_N = \frac{\Sigma_S - \Sigma_B}{\Sigma_E} \pm \sqrt{\frac{\Sigma_E^2(\sigma_S^2 - \sigma_B^2) + (\Sigma_S - \Sigma_B)^2\sigma_E^2}{\Sigma_E^4}} \tag{4.1}$$

where Σ_S,Σ_B and Σ_E are the values of SB measured, respectively, on source, background and exposure maps, and σ_S, σ_B and σ_E are the relative errors estimated with the poisson statistic.
The SB profiles were fitted with the *double β-model* or the *broken power-law model*. The broken power-law model consists of a power-law:

$$S(r) = Ar^{\delta} \tag{4.2}$$

where A and δ can change value at $r = r_c$, which is the position of a discontinuity in the SB profile. The fit was performed with the code `FRONT` developed by Dr. Nulsen (Nulsen et al. 2005). This code is able to estimate the position of the jump and the density difference across the discontinuity.

4.2.3 Spectral analysis

The spectrum of the thermal emission of a cluster contains many information regarding the thermal properties of the plasma. By fitting the spectrum with an appropriate model of emission, it is possible to estimate temperature, density and pressure of the ICM. The analysis of the spectral properties of the ICM of A2626 was developed through the spectral maps provided by our collaborator Dr. O'Sullivan, and the fitting of the spectral profiles.
The spectral maps were created by using the techniques described in O'Sullivan et al. (2011). Each pixel on the maps represents the best-fitting values obtained from absorbed APEC model fits to spectra with 1500 net counts. Since the spectral extraction regions are typically larger than the map pixels, individual pixel values are not independent and, therefore, the maps are analogous to adaptively smoothed images, with more smoothing in regions of lower surface brightness. Due to above assumptions, the values of the these maps are approximate, and they should be supported with the spectral profiles. Nevertheless they can hint to the presence of substructures, that may be not detected in a surface brightness map.
On the other hand, the fit of spectral profiles is a useful tools that allows us to estimate the variation of thermal properties of the ICM. In order to obtain the profiles, the cluster region was divided in many annular subregions, then the spectrum of each sector was analyzed by fitting the observations with a proper model of emission. We used the software XSPEC v. 12.9.1 (Arnaud 1996)

to develop this analysis. We fitted the data with two models, the projected `WABS·APEC` and the de-projected `PROJCT·WABS·APEC`. The `WABS` model (Morrison and McCammon 1983) parametrizes the photo-electric absorption using Wisconsin cross-sections. On the other hand, `APEC` recreates an emission spectrum from collisionally-ionized diffuse gas calculated from the AtomDB [2] database. The combination `WABS·APEC` is a solid modelization of the thermal emission of the ICM. The de-projected model include also a de-projection component `PROJCT`. This model performs a 3D to 2D projection of prolate ellipsoidal shells onto elliptical annuli.

These models allow to estimate the normalization parameter N, the temperature T and the metallicity Z of the emitting plasma. Given the definition of N in APEC, it is possible to compute the electron density n_e as:

$$n_e(r) = \sqrt{10^{14}\left(\frac{4\pi \cdot N(r)[D_A(1+z)^2]}{0.82V(r)}\right)} \tag{4.3}$$

where $V(r)$ is the volume of the region at radius r (we assumed the spherical symmetry) and D_A is the *angular distance* of the source. The pressure P may be written as:

$$P(r) = 1.83\ n_e(r)kT(r) \tag{4.4}$$

From the temperature and density profiles it is possible to estimate the *cooling time profile* (Eq. 1.9).

We built a package of codes that automate the extraction of spectral profiles (e.g. Fig. 4.3). These scripts require the events file of the observation, several information about the target of the observation (as redshift, luminosity distance, galactic hydrogen column density), and a region, which can be composed of circular annulus or circular sectors. With these inputs, the codes extract the spectrum of each sector, and give the user the options to perform the projected or de-projected fit. After the fit, the scripts collect the results of every sector, with the associated error on each value, and the statistical information of every fit. Every value has a 90% confidence with a $\Delta\chi^2$=2.7 what correspond to 1.65 σ. The final step is to compute density, pressure and cooling time and produce a simple plot of the radial profile of each quantity. The projected fit is totally automated, while the de-projected fit, due the complexity of the operation, requires the monitoring of the user. This package reduced heavly the time required to complete the spectral analysis.

---

[2] http://atomdb.org/

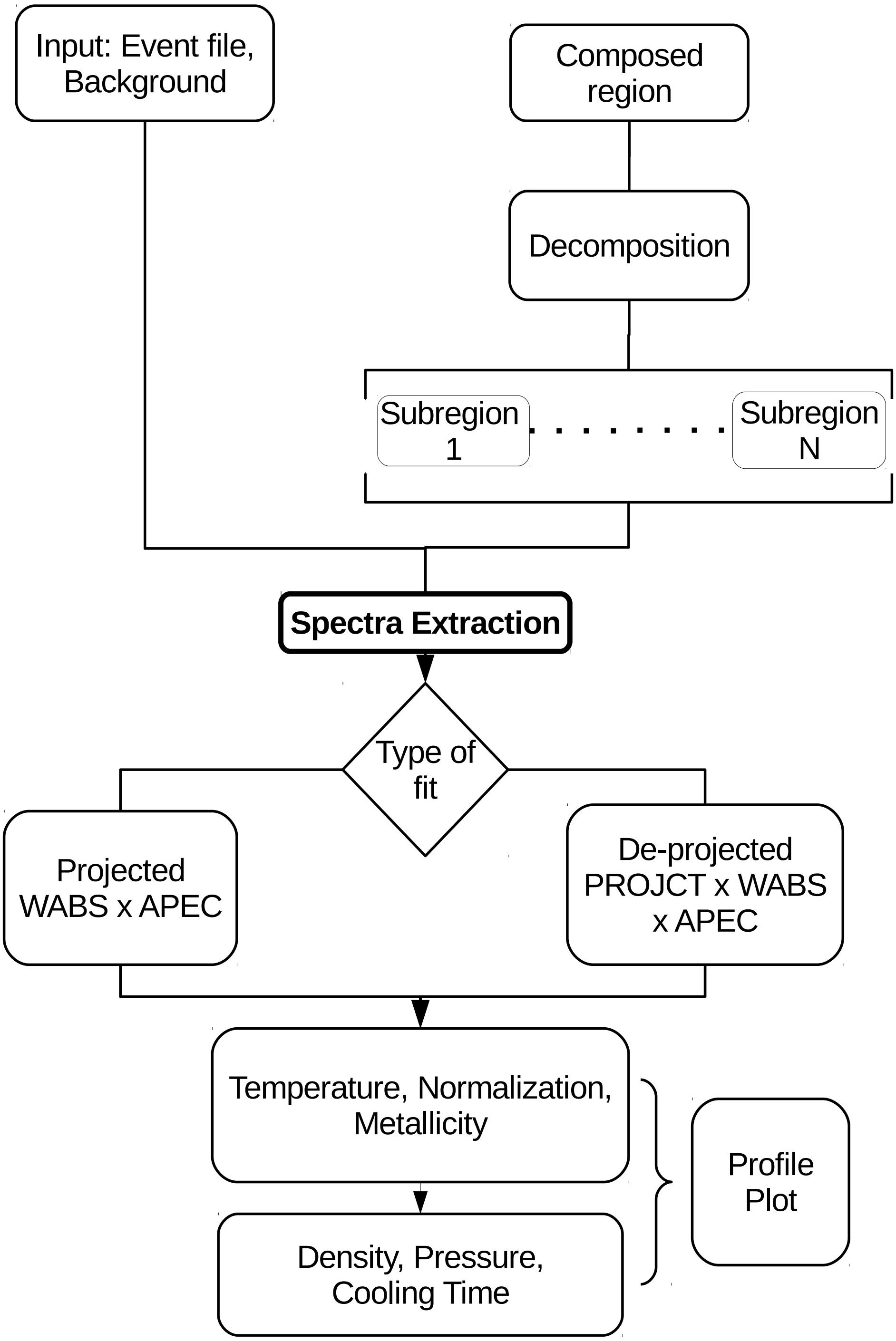

Figure 4.3: Flow chart of the code developed to perform the spectral analysis.

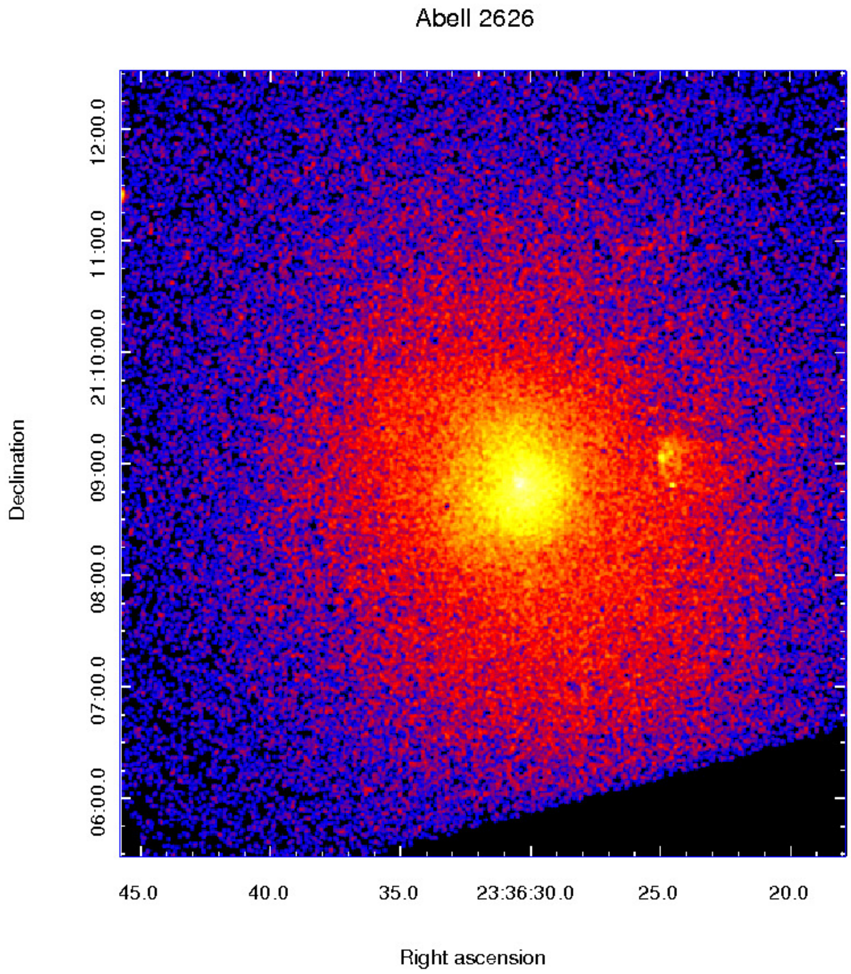

Figure 4.4: 0.5-2 keV smoothed raw image of A2626 made from the CHANDRA dataset.

4.3 Analysis of the Cluster

After the data reduction process we produced the raw image of the X-ray emission of the cluster in the 0.5-2 keV energy band (Fig. 4.4). A2626 appears as a relaxed cluster, with a roundish shape that is disturbed only by the motion of IC5337. This galaxy shows its own emission (e.g. Fig. 4.5), whose shape resembles its radio emission (e.g. Fig 3.2-3.3).

We detected three point sources: the cores of IC5338 and IC5337 and one in the south tail of IC5337.
We analyzed the spectral profiles of the cluster, that we evaluated by sampling

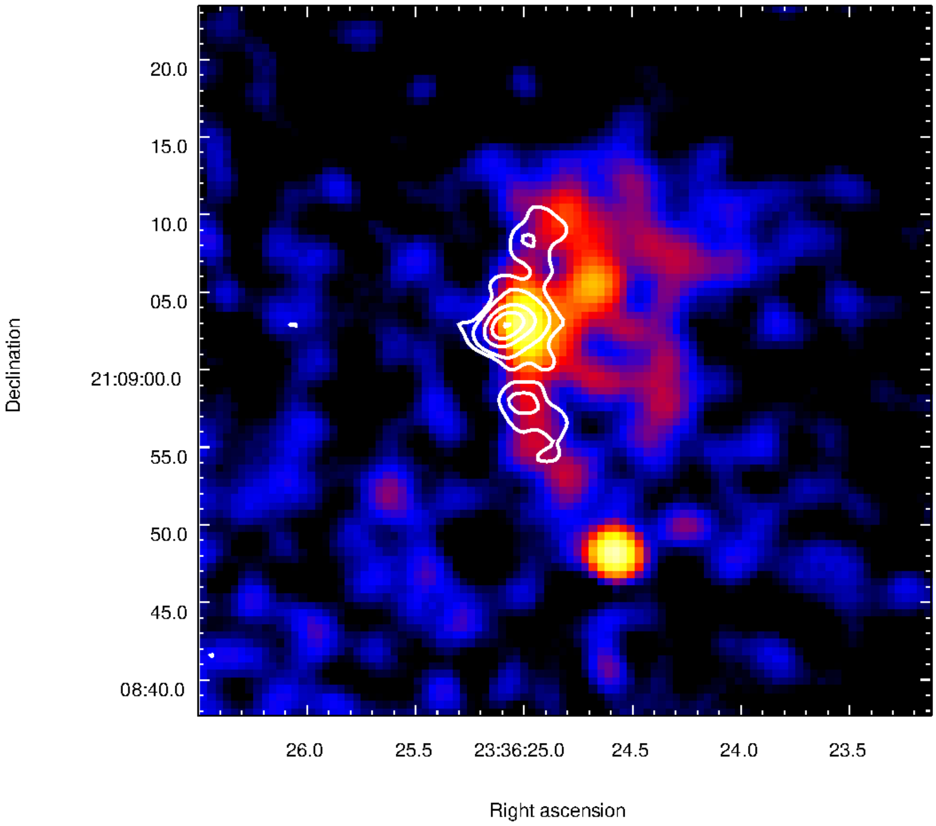

Figure 4.5: X-ray emission of IC5337 in the 0.5-2 keV energy band. In white are overlaid the contours of its radio emission at 1.4 GHz (Gitti 2013).

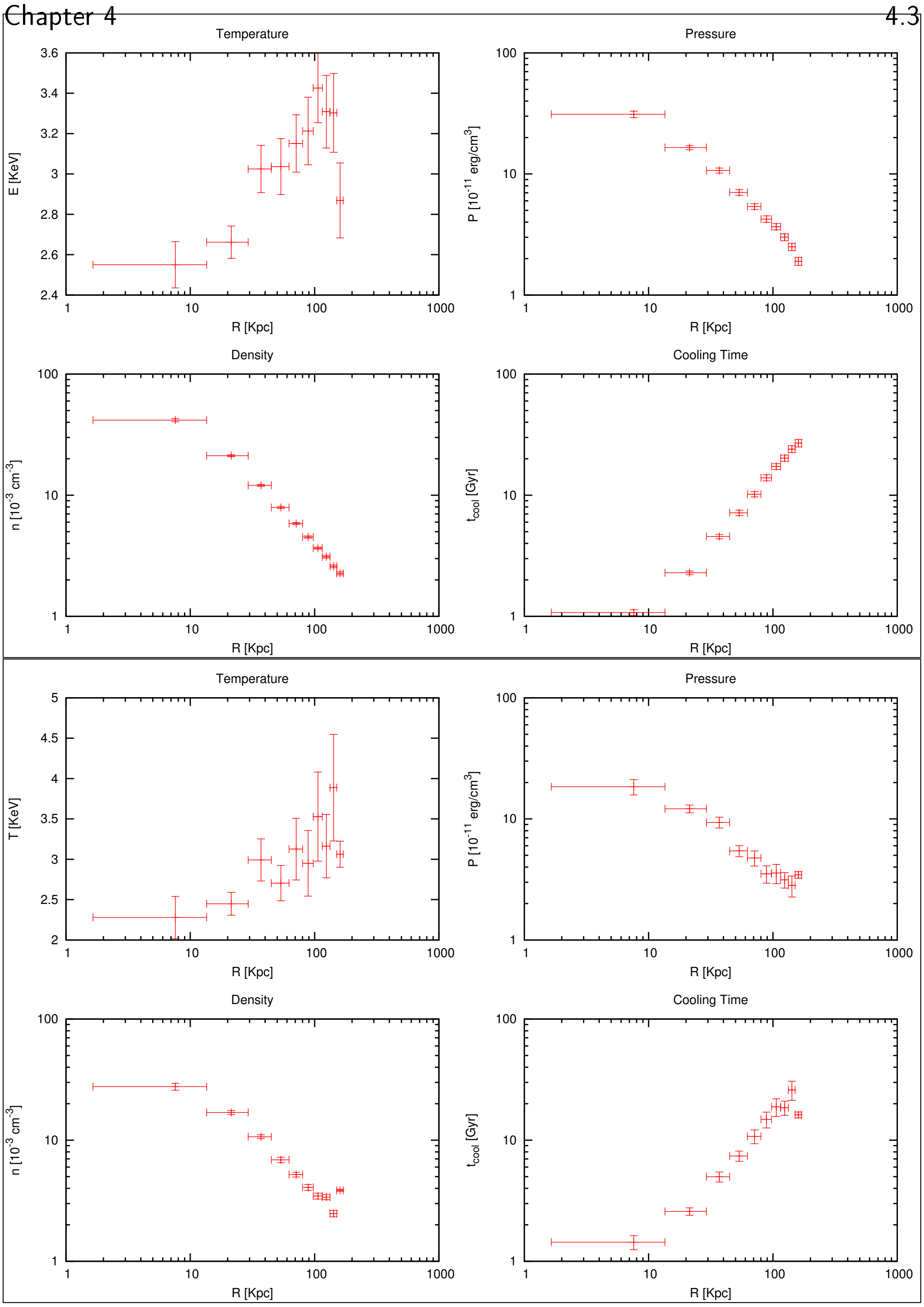

Figure 4.6: The azimuthally-averaged radial profiles inside 170 kpc *Top:* projected azimuthally-averaged radial profiles *Bottom:* de-projected azimuthally-averaged radial profiles.

the ICM thermal emission with ten circular annuli, thus obtaining azimuthally-averaged radial profiles. During the sampling we removed every source that was not related to the cluster thermal emission, as the point-like sources and the diffuse tail of IC5337. The radial profiles (Fig. 4.6) reveal that the temperature decreases slightly towards the center, indicating that the cluster is a cool-core. The cooling radius, R_3, is the radius for which the cooling time is 3 Gyr. For A2626 we estimated a cooling radius R_3=23.2 kpc. This value is in agreement with that found by Bravi et al. (2016), who developed a similar analysis of the cluster based on another observation.

We then extracted the spectrum of the whole cluster inside R_3 (Fig. 4.7),

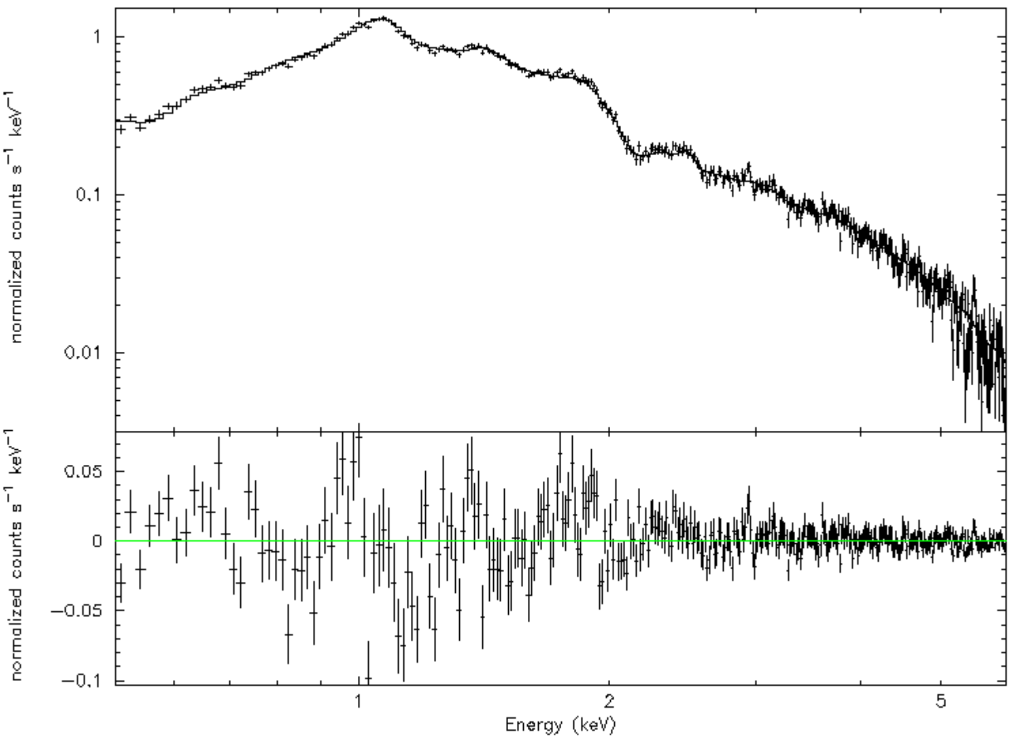

Figure 4.7: Spectrum of the emission of A2626 inside R_3 in the energy range 0.5-7 keV and residual of the fit with the WABS·(APEC+MKCFLOW). The best fit has χ^2_r=1.2. We removed the point sources in IC5338 and IC5337.

to estimate its cooling luminosity and the mass accretion rate. We fitted the spectrum with the WABS·(WABS+MKCFLOW) model, where MKCFLOW model takes into account a isobaric multi-phase cooling flow component. In order to consider the standard cooling flow model, the higher temperature component (kT_{high}) of the MKCFLOW model was tied to the thermal model, under the assumptions that the thermal component represents the ambient cluster gas and that cooling flow

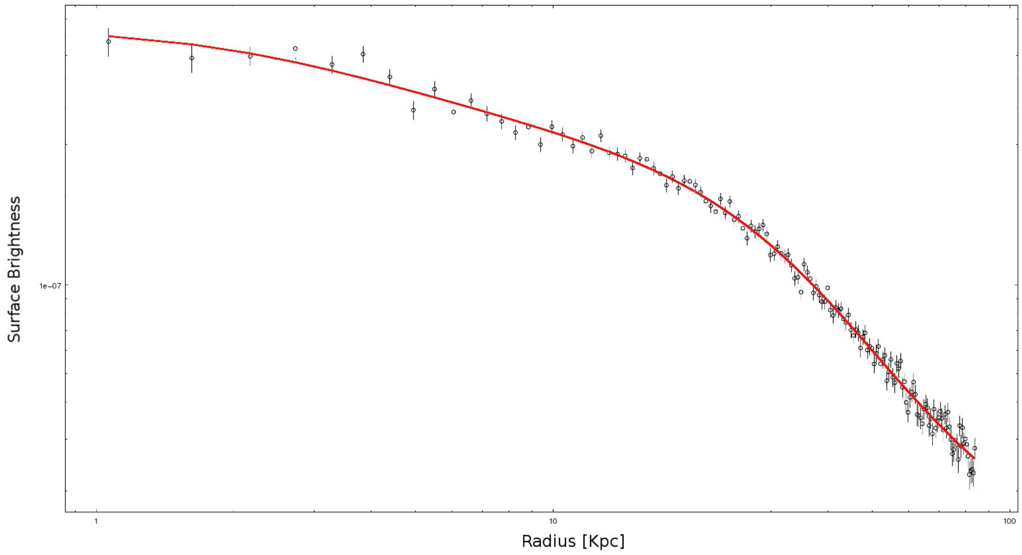

	Radius [kpc]	β	Amplitude $[10^{-7}]$
Component 1	$48.18^{+12.02}_{-8.20}$	$1.14^{+0.42}_{-0.24}$	$2.13^{+0.20}_{-0.19}$
Component 2	$2.28^{+0.57}_{-0.52}$	$0.31^{+0.01}_{-0.01}$	$5.3^{+0.50}_{-0.60}$

Figure 4.8: Azimuthally-averaged SB profile in arbitrary unit of the cluster, extracted from circular annulus inside ~100 kpc. We report in red the result of the double β-model fit. In the table are reported the best-fit parameters.

gas is cooled ambient gas. The lower temperature component (kT_{low}) was fixed close to zero, namely at 0.0808 keV.
We observed that A2626 is a weak cool core cluster, with a cooling flow of 2.5±0.8 $M_{\odot}$/year and a cooling luminosity of $4.2 \cdot 10^{43}$ erg/s in the 0.5-7 keV energy band. The mean temperature is 3.15±0.07 keV. These results are in agreement with the previous results of Wong et al. (2008) and Bravi et al. (2016). On the other hand, the SB of the cluster (e.g. Fig. 4.8) appears to be well fitted by a double β-model.

4.3.1 Spectral maps analysis

We examined the temperature and pressure maps of the cluster, courtesy of Dr. O'Sullivan (Fig. 4.9 and 4.10), with the aim of identifying a possible correlation between the radio arcs and the ICM.

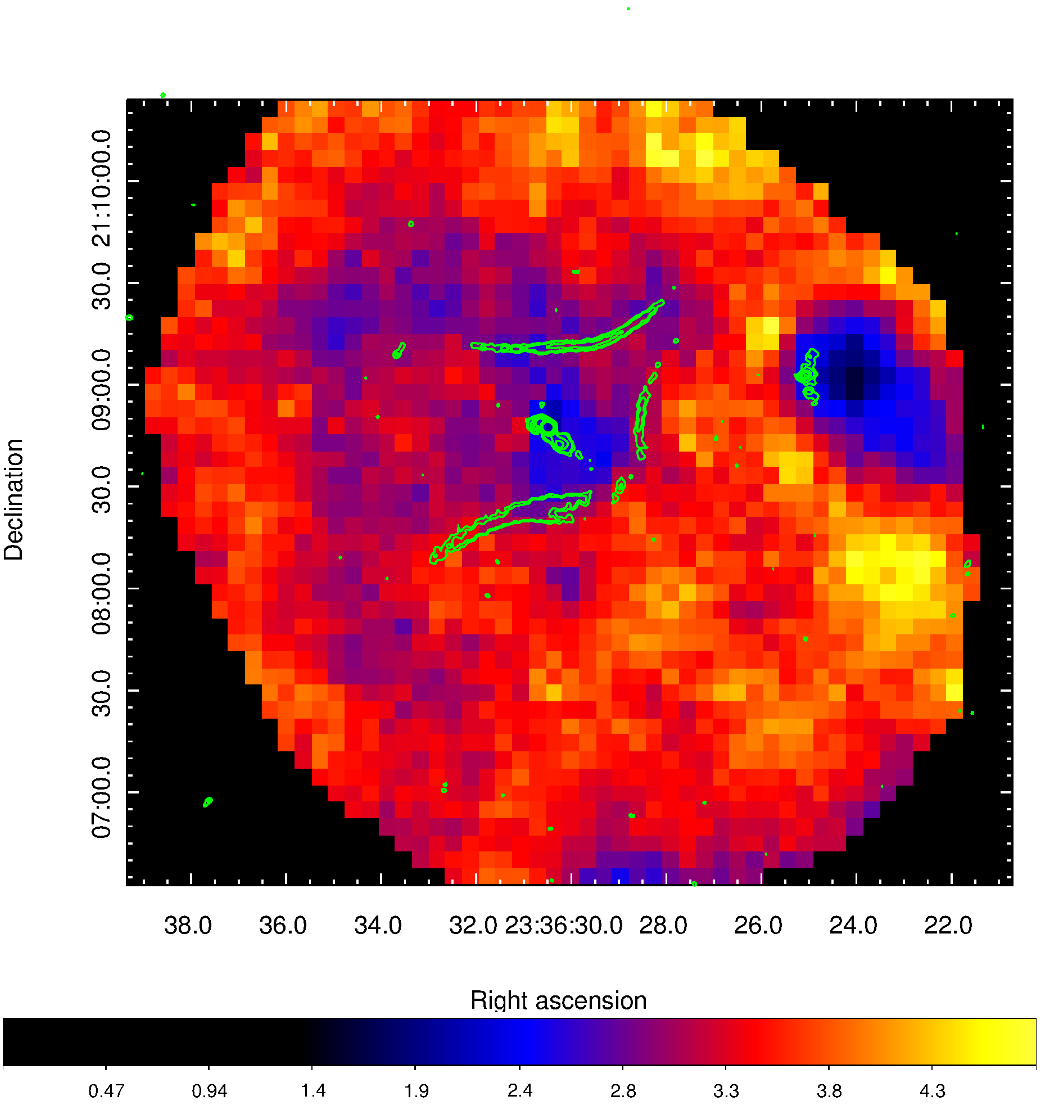

Figure 4.9: Temperature maps of A2626, courtesy of Dr. O'Sullivan. In green are overlaid the contours of the 1.4 GHz map of radio emission from Gitti (2013). The values have a relative error of $\sim 10\%$

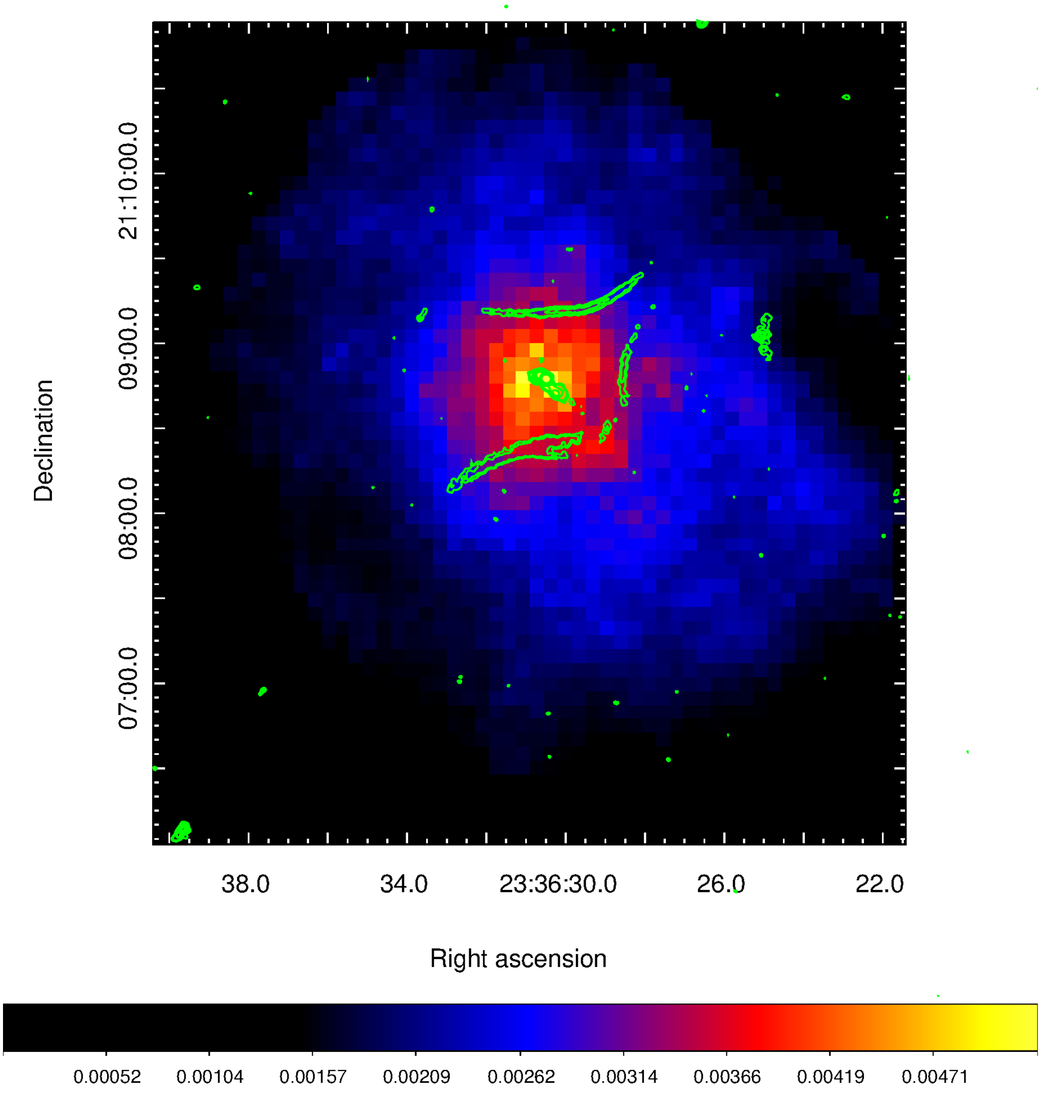

Figure 4.10: Pressure maps of A2626, courtesy of Dr. O'Sullivan. In green are overlaid the contours of the 1.4 GHz map of radio emission from Gitti (2013). The values have a relative error of $\sim 10\%$

The temperature map (Fig. 4.9) shows an interesting correlation between the non-thermal and the thermal components. The radio arcs, in particular the junction between the arc south and west, appear to divide the inner cold region from the outer hot plasma. Furthermore, the cold region does not appear to be totally enclosed by the arcs, but it is elongated outward in a spiral-like shape. On the other hand, the pressure map (Fig. 4.10) highlights the interactions between the ICM and IC5337, which is moving through the plasma leaving a trail of cold plasma (e.g. Fig. 4.9).

4.3.2 Morphological analysis

We further performed a 2D morphological analysis of the cluster emission by fitting the SB of the whole cluster with a double β-model. If the process that originated the arcs interacted also with the ICM, then the plasma may "remember" that event by exhibiting an anomalous distribution of the SB. We carried out this analysis on a circular region centered on IC5337, where we removed the emission of IC5337 and the core of IC5338. We report the residual map and the best-fit parameters in Fig. 4.11.

The residual map (Fig. 4.11) hints at the presence of a cavity in the emission to the east, and an excess to the west. A similar analysis was conducted by Shin et al. (2016), and they argued that the eastern cavity may be related to AGN activities. We are cautious about claiming the detection of a cavity, as it may be an artifact produced by the algorithm. If the cluster hosts a real emission excess to the west, then the fit process may compute a mean value of brightness, in inner region, which is higher than the real value. For this reason it may have overestimated the real emission, finding a cavity at east. It is interesting to notice that, again, the S-W junction of the radio arcs delimits the emission excess.

After the 2D fit we developed the Gaussian Filter analysis. We applied this method (Fig. 4.12), varying the scale from 1 to 8 σ, and we produced also a multiple-scale map. The Gaussian filter highlights an excess located at South-West, which is composed by multiple "fronts". The 1σ map does not detect any kind of structure on the smallest scale. The 4σ map shows at least two clear discontinuities in the SB, and the same result can be observed in the multi-scale map. Finally, in the 8σ map, all the fronts are merged together and they are detected as a single emission bump. It was reassuring to notice that the excess coincides with the positive residual of Fig. 4.11. On the other hand, the filter does not detect the eastern cavity, supporting our interpretation that it may be an artifact given by the asymmetrical surface brightness distribution around the core. The temperature jump (Fig. 4.9) and the SB excess (Fig. 4.11 and 4.12) suggest the presence of possible edges in the ICM. In section 4.4 we present the analysis that was carried out to confirm this possibility.

4.4 Analysis of the South-West Junction

The temperature map of the cluster (Fig. 4.9) indicates that there is a clear separation between the cold (T ~2.4 keV) and the hot (T ~3.4 keV) plasma of the ICM, and the South-West (S-W) junction of radio arcs appears to delimit these regions. We focused our analysis on the S-W junction to investigate this peculiarity.
The spectral analysis was carried out on a specific sector across the S-W junction. This sector (Fig. 4.13) was further divided in seven, eight and nine circular annuli. This sampling method was adopted because we did not know the position of the front *a-priori*. Due to the method that is used to compute them, the spectral maps have a low resolution, so we could not use them to locate reliably the position of the front.
The profiles in Fig. 4.14-4.16 show clearly how the location of the annuli influences the radial profiles. Only the profiles in Fig. 4.15 show a discontinuity in temperature and density, whereas in the other configurations this jump is undetected. The sampling system allowed us to locate the front between 20 and 40 kpc from the core.

In order to know more accurately the position of the jump, we would need to improve the spatial resolution of the spectral profiles. Unfortunately it was not possible due to the low statistics. Each spectra requires a certain number of photons to provide reliable results, so we could not reduce further the dimensions of each sector.
We resolved this issue with the analysis of the surface brightness profiles, that allowed us to tighten the radial sampling of the region to improve the spatial resolution.

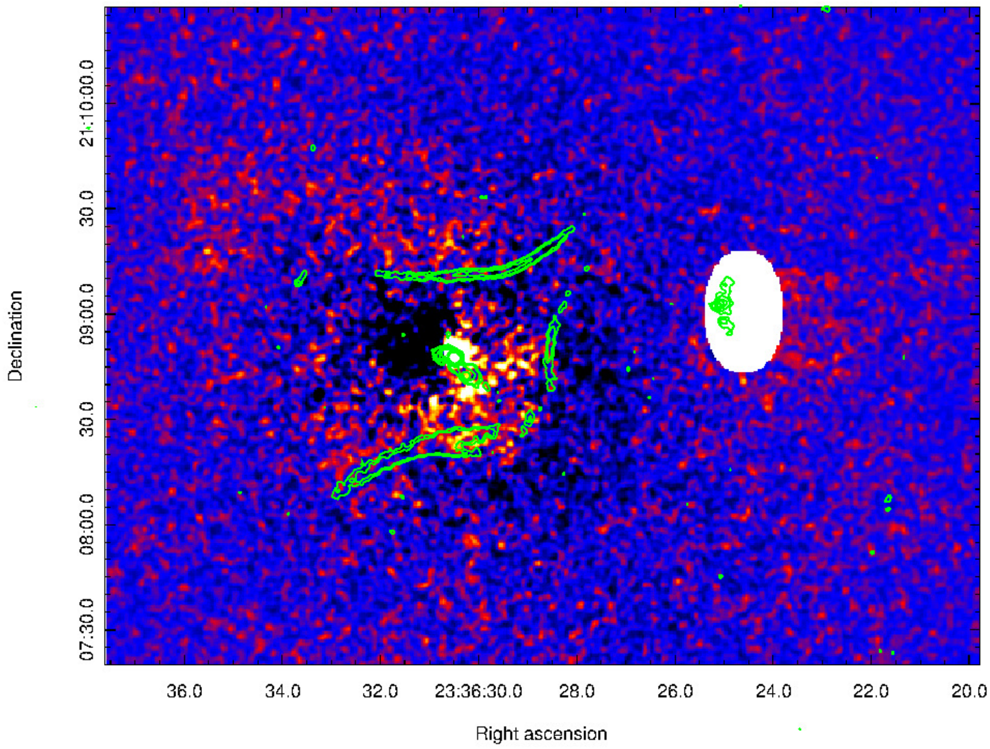

Model	R_0 [kpc]	β
Component 1	$78.74^{+224.12}_{-12.14}$	$2.54^{+12.87}_{-0.55}$
Component 2	$2.21^{+0.85}_{-0.93}$	$0.36^{+0.01}_{-0.02}$

Figure 4.11: Overlay of the residual of the 2-D fit and the contours of the radio emission at 1.4 GHz from Gitti (2013). Positive values are in white-orange scale, whereas the zeros are in blue and the negative ones are in black. In the table are reported the parameters of best-fit. The values differ from the fit of the SB profile due to a different behavior of the 2D model with respect to the 1D model. The emission of IC5337 has been masked with elliptical region because it was not related to the cluster thermal emission.

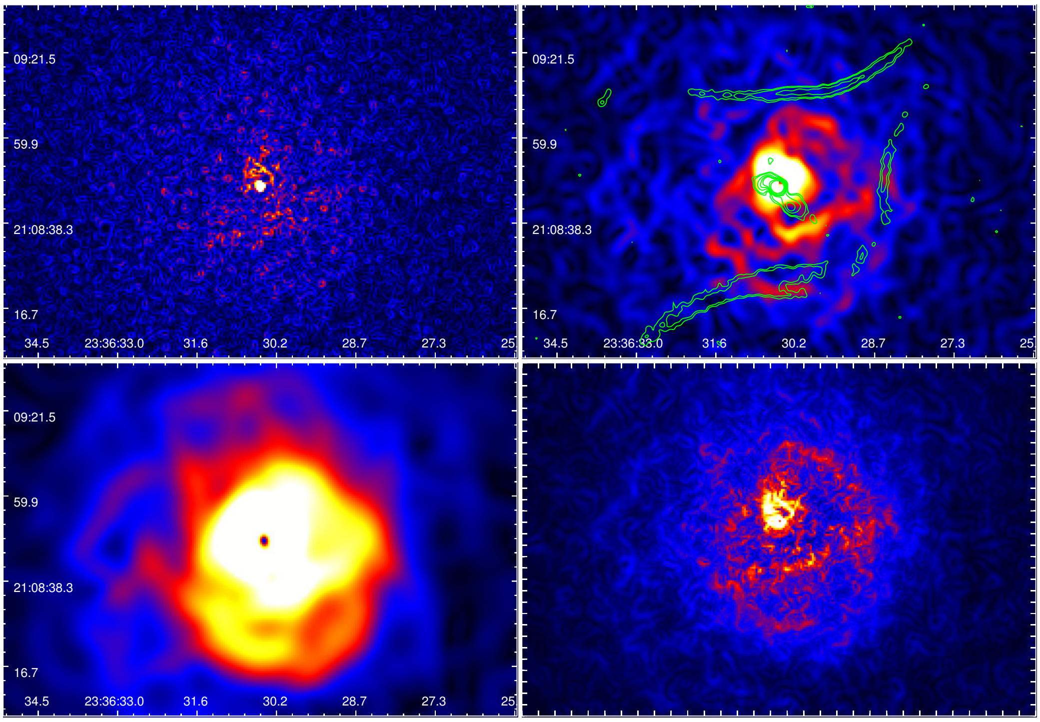

Figure 4.12: The result of the Gaussian filtering: *Top-left:* 1σ filtering; *Top-right:* 4σ filtering. In green are reported the contours of the radio emission at 1.4 GHz (Gitti 2013); *Bottom-left:* 8σ filtering; *Bottom-right:* multi-scale filtering.

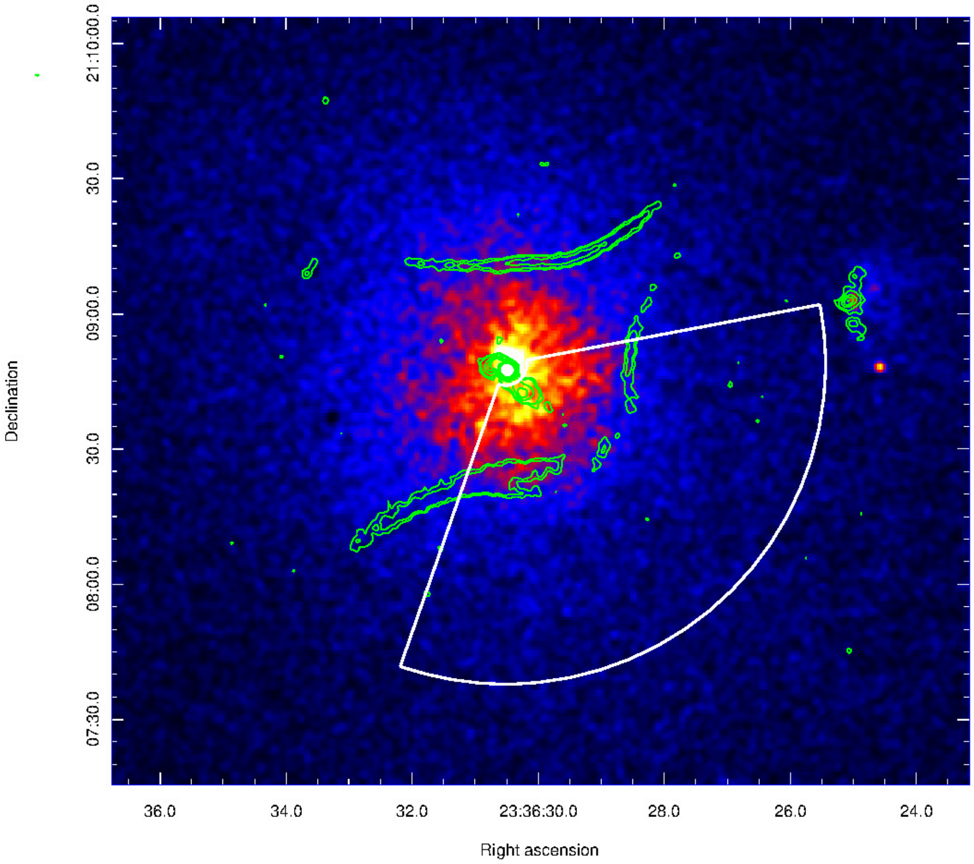

Figure 4.13: The region where we performed the spectral analysis of the S-W junction. In green are overlaid the 1.4 GHz radio contours.

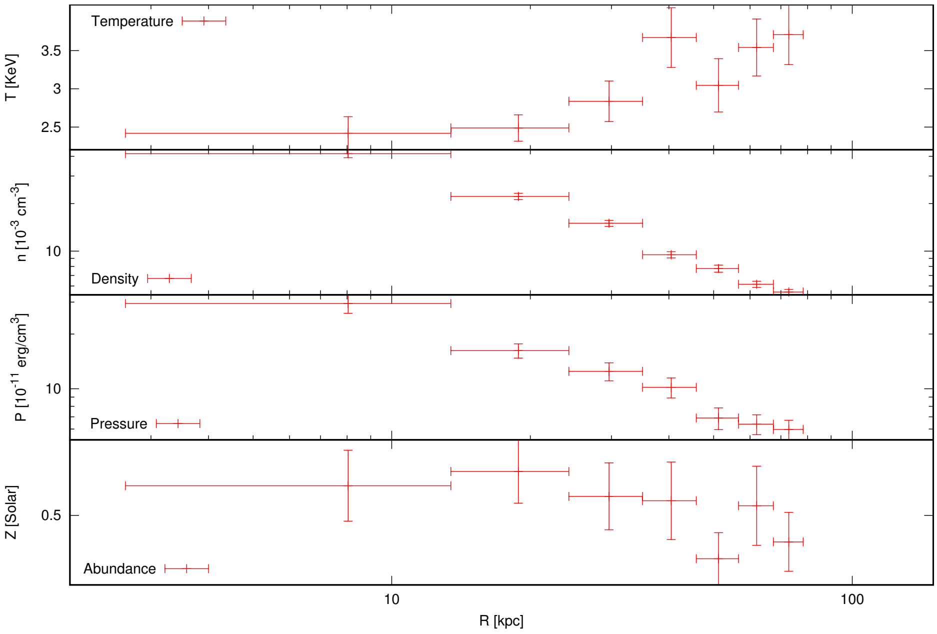

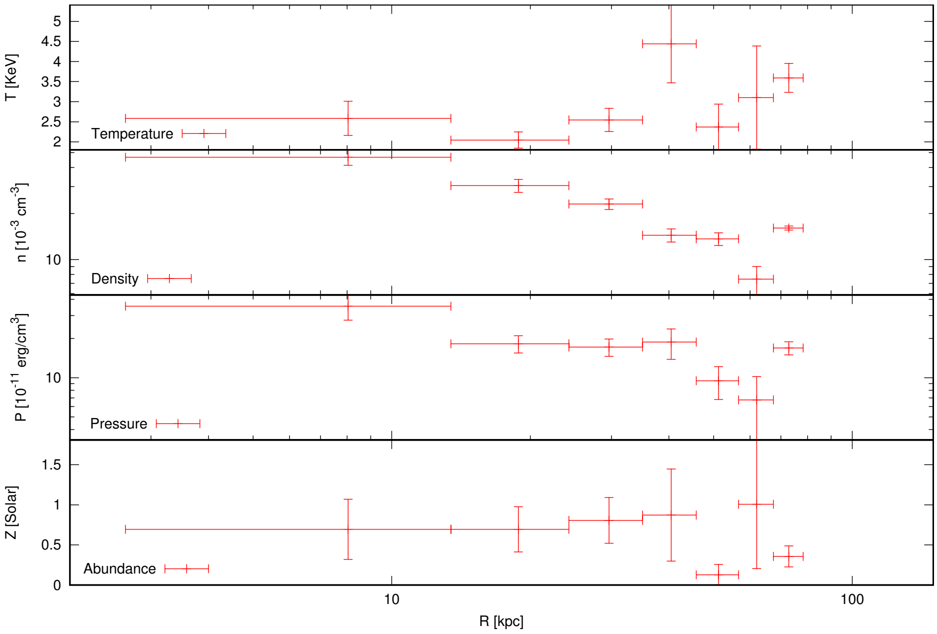

Figure 4.14: The profiles extracted from Fig.4.13. The region has been divided in 7 annuli *Top:* projected profile *Bottom:* de-projected profile.

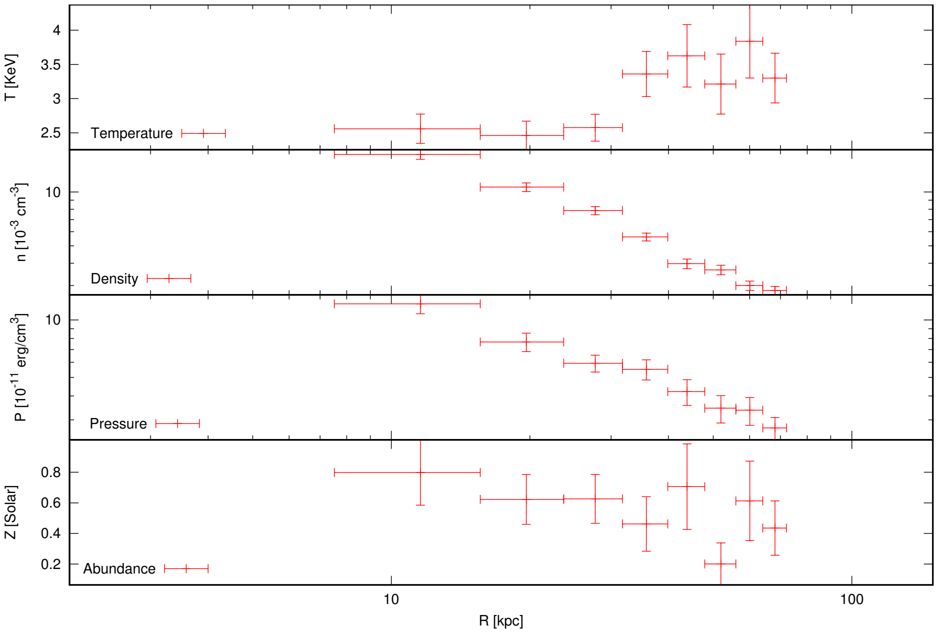

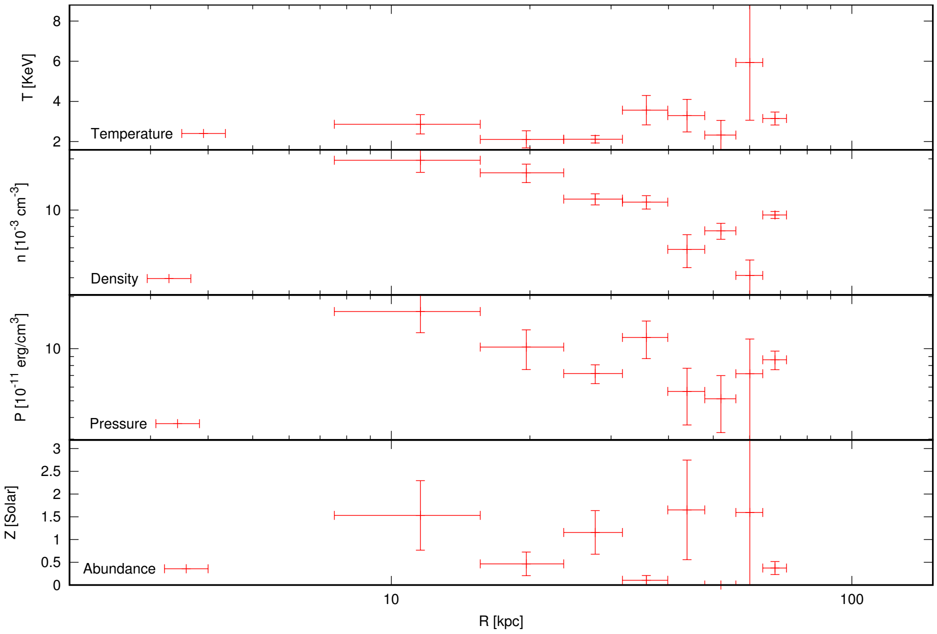

Figure 4.15: The profiles extracted from Fig.4.13. The region has been divided in 8 annuli *Top:* projected profile *Bottom:* de-projected profile.

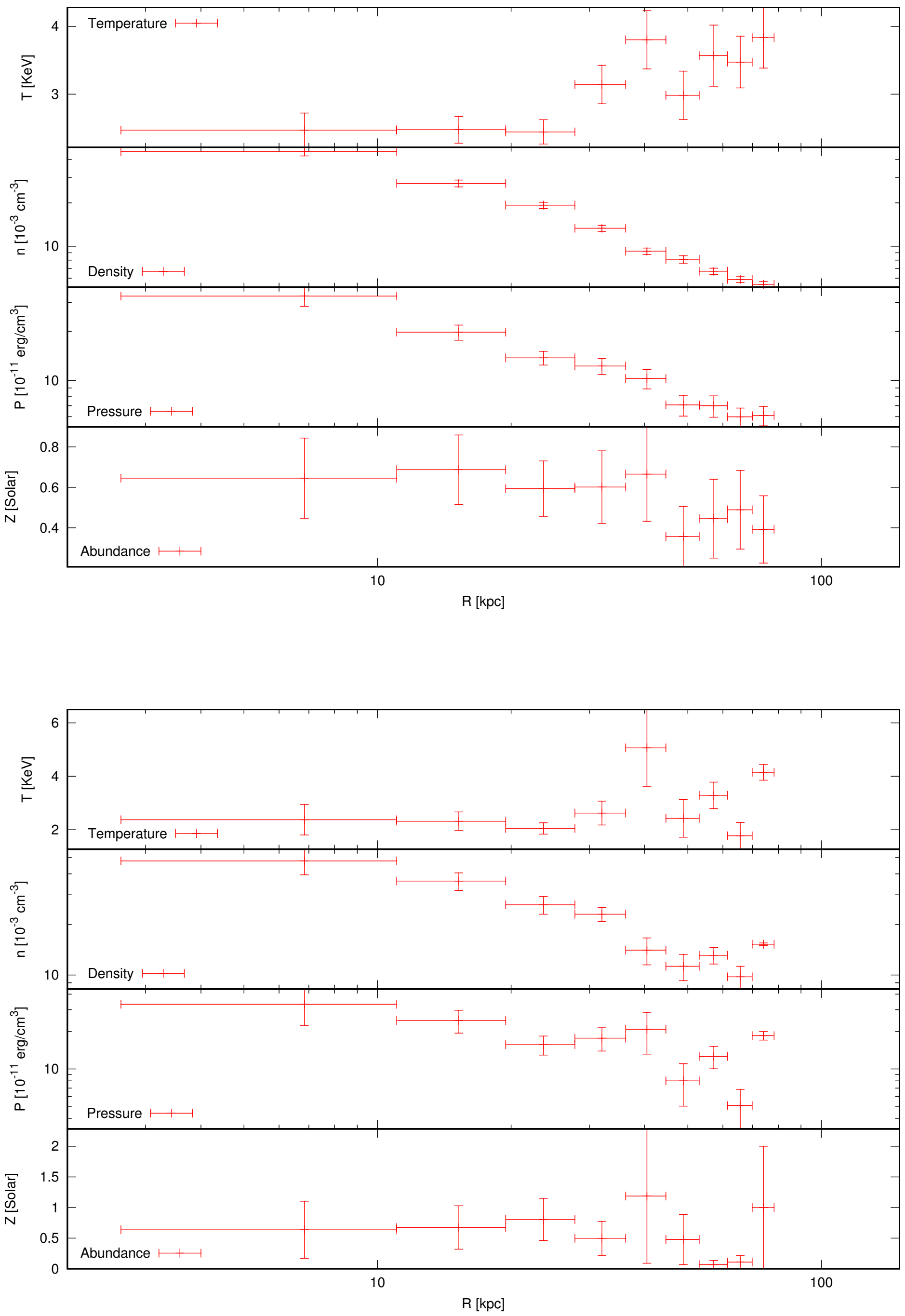

Figure 4.16: The profiles extracted from Fig.4.13. The region has been divided in 9 annuli *Top:* projected profile *Bottom:* de-projected profile.

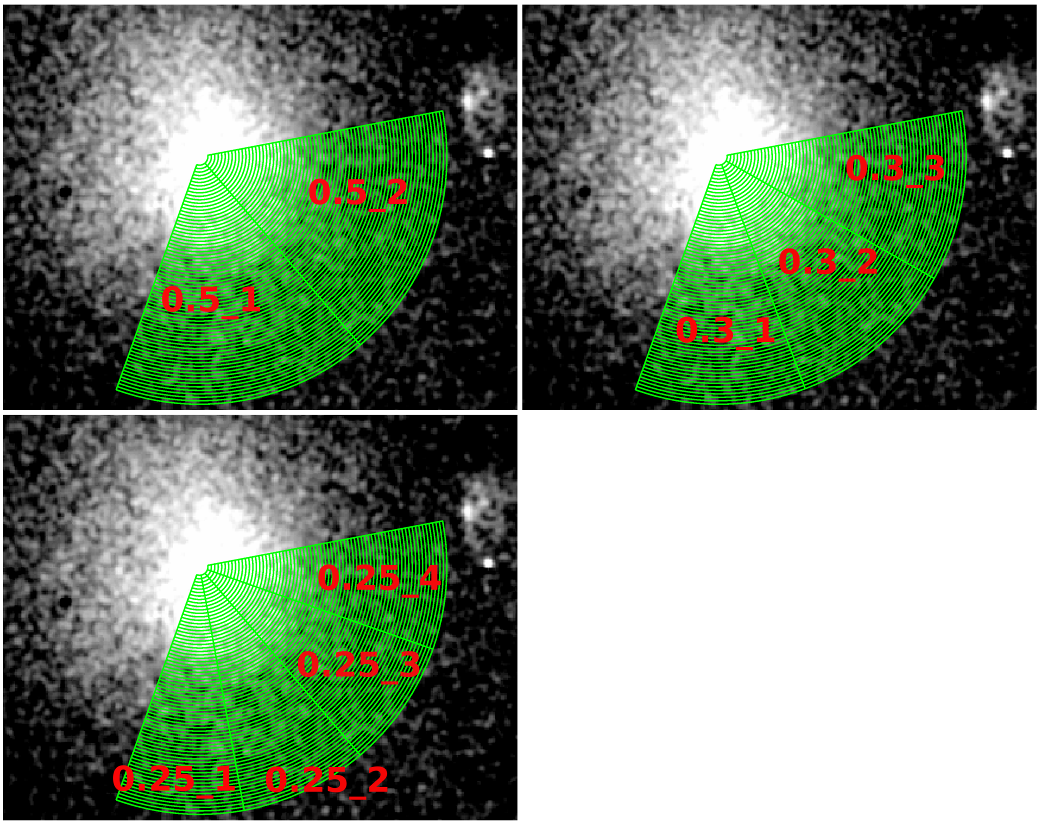

Figure 4.17: Sampling system that we adopted in the SB profiles analysis.

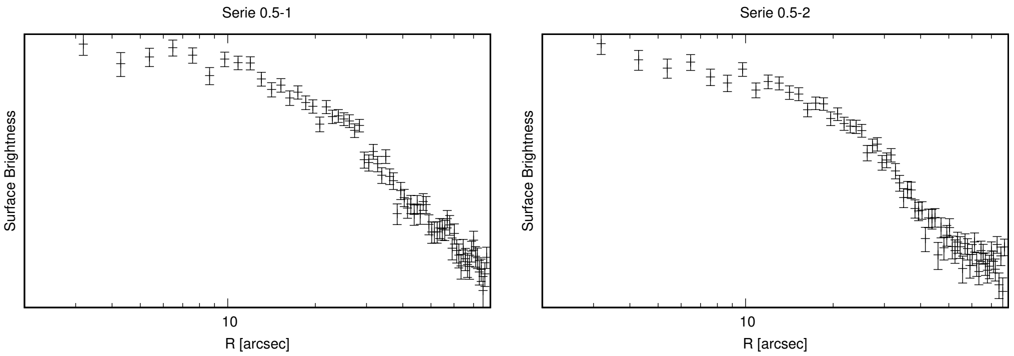

Figure 4.18: Surface brightness profile from each sub-sector of the 0.5 Sequence. The SB is expressed in arbitrary units.

For the analysis of the SB profiles we divided the S-W area (Fig. 4.17) in several sectors with different orientation:

- *Sequence 0.5:* two sub-sectors with amplitude ∼60°;
- *Sequence 0.3:* three sub-sectors with amplitude ∼40°;
- *Sequence 0.25:* four sub-sectors with amplitude ∼30°;

Each sub-sector is composed of 69 annulus with radius 1", and it is enumerated with a number which goes counter-clockwise from South to West (e.g. Fig. 4.17). This sampling method allowed us to individuate also the direction of the discontinuity. We extracted the SB profiles (Fig. 4.18-4.20) from each sector, then we fitted a broken power law model to estimate the brightness jump. The results that we report here have a confidence level of 90% using $\Delta\chi^2$=2.7, which correspond to 1.65 σ.

Only three sub-sectors, namely *0.3-1*, *0.3-3* and *0.25-1*, exhibit a clear discontinuity in surface brightness. In Fig.4.24 we report the results of these fits. For each profile we report the radius of the front and the value of the *Density jump*, that is the ratio between the inner and the outer density.

The others profiles have a more complex structure which might indicate the presence of several minor fronts.

The profiles in Fig. 4.24 point out the presence of a couple of SB discontinuities located at ∼29.5 and ∼26.3 kpc from the center of the cluster. We estimated the final spectral profiles over these region (e.g. Fig. 4.25) by placing two sectors, the second and the third, exactly across the discontinuities (Fig. 4.26 and 4.27) in order to maximize the effects of the jump on the spectral profiles.

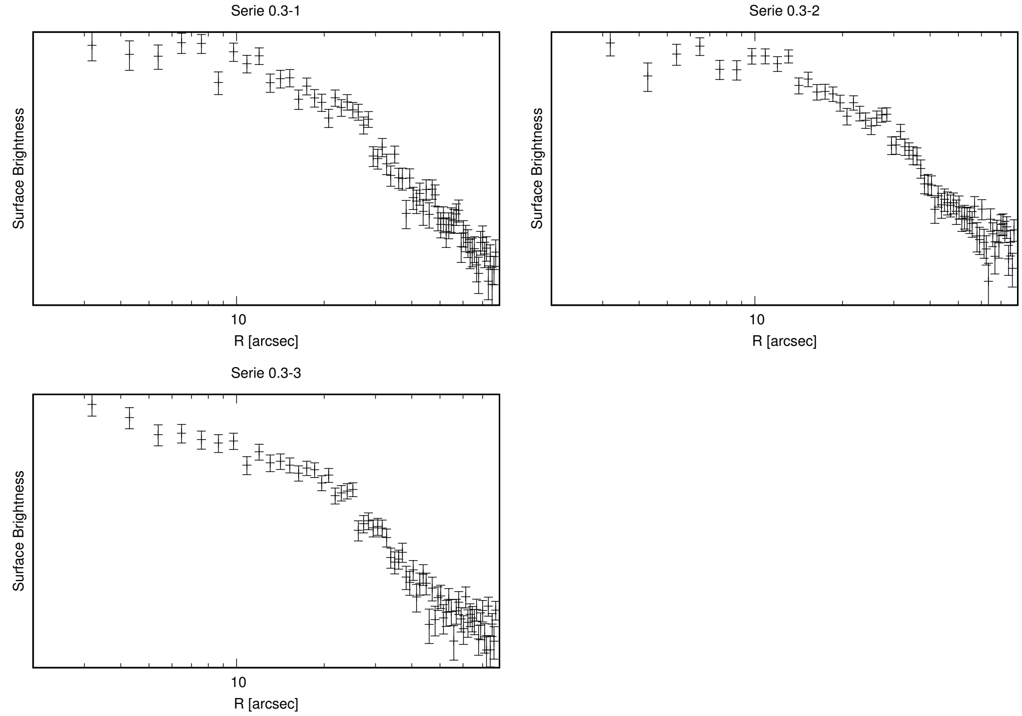

Figure 4.19: Surface brightness profile from each sub-sector of the 0.3 Sequence. The SB is expressed in arbitrary units.

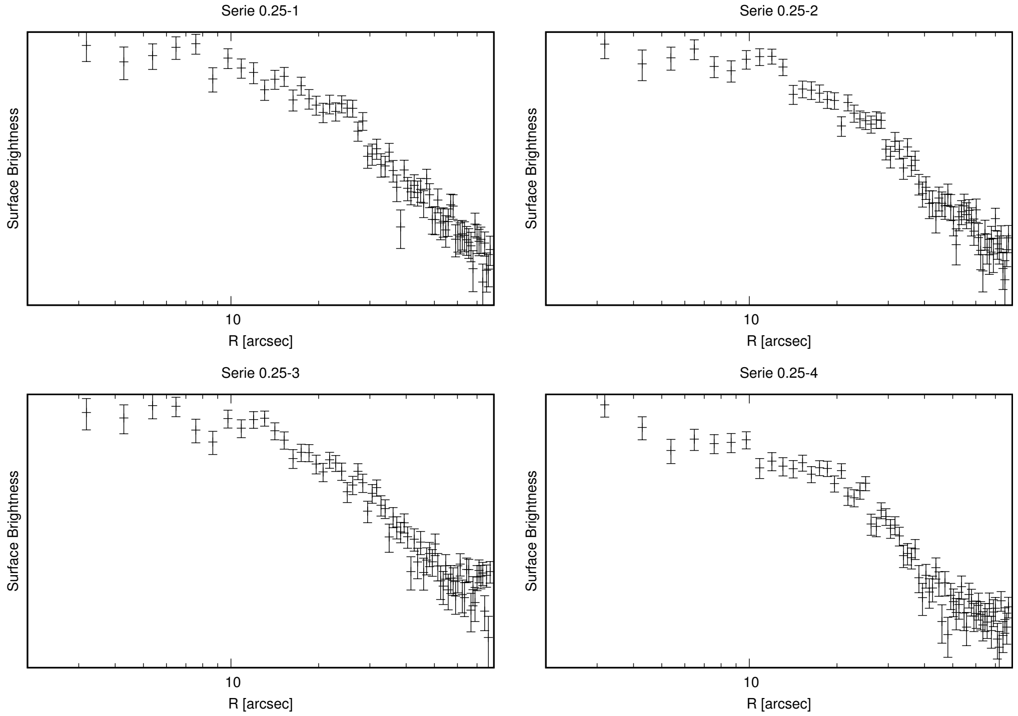

Figure 4.20: Surface brightness profile from each sub-sector of the 0.25 Sequence. The SB is expressed in arbitrary units.

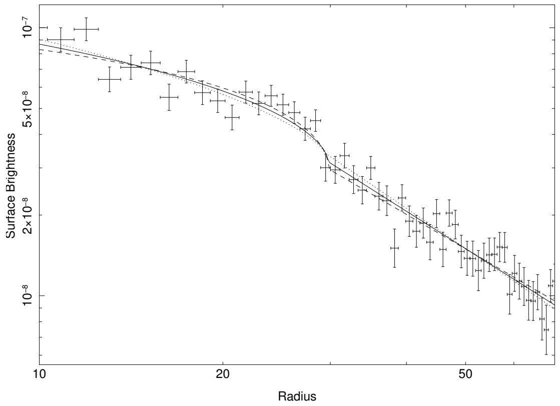

Figure 4.21: Profile of *0.3-1*. Front radius=29.7 kpc, Density jump=$1.27^{+0.22}_{-0.18}$

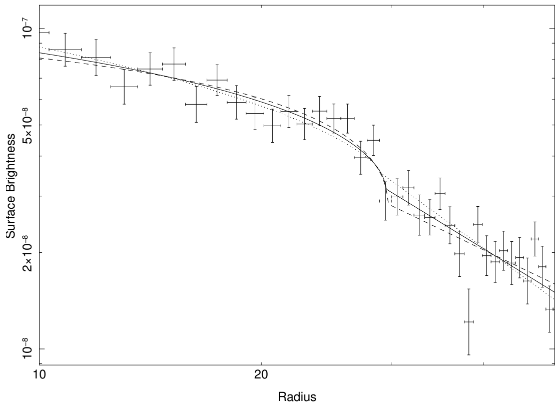

Figure 4.22: Profile of *0.25-1*. Front radius=29.5 kpc, Density jump=$1.31^{+0.27}_{-0.21}$

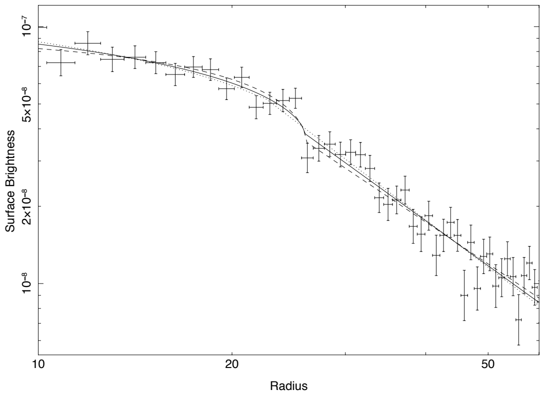

Figure 4.23: Profile of *0.3-3*. Front radius=26.3 kpc, Density jump=$1.36^{+0.16}_{-0.14}$

.

Figure 4.24: Surface brightness profiles fitted with the broken-power law model.

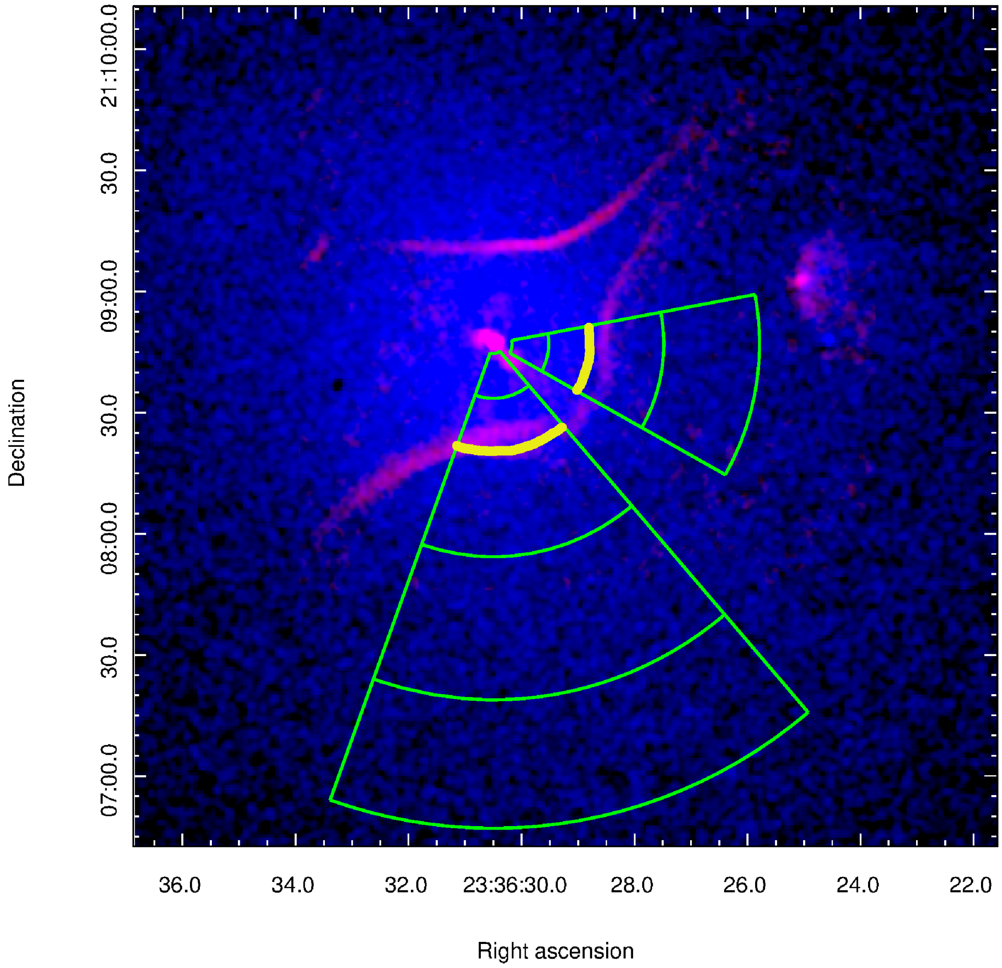

Figure 4.25: *Blue:* Image of the thermal X-rays emission between 0.5-7.0 keV *Red:* Non-thermal emission at 1.4 GHz from Gitti (2013) *Green:* regions where we extracted the profile reported in Fig. 4.26 and Fig. 4.27. The discontinuities observed in the fits, that we have highlighted in yellow on each sector, follow the shape of the radio emission.

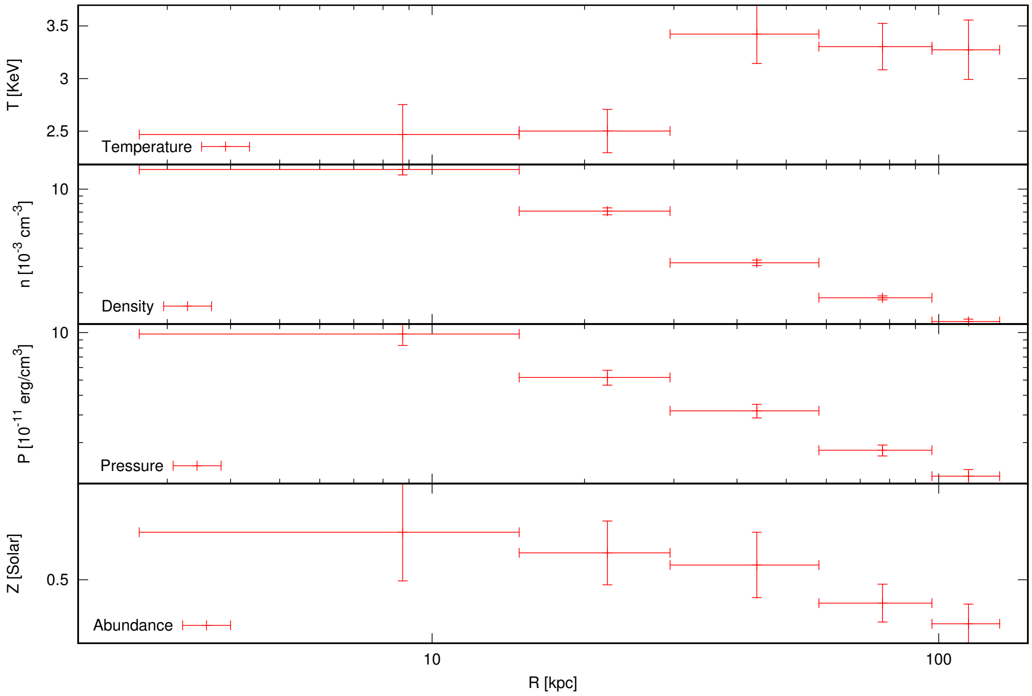

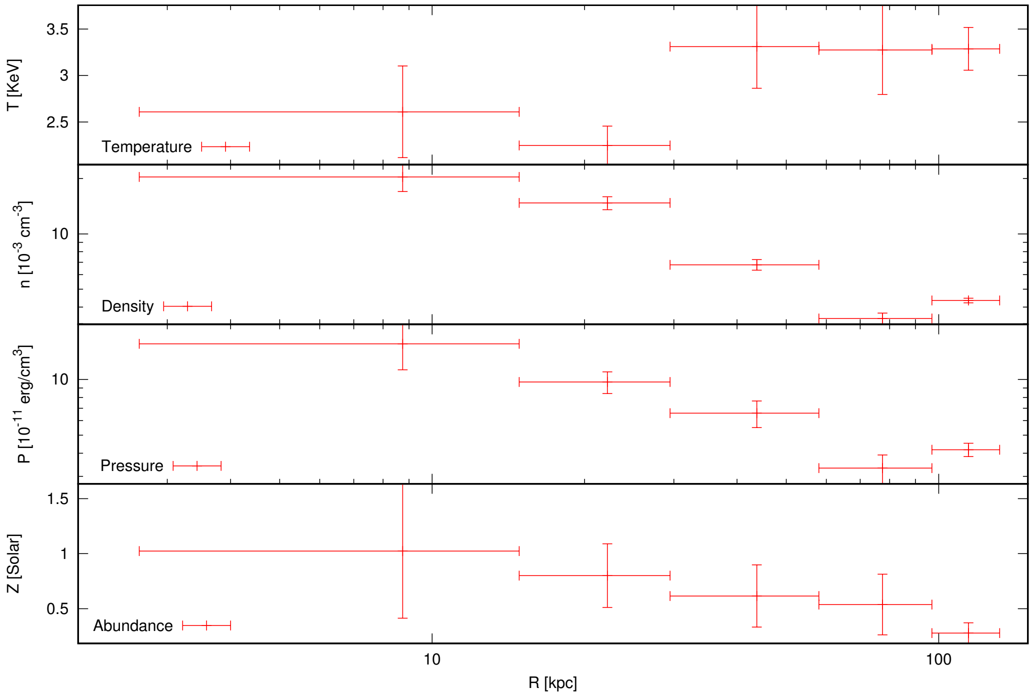

Figure 4.26: Profiles of the thermal properties across the jump at ∼29.5 kpc. *Top:* Projected profiles; *Bottom:* De-projected profiles

Table 4.2: Summary of the analysis of the discontinuities

R=29.5 kpc			
Temperature	Projected	$T_1 = 2.5^{+0.2}_{-0.2}$ $T_2 = 3.4^{+0.4}_{-0.3}$	Confidence:4.1σ
	De-Projected	$T_1 = 2.2^{+0.3}_{-0.2}$ $T_2 = 3.3^{+0.6}_{-0.4}$	Confidence:3.3σ
Density	Sector 0.3-1	$Dens.Jump = 1.3^{+0.2}_{-0.2}$	Confidence:2.4σ
	Sector 0.25-1	$Dens.Jump = 1.3^{+0.3}_{-0.2}$	Confidence:2.4σ
R=26.3 kpc			
Temperature	Projected	$T_1 = 2.3^{+0.3}_{-0.3}$ $T_2 = 3.3^{+0.6}_{-0.3}$	Confidence:3.6σ
	De-Projected	$T_1 = 2.0^{+0.3}_{-0.3}$ $T_2 = 3.3^{+1.0}_{-0.6}$	Confidence:3.3σ
Density	Sector 0.3-3	$Dens.Jump = 1.3^{+0.2}_{-0.2}$	Confidence:2.4σ

Each front is characterized by temperature and density jumps. The pressure does not exhibit any discontinuity, and so does the abundance. The density jump can be observed on both the spectral and the SB profiles. Due to the improved spatial resolution, we favored the estimate which came from the SB profiles.
We estimated the statistical confidence of the jumps (Tab. 4.2) and we find that overall our jump detections are close to the 3 σ.
Both fronts exhibit the characteristic properties of a cold front, that are sharp contact discontinuities between regions of gas with different entropies (e.g. Markevitch and Vikhlinin 2007).
We argue so that the brightness jumps that we observe are related to a cold front, whose position correspond to the radio arcs.

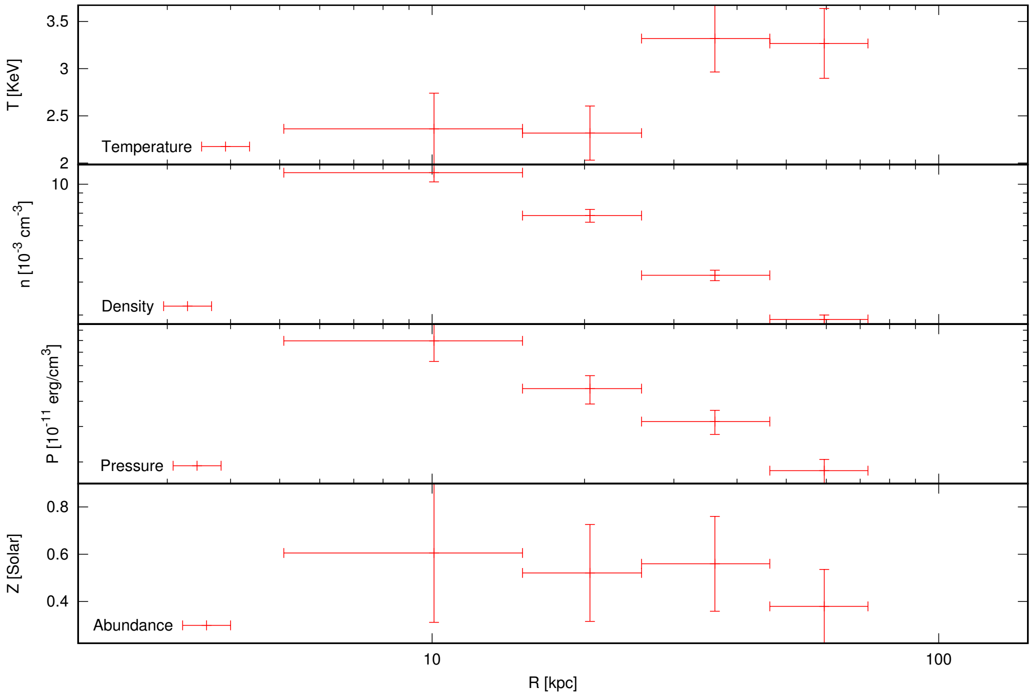

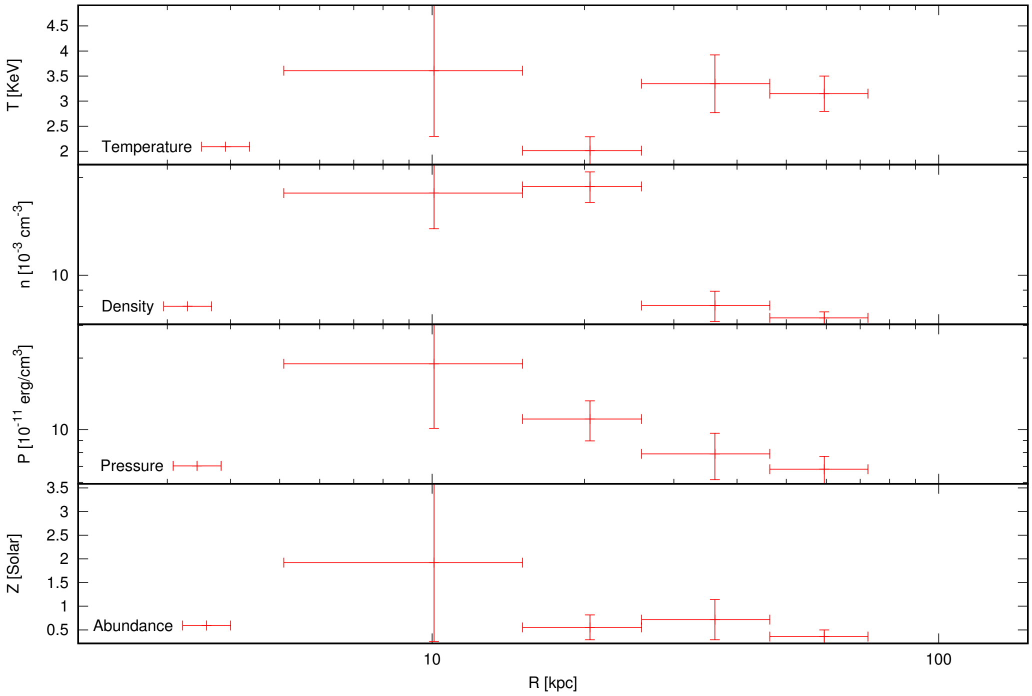

Figure 4.27: Profiles of the thermal properties across the jump at ∼26.3 kpc. *Top:* Projected profiles; *Bottom:* De-projected profiles

Chapter 5

On the origin of the radio arcs

We present here our interpretation about the nature of the radio arcs observed in A2626. We propose a connection between the origin of the radio arcs emission and the dynamics of the ICM.

5.1 Constraining the jet-precession model

As mentioned in the Introduction, the reference model to explain the origin of the arcs is the jet-precession model. According to this model, the arcs are the contrails of the hot-spots of a pair of jets, that trailed as result of the gravitational interactions between two super massive black holes (SMBH) inside IC5338. For this reason, the arcs would exhibit properties similar to that of the radio plasma that is accelerated and then released in the hot-spots of radio galaxies.
We derived constrains on the time of the precession, by starting from the results of the radio spectral maps. We assumed that the plasma initially was accelerated in an hot spot, so it would have an initial spectral index α =-0.7 (Meisenheimer et al. 1997). According to the synchrotron emission theory (Pacholczyk 1970), the continuous energy loss modify the emission spectrum, decreasing the value of the break frequency ν_{br} with time and steepening the spectrum. Therefore, by comparing the spectral index that we observe with the initial spectral index we can estimate the radiative time of the particles.
According to the jet-precession model, the time elapsed since the acceleration along the arcs should increase from one end to the other end of the structures. This should unavoidably produce a spectral steepening along the arcs. The fact that we do not observe the steepening challenges this scenario, or at least it constrains the difference in time elapsed since the acceleration along the arcs.

We estimated this difference in radiative time, Δt_{rad}, on each arc and we argue that this is an estimate of the time required to the jets to cover the arcs length, therefore it is related to the precession period.

The absence of a clear trend of the spectral index along the arcs (Fig. 3.16-3.18) implies that the precession time-scale has to be significantly shorter than Δt_{rad}. If the precession of the jets is sufficiently fast, the plasma, which is deposited by the jets, will be spread on a large angle in a short while. So, there will be a small difference in the spectral index, thus in the Δt_{rad}, between two contiguous "chunks" of the arcs.

The radiative time, according to the JP model (Jaffe and Perola 1974), can be estimated as:

$$t_{rad} = \frac{1.62 \cdot 10^3 \sqrt{H}}{(H^2 + H_{CMB}^2)\sqrt{\nu_{br}}} \text{ Myr} \tag{5.1}$$

H_{CMB} is the equivalent magnetic field of the cosmic microwave background (CMB), that interacts with the electrons by the Inverse Compton scatter, and it is defined as:

$$H_{CMB} = 3.25(1+z)^2 \ \mu\text{G} \tag{5.2}$$

H is the local magnetic field of the radio source, that is assumed to be constant in its whole volume and that it has remained constant over the source life. Given the very steep spectrum that is measured for the radio arcs, the observing frequencies are greater than the break frequency. Under the condition $\nu >> \nu_{br}$ from synchrotron theory it is possible to derive a simple relationship between the observed radio spectral index, observing frequency and radiative age of the emitting electrons (Appendix A) :

$$\alpha(t_{rad}) = \frac{(1-R)}{ln(R)} \frac{[3.25(1+z)^2]^3}{8.5 \cdot 10^5} \left(\frac{\nu_1^{obs}}{[\text{GHz}]}\right) \left(\frac{t_{rad}}{[\text{Myr}]}\right)^2 - \frac{\Gamma - 1}{2} \tag{5.3}$$

This equation allows us a to derive straightforwardly the radiative age of the radio emitting plasma from the measured spectrum :

$$t_{rad}(\alpha) = \sqrt{\frac{ln(R)}{(1-R)} \frac{8.5 \cdot 10^5}{[3.25(1+z)^2]^3} \left(\frac{\nu_1^{obs}}{[\text{GHz}]}\right)^{-1} \left(\alpha + \frac{\Gamma - 1}{2}\right)} \text{ Myr} \tag{5.4}$$

where Γ is the injection index of the particles energy distribution, $n(E) \propto E^{-\Gamma}$, R is the ratio between the observed frequencies ν_1^{obs} and ν_2^{obs}, and z is the red-shift.

The $t_{rad}(\alpha)$ relation (Eq. 5.4) allows to obtain a *radiative age map* from the spectral index map. We produced two radiative age maps, one by assuming the

the magnetic field H=2.08 μG (Fig. 5.1) that is the magnetic field that minimizes the energy loss (see appendix A for further details), and one by assuming the equipartition magnetic field H_{eq}=12 μG (Fig. 5.2), that we obtained as:

$$H_{eq} = \sqrt{\frac{24\pi u_{min}}{7}} \tag{5.5}$$

where

$$u_{min} = 1.23 \cdot 10^{-12}(1+k)^{4/7}\nu_o^{4\alpha/7}(1+z)^{(12+4\alpha)/7}I_o^{4/7}d^{-4/7} \tag{5.6}$$

where I_o is the surface brightness at the frequency ν_o, d is the thickness of the radio source and k is the ratio of the energy of the relativistic protons to that in electrons (Murgia et al. 2004). The classical equipartition formula (Pacholczyk 1970) is obtained for a power law energy distribution of electrons. On the other hand, we detect a synchrotron spectrum whose properties are affected by radiative ageing. In order to correct for this effect we anchored the formula to the spectrum of the arcs at lower frequencies and, to do that, we calculated the emission at frequency 100 MHz from the spectrum measured at 1.4 GHz assuming a break frequency derived from the spectral slope between 1.4 and 3.0 GHz. We estimated the surface brightness at 100 MHz ,I_{100MHz}, from the flux density S_{100MHz}=264 mJy, estimated by re-scaling $S_{1.4}$ according to the synchrotron spectrum:

$$J_{sy}(k) = \int_0^\infty \int_0^\infty F(k,H)\ n(E)dEdH \tag{5.7}$$

where $F(k,H)$ is the synchrotron kernel of a single electron and $n(E)$ is the distribution function of the energy of the population. We produced the radiative age maps from the `NATURAL` spectral index map (Fig. 3.9). The value of the injection index Γ was derived from the hypothesis that the particles were initially accelerated in an hot-spot, that is the cardinal hypothesis of the jet-precession model, i.e.:

$$\Gamma = 1 - 2\alpha = 2.4 \tag{5.8}$$

Based on these assumptions, the radiative age maps show an estimate of the distribution of the time that has elapsed since the epoch when the plasma was accelerated.

The difference in the assumed magnetic field results is a significant difference in the radiative age, thus providing two different estimates of the age of the arcs. The radiative age map in Fig. 5.1 locates the origin of the arcs ∼130 Myr ago. Due to the hypothesis on the magnetic field, this is the upper limit of the possible age of plasma, according to the jet-precession model. On the other hand, the radiative age map in Fig. 5.2 suggests that the arcs are only ∼35

Myr old. Despite of this difference, both radiative maps provide a $\Delta t_{rad} \sim$ 5-10 Myr, thus resulting on a tight constraint for the parameters of the jet-precession model.

We estimated the precession periods of the jets, by starting from the fact that IC5338 exhibits a pair of optical cores with a projected distance of 3.3 kpc. Wong et al. (2008) assumed that the interaction of the two cores is responsible for the precession of the jets. Since their masses have never been estimated in any previous studies, we assumed a reference mass value=10^8 $M_\odot$.
A binary system of massive compact objects admits the precession of the rotation axis. Abraham and Caproni (2003) derived an estimate for the precession period, P_{prec}, of this kind of objects:

$$\frac{2\pi}{P_{prec}}(1+z) = -\frac{3}{4}\left(\frac{7-2n}{5-n}\right)\frac{GM_s}{R_{ps}^3}\frac{r_D^2}{\sqrt{GM_p r_D}}cos(\theta) \tag{5.9}$$

where M_p is the mass of the emitting AGN, M_s is the perturbing object and R_{ps} is the distance between the AGN and the perturbing object. The disk is parametrized by n, which is $n = 3$ if the matter of the disk is relativistic, or $n = 0.66$ otherwise, and its radius r_D. The parameter θ is the angular separation between the plane of the orbit and the disk. They argued that the gravitational tidal forces are able to disturb the accretion disk of the AGN, which is bounded to the jets, triggering the precession of the jets.
By assuming $M_1 = M_2 = M$, $R_{ps} = 3.3$ kpc, $n = 0.66$, $\theta = 0$ and $r_D = 1$ pc, we derived an estimate of the precession period as function of the masses of the bodies from Eq. 5.9:

$$P_{prec} = \frac{3.5 \cdot 10^5}{\left(\frac{M}{10^8 M_\odot}\right)^{1/2}} \text{ Gyr} \tag{5.10}$$

This is extremely long, because the present distance between the two SMBHs is large enough that the mutual gravitational interactions are negligible.
As a first approximation, from Eq. 5.9 we can estimate the fly-by distance R_m that would be necessary to induce a jet precession time $\leq 2\Delta t_{rad} \sim 20$ Myr and the velocity V of the cores orbiting at such radius:

$$R_{fb} = 12.3\left(\frac{M}{10^8 M_\odot}\right)^{1/6} \text{ pc} \tag{5.11}$$

By assuming an instantaneous interaction between the two bodies, we evaluated V from the energy conservation:

$$\frac{1}{2}MV^2 = -U = \frac{GM^2}{R_{fb}} \tag{5.12}$$

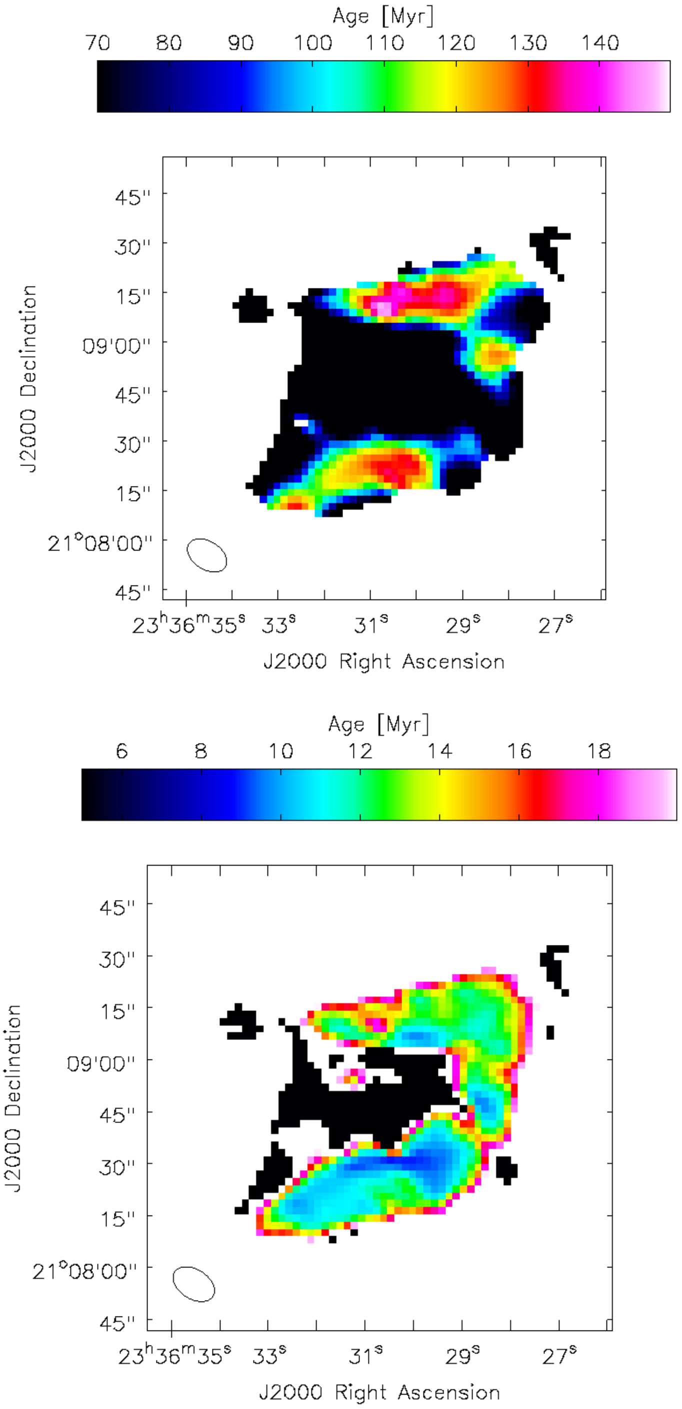

Figure 5.1: Radiative Age map (top) and error map (bottom) of A2626, obtained from the spectral index map in Fig. 3.9. The parameters are: ν_1=1.4 GHz, ν_2=3.0 GHz, R=2.14, z=0.0553, H_{eq}=2.08 μG, H_{CMB}=3.61 μG, and Γ=2.4. The black regions are upper limit to the radiative age.

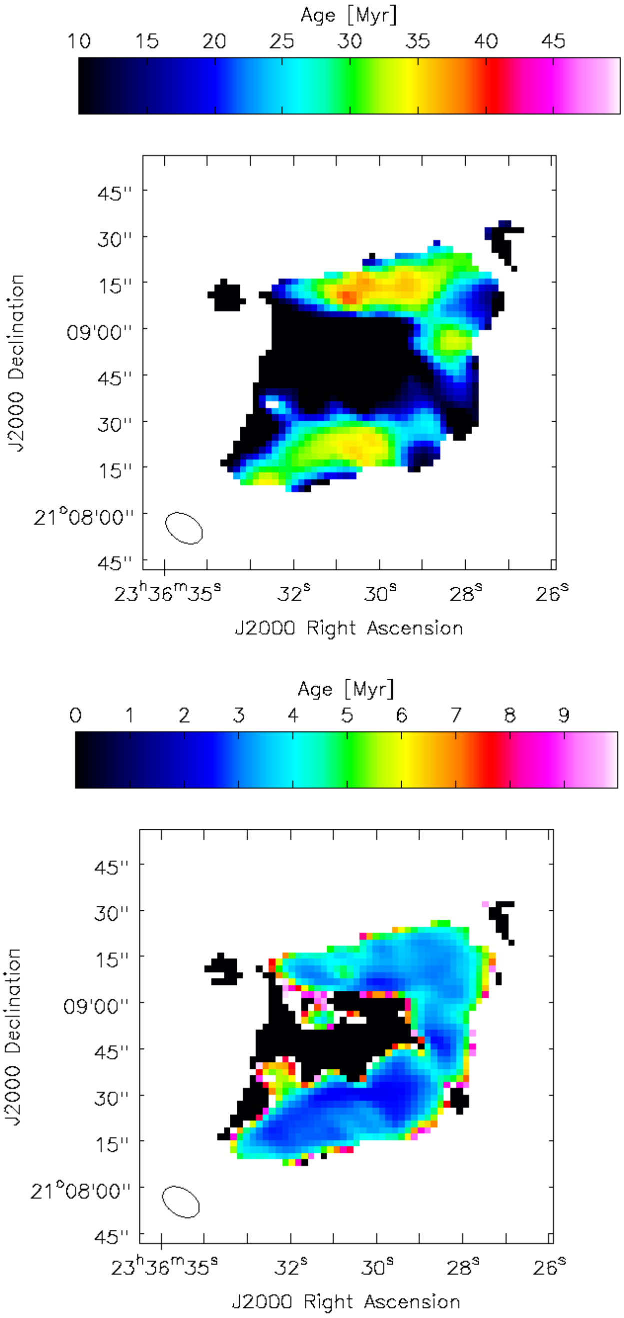

Figure 5.2: Radiative Age map (top) and error map (bottom) of A2626, obtained from the spectral index map in Fig. 3.9 in condition of Equipartition. The parameters are: ν_1=1.4 GHz, ν_2=3.0 GHz, R=2.14, H_{eq}=12.1 μG, H_{CMB}=3.61 μG and Γ=2.4. The black regions are upper limit to the radiative age.

so

$$V = \sqrt{\frac{2GM}{R_{fb}}} = 267 \left(\frac{M}{10^8 M_\odot} \right)^{5/12} \text{ km/s} \tag{5.13}$$

This fly-by happened about Δt_t ago, where Δt_t is the sum of the age of the radio plasma released from the hot-spots tracing the radio arcs ($t_{rad} \sim 35 - 130$ Myr, Eq. 5.4) and of the jet travel time from the core to the radio arcs. The latter one is a few Myrs assuming typical jet propagation speeds in the ICM ($V_h \sim 0.02c$,Kaiser and Alexander (e.g. 1997)). After this fly-by the two cores moved from each other and reached a present-time distance R_n :

$$\begin{aligned} R_n &= R_{fb} + V_E \Delta t_t = \\ &= 12.3 \left(\frac{M}{10^8 M_\odot} \right)^{1/6} \text{ pc } + 267 \left(\frac{M}{10^8 M_\odot} \right)^{5/12} \text{ km/s} \cdot 50 \text{ Myr} = \\ &\simeq 14 \left(\frac{M}{10^8 M_\odot} \right)^{5/12} \text{ kpc} \end{aligned} \tag{5.14}$$

This, however, is in disagreement with the observed distance, that is only 3.3 kpc, although it is also possible that projection effects play a role. This estimate is an approximation based on several assumptions, so it should be considered only as a *zeroth-order* test for the jet-precession model.

Nevertheless, our results challenge the jet-precession model or, at least, they provide strong constrains on the time-scale of the precession and the dynamics of the interacting bodies. Accurate simulations are necessary to further explore the challenges of this model.

5.2 A new possible scenario for the origin of the arcs?

In this Section we look for an alternative scenario for the origin of the extended radio emission from the arcs. Relativistic particles in galaxy clusters can be accelerated, or re-accelerated, by a hierarchy of processes operating in the ICM (e.g. Brunetti and Jones 2014). Radio mini-halos in cool-core clusters can be generated by turbulence that can be produced by several mechanisms, including the sloshing of the gas in cold fronts.

Based on the observational evidences that we have reported in this Thesis (Chapter 4), in this Section we propose that the radio arcs are the brightest parts of a faint mini-halo with very steep spectrum. This scenario was yet qualitatively proposed by Gitti (2013). Following the results of ZuHone et al. (ZuHone et al. (2011), ZuHone et al. (2013)), sloshing of the gas in cold fronts in cool-cores

clusters can generate turbulence that amplifies magnetic fields and re-accelerate relativistic electrons. This process may result in the generation of diffuse synchrotron radiation on cluster-core scales in the form of radio mini-halos.
According to (ZuHone et al. 2013), the strongest magnetic fields are generated at the fronts, where turbulence is injected more effectively by contact instabilities in the gas. In the cases where turbulent re-acceleration is not efficient enough to generate cluster-core wide sources, the resulting synchrotron emission has a very steep spectrum and may trace preferentially the narrow regions around the front discontinuities.
An example is given in Fig. 5.3 where, under some circumstances, the morphology of the emission predicted by these models appears in radio bright filaments, qualitatively similar to the radio arcs in A2626. The fact that the radio arcs surround the low temperature region in the cluster core and that the SW arc is remarkably connected to a cold front as shown in Sect. 4 supports this possibility. Obviously a number of points remain open:

- We observed only one cold front connected with two radio arcs, but there are four of them (Kale and Gitti 2017). Assuming that the south and west arcs were produced by the cold front that we observe, at least two other cold fronts should be present to explain the origin of the other radio arcs. We do not find evidence of them, but it may be possible that they are hidden by projection effects, or that are undetected at the sensitivity level of our CHANDRA observation;

- The most relevant open issue is the geometry of the radio arcs. Unlike typical radio filaments produced in ZuHone et al simulations (Fig. 5.3), the curvatures of both the radio arcs and the cold front of A2626 are directed outside. The curvature of radio filaments in simulations is however connected with the structure and dynamics of the cold fronts. Therefore, provided that the filaments are due to turbulent re-acceleration, the unusual curvature of the radio filaments would constrain a complex, unusual, dynamics of the sloshing of the gas in the core of A2626. Even considering complicated 3D projection effects, a very *fine-tuning* combination of spirals would be necessary to reproduce the peculiar morphology of A2626. This point will be tested with adequate simulations in the future.

Due to the steep spectra of the extended emission, we expect that the flux density of the arcs at 100 MHz should be ∼260 mJy, so we argue that the cluster will be an excellent study subject for LOFAR. In addition, according to (ZuHone et al. 2013), the faint diffuse emission embedding the radio filaments on a cluster-core scale should glow-up at low redio frequencies (e.g. Fig. 5.3), thus LOFAR observations may test our interpretation of A2626.

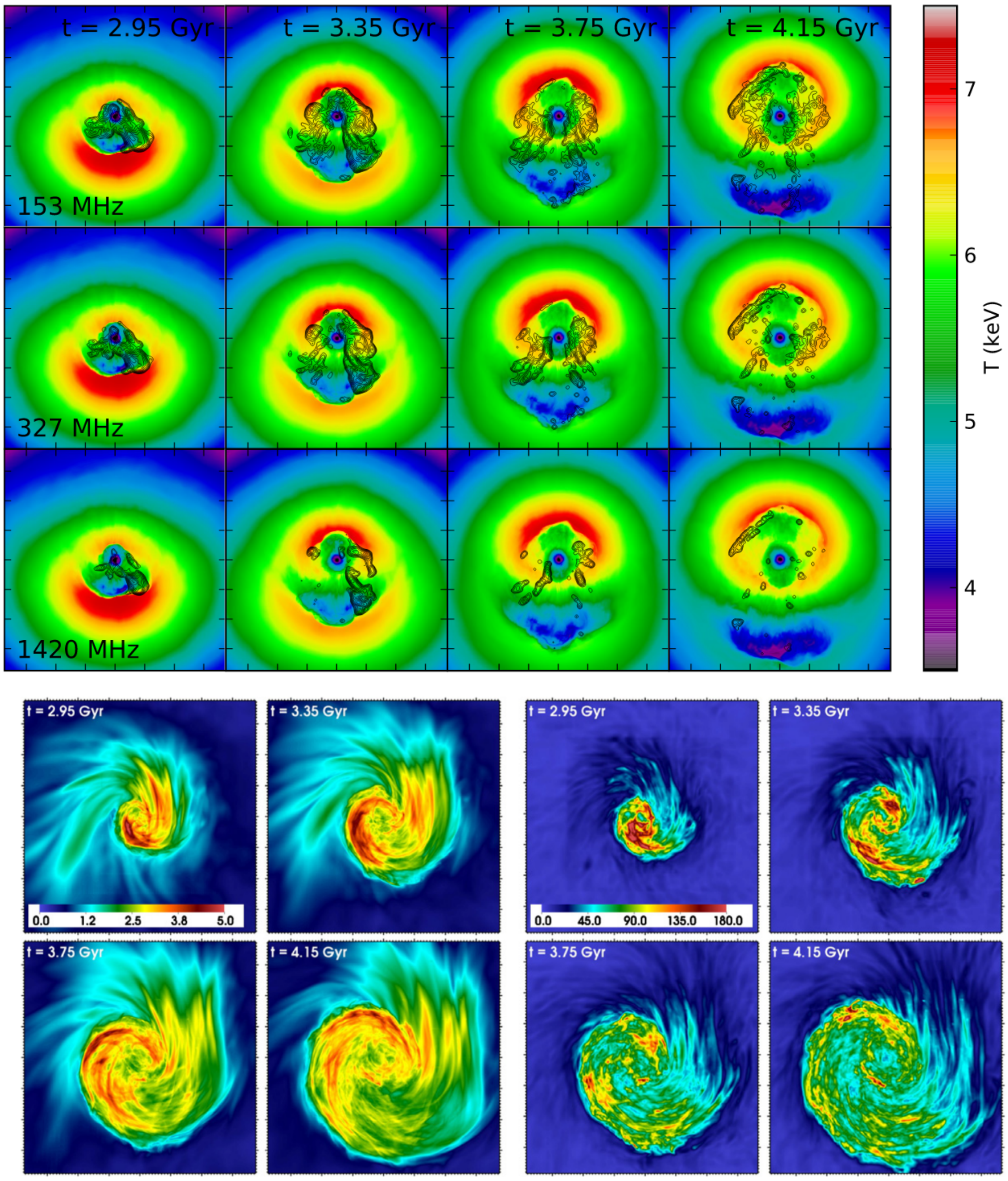

Figure 5.3: Results of the simulations of the particles acceleration (ZuHone et al. 2013). *Top:* Projected gas temperature maps with radio contours overlaid at several epochs for the frequencies 153, 327, and 1420 MHz in the x-projection. The radio filaments in the bottom-right panel resemble the radio arcs; *Bottom:* Magnetic field strength for several epochs. The distribution follows the morphology of the cold fronts.

Chapter 6

Conclusions

Abell 2626 is a massive and nearby cool-core cluster with two optical cores, that hosts an unusual diamond-like radio source formed by four symmetric arcs. A number of models have been proposed for the origin of this unusual radio source, the reference one assumes that the radio arcs are generated by the precession of the radio jet of the AGN in the cluster center.
In this work we analyzed both the radio and X-rays emission of the cluster, by exploiting the newest observation with JVLA and CHANDRA. Our aim was to investigate the interplay between the thermal and non-thermal phenomena that are responsible for the origin of the arcs.
The main results of the radio analysis can be summarized as follows:

- We detected for the first time the arcs at 3.0 GHz. Until now they were observed only at 610 MHz and 1.4 GHz;
- We detected the diffuse emission of the head-tail galaxy IC5337. Its bent morphology confirms that the galaxy is falling toward the center of the cluster;
- We estimated that the arcs emission is characterized by an unusual steep spectral index (α <-2.5);
- We did not find any evidence of variation of the spectral index along the arcs within the uncertainties. For the first time, this provides strong constraints on the models for the origin of the radio arcs.;
- Assuming the jet-precession model, we derived the radiative age of the radio arcs under different assumptions for the magnetic field strengths. We find that the age of the arcs is ∼30 Myr and ∼130 Myr assuming the equipartition magnetic field H_{eq} and the magnetic field $H = H_{CMB}/\sqrt{3}$,

respectively. Most important, the fact that we do not detect any trend of the spectral index as a function of the position in the arcs implies a maximum difference of the age of the radio plasma across the arcs $\Delta t_{rad} = 5 - 10$ Myr. Such a difference in age constraints the kinematics in the jet-precession model challenging this hypothesis (Chapter 5).

The main results of the X-ray analysis can be summarized as follows:

- We find that the radio arcs are located at the edge of a high pressure, low temperature region. This is particularly clear at SW edge of the cold gas. More specifically, we examined the spectral maps (Fig. 4.9), finding that the ICM is composed by a inner cold region with T_{cold} ~2.4 keV and an outer hot region with T_{hot} ~3.4 keV. The edge of these coincides with the S-W junction of the radio arcs. Moreover, the cold ICM is not confined in the inner part of A2626, but it is elongated outside in a spiral-like shape;

- We carried out two independent methods to study the surface brightness, the 2D fit (Fig. 4.11) and the Gaussian gradient (Fig. 4.12), discovering the presence of an anomalous emission excess located at South-West. The excess is delimited by the junction of the radio arcs. We measured a density jump $\rho_i/\rho_o = 1.2$ that is located at ~ 27 kpc from the core, through the analysis of the surface brightness profiles over the junction. By analyzing the spectral profiles, we discovered a cold front in the ICM, that coincides with the south-west junction of the radio arcs

The lack of a spectral index trend across the radio arcs challenges the current models, whereas the connection between cold fronts (or in general thermal properties) and radio arcs may suggest that these arcs are generated by particle acceleration mechanisms operating in the ICM.

Therefore, we propose a new scenario for the origin of the radio arcs. We propose that the radio arcs are the brightest edges of a mini-halo. According to ZuHone et al. (2013) mini-halos may be generated by turbulent acceleration in cold fronts generated by the sloshing of the gas in cool-core clusters. When this mechanism is inefficient the radiation is generated with very steep spectrum and preferentially in the regions where magnetic fields and turbulence are stronger. This results in arcs-like emissions tracing cold fronts, a behaviour that is very similar to that observed in A2626. In this case the geometry of the radio arcs is generated by the sloshing of the gas responsible for the cold fronts. This requires a complex dynamics and 3D geometry that must be explored with *ad hoc* numerical simulations.

Our results may represent a new development in the comprehension of the ICM physics, because they provide evidences that non-thermal filaments, as the radio arcs, are able to trace the dynamics of the ICM. The future radio observatories, as SKA or LOFAR, may be able to locate many others of these filaments, providing a new tool to study the galaxy clusters.

Appendix A

A simple relationship between the spectral index and the radiative age

A.1 Analytical derivation

We derived a mathematical relation between the observed spectral index α and the radiative time t_{rad} of the emitting population. The synchrotron emission involves that, as the electrons lose energy due to the synchrotron emission, the break frequency ν_{br} of the synchrotron spectrum moves to lower frequencies. For an isotropic injection of electrons, where also the pith angle has an isotropic distribution (JP model Jaffe and Perola 1974), the relation between t_{rad} and ν_{br} may be written as:

$$t_{rad} = \frac{1.62 \cdot 10^3 (H)^{1/2}}{(H^2 + H_{CMB}^2)\sqrt{\nu_{br}}} \text{ Myr} \tag{A.1}$$

Where H is the local magnetic field and H_{CMB} is the equivalent magnetic filed of the Cosmic Microwave Background (CMB), that contributes to the energy loss of the relativistic electrons by interacting via Inverse Compton scatter.

The radiative life-span is maximized by a certain value of H:

$$\begin{aligned}\frac{dt_{rad}}{dH} &= \frac{1.62\cdot 10^{5}\sqrt{\nu_b r}}{\nu_{br}(H^2+H_{CMB}^2)^2}\left(\frac{H^2+H_{CMB}^2}{2\sqrt{H}}-2H\sqrt{H}\right)=\\ &= \frac{1.62\cdot 10^{5}\sqrt{\nu_b r}}{\nu_{br}(H^2+H_{CMB}^2)^2}(H_{CMB}^2\sqrt{H}-3H^2\sqrt{H})\end{aligned}$$

so:

$$\frac{dt_{rad}}{dH}=0 \Leftrightarrow H_{CMB}^2\sqrt{H}-3H^2\sqrt{H}=0 \implies H=\frac{H_{CMB}}{\sqrt{3}}=\frac{3.25(1+z)^2}{\sqrt{3}} \tag{A.2}$$

If we use the condition A.2 in A.1 we find the upper limit of the radiative time for a specific value of ν_{br}:

$$t_{rad}^2=\frac{8.5\cdot 10^5}{[3.25(1+z)^2]^3}\frac{1}{\nu_{br}}=\frac{8.5\cdot 10^5}{[3.25(1+z)^2]^3}\frac{k}{\nu^{obs}} \tag{A.3}$$

where

$$k=\frac{\nu^{obs}}{\nu_{br}} \tag{A.4}$$

is the ratio between the observed frequency ν^{obs} and the ν_{br}.
The synchrotron emissivity per volume unit of a population emitting particles is defined as:

$$J_{sy}(k)=\int_0^\infty\int_0^\infty F(k,H)\ n(E)dEdH \tag{A.5}$$

where $F(k,H)$ is the synchrotron kernel of a single electron and

$$n(E)\propto E^{-\Gamma} \tag{A.6}$$

is the distribution function of the energy of the population. Eilek and Arendt (1996) derived an approximation to Eq. A.5 for $H=H_0$ and $n(E)\propto E^{-\Gamma}$:

$$J(k)=j_0 n_e H_0 R_E^{\Gamma-1}e^{-k}k^{-\frac{\Gamma-1}{2}} \tag{A.7}$$

where R_E is dimensionless ratio between the limits of the particles energy range, n_e is the electron density and j_0 is the proportional factor.

We use this approximation to calculate the spectral index α between two pseudo-frequencies k_1 and k_2 as:

$$\begin{aligned}
\alpha =& \frac{ln\left(\frac{J(k_2)}{J(k_1)}\right)}{ln\left(\frac{k_2}{k_1}\right)} = \\
=& \frac{1}{ln\left(\frac{k_2}{k_1}\right)} ln\left(\frac{j_0 n_e H_0 R_E^{\Gamma-1} e^{-k_2} k_2^{-\frac{\Gamma-1}{2}}}{j_0 n_e H_0 R_E^{\Gamma-1} e^{-k_1} k_1^{-\frac{\Gamma-1}{2}}}\right) = \\
=& \frac{1}{ln(R)} ln\left[e^{(-Rk_1+k_1)} R^{-\frac{\Gamma-1}{2}}\right] = \text{ where } R = \frac{k_2}{k_1} = \frac{\nu_2^{obs}}{\nu_1^{obs}} \\
=& \frac{1}{ln(R)}\left[ln\left(e^{-Rk_1+k_1}\right) + ln\left(R^{-\frac{\Gamma-1}{2}}\right)\right] = \\
=& \frac{1}{ln(R)}\left[(1-R)k_1 + ln\left(R^{-\frac{\Gamma-1}{2}}\right)\right] = \\
=& \frac{(1-R)}{ln(R)}k_1 + \frac{ln\left(R^{-\frac{\Gamma-1}{2}}\right)}{ln(R)} = \\
=& \frac{(1-R)}{ln(R)}k_1 - \frac{\Gamma-1}{2}
\end{aligned} \tag{A.8}$$

We can now substitute k with ν_{br} (Eq. A.4) or with t_{rad} (Eq. A.3). On the one hand, we obtain the relation between spectral index and break frequency:

$$\alpha(\nu_{br}) = \frac{(1-R)}{ln(R)}\frac{\nu_1^{obs}}{\nu_{br}} - \frac{\Gamma-1}{2} \tag{A.9}$$

On the other hand, we derive the spectral index-radiative time relation:

$$\alpha(t_{rad}) = \frac{(1-R)}{ln(R)}\frac{[3.25(1+z)^2]^3}{8.5\cdot 10^5}\left(\frac{\nu_1^{obs}}{[\text{GHz}]}\right)\left(\frac{t_{rad}}{[\text{Myr}]}\right)^2 - \frac{\Gamma-1}{2} \tag{A.10}$$

A.2 Numerical test

In order to test the solidity of our results we compare the analytical and the numerical estimates. We built a code to estimate the radiative time from the frequencies of the observations ν_1^{obs} and ν_2^{obs}, the injection index Γ and the redshift z of a radio source, that is used to compute the magnetic field of the source on the basis of Eq. A.2.
For every iteration i the code computes the k_i, which goes from 0.1 to 5.0 with a

step of 0.1, the emissivity $J(k_i)$ by integrating Eq. A.5 and the respective $J(k_i^c)$ where:

$$k_i^c = \frac{\nu_2^{obs}}{\nu_1^{obs}} k_i = R k_i \tag{A.11}$$

Then, the code computes the spectral index α_i as:

$$\alpha_i = \frac{log(J(k_i)) - log(J(k_i^c))}{log(k_i) - log(k_i^c)} \tag{A.12}$$

and it estimates the position of the break frequency of each couple $(k\text{-}k^c)_i$ as:

$$\nu_{br}^i = \frac{\nu_1^{obs}}{k_i} \text{ GHz} \tag{A.13}$$

Finally it applies Eq. A.3 to estimate the t_{rad}^i from the ν_{br}^i and the redshift z. Eventually, after it collects all of these values, the code stores every result in a data file, where they can be plotted as shown in Fig.(A.1).

The analytical approximation of the emissivity (Fig. A.2) produces a spectrum which is slightly flatter than the numerical integration. This difference becomes lesser evident in Fig. A.4-A.5, proving the validity of the $\alpha(t_{rad})$ relation.

A.3 Radiative age map

The $\alpha(t_{rad})$ equation allows us a to derive straightforwardly the radiative age of the radio emitting plasma from the measured spectrum ::

$$t_{rad}(\alpha) = \sqrt{\frac{ln(R)}{(1-R)} \frac{8.5 \cdot 10^5}{[3.25(1+z)^2]^3} \left(\frac{\nu_1^{obs}}{[\text{GHz}]}\right)^{-1} \left(\alpha + \frac{\Gamma - 1}{2}\right)} \text{ Myr} \tag{A.14}$$

This equation is more "observer-friendly" than Eq.A.10, because, often, the spectral index is the observable feature and one wants to estimate t_{rad} of the source. This relation can be used to convert a spectral index map into a radiative time map. In this case, it is necessary to estimate also a $\sigma_t(\alpha, \sigma_\alpha)$ to monitor the solidity of the map. The generalized formula to obtain the radiative map $t_{rad}(\alpha, \sigma_\alpha)$ from the spectral index map α and the spectral index error map σ_α is:

$$t_{rad}(\alpha, \sigma_\alpha) = \sqrt{C\,(\alpha + B)} \pm \frac{C\sigma_\alpha}{2\sqrt{C\,(\alpha + B)}} \text{ Myr} \tag{A.15}$$

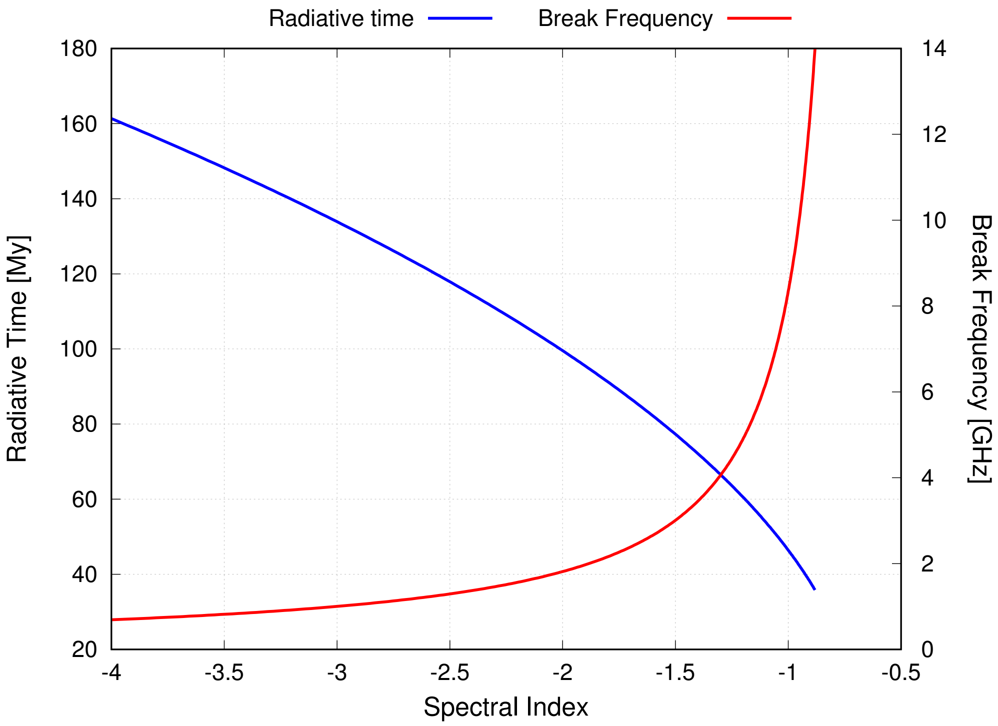

Figure A.1: Result of the numerical integration *Blue:* the relation between the observed spectral index between 1.4 and 3.0 GHz an the estimated age of the electron population; *Red:* the estimated position of the ν_{br} that produces the observed spectral index

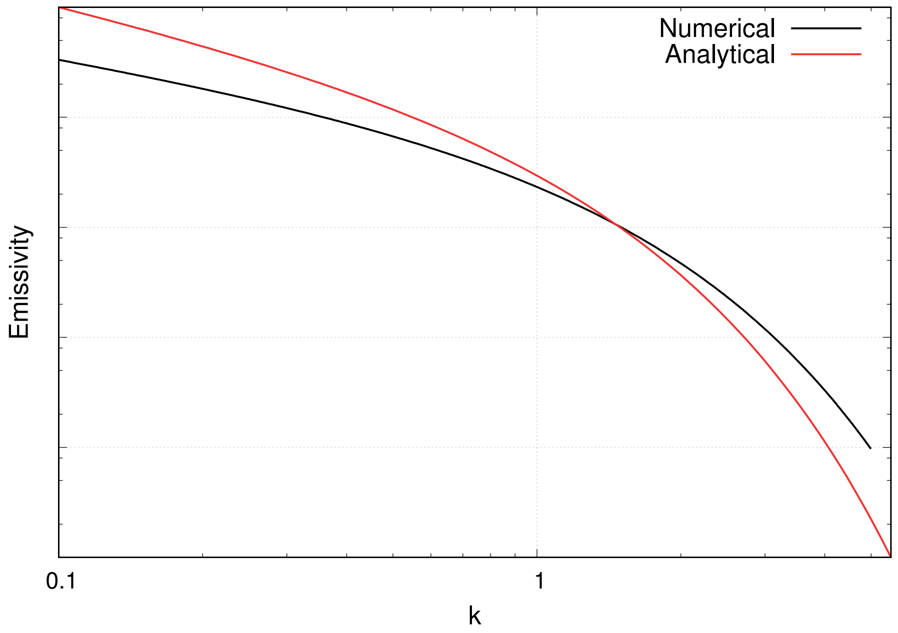

Figure A.2: Synchrotron spetrum computed by numerical integration of Eq. A.5 and the analytical approximation Eq. A.7

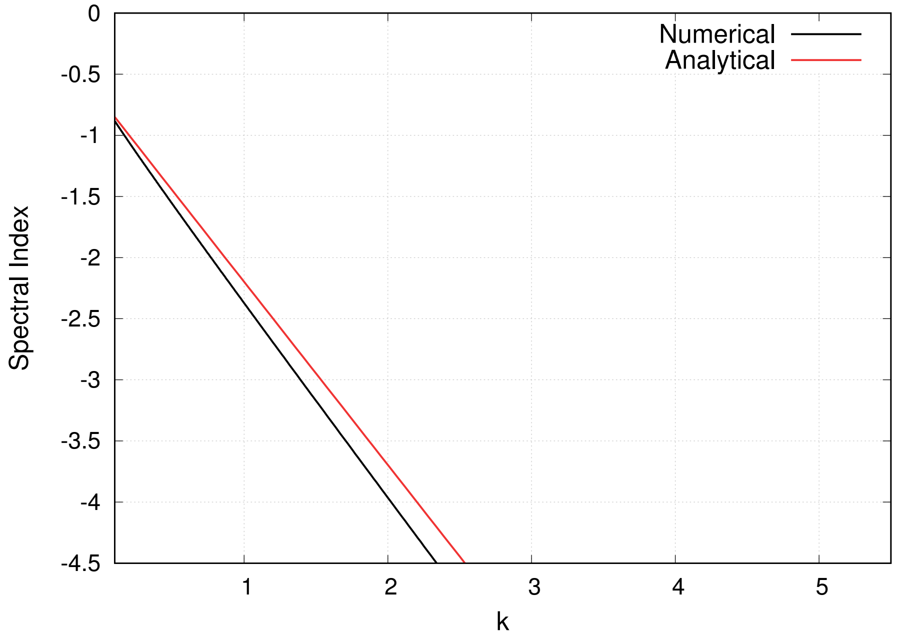

Figure A.3: The Spectral index vs k_1, with Γ=2.4 and a ratio R=2.14 between the observed frequencies, computed from the emissivity spectra reported in Fig. A.2

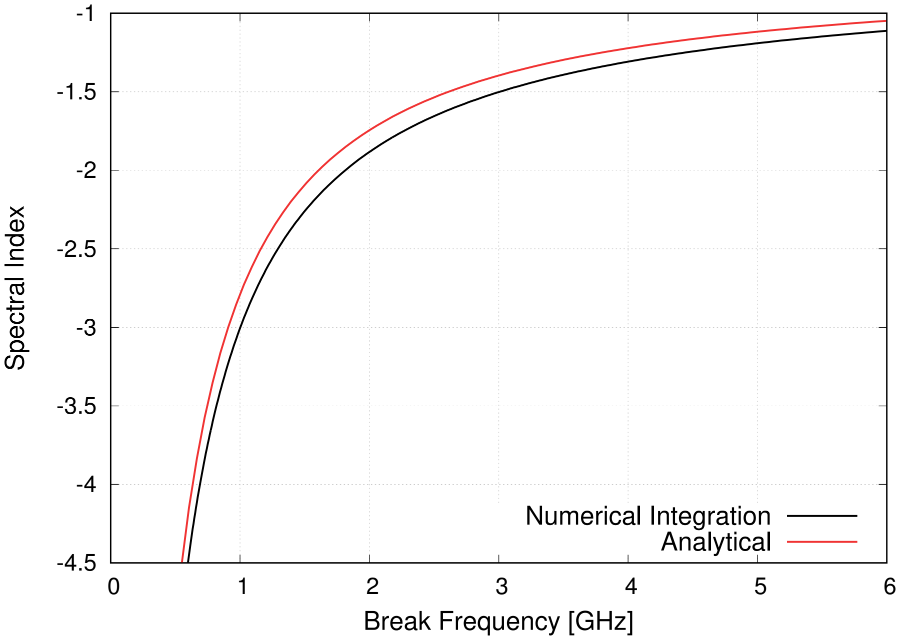

Figure A.4: Spectral Index vs Break frequency, with Γ=2.4, R=2.14 and ν_1^{obs}=1.4 GHz.

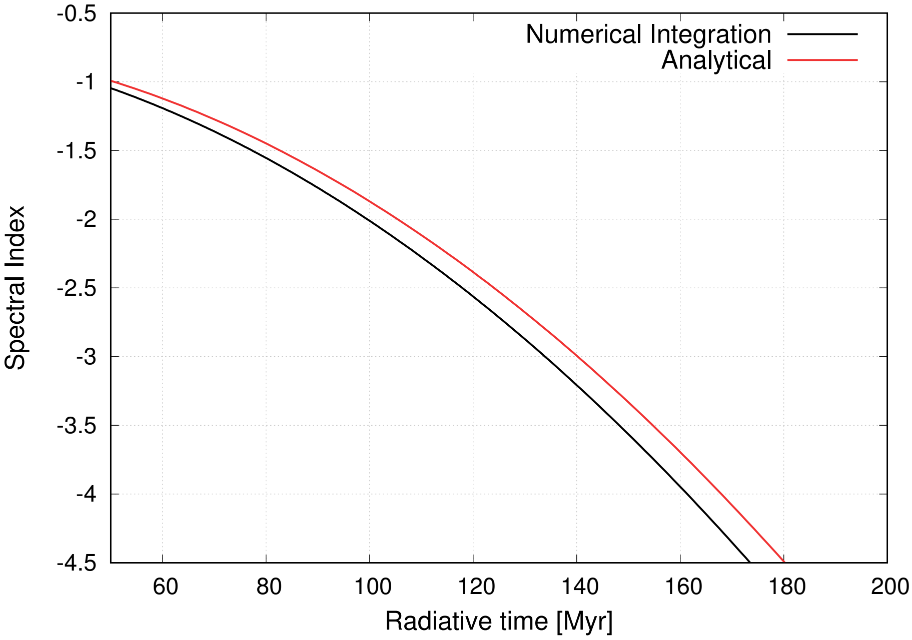

Figure A.5: Spectral index vs Radiative time, with Γ=2.4, z=0.053, R=2.14 and ν_1^{obs}=1.4 GHz.

where, according to Eq. A.14:

$$
\begin{aligned}
C =& \frac{ln(R)}{(1-R)} \frac{8.5 \cdot 10^5}{[3.25(1+z)^2]^3} \left(\frac{\nu_1^{obs}}{[\text{GHz}]} \right)^{-1} \\
B =& \frac{\Gamma - 1}{2}
\end{aligned}
\tag{A.16}
$$

The parameters C and B depend on the physical assumption about the magnetic field and the Injection index. They can be generalized to operate with every magnetic fields:

$$
\begin{aligned}
C =& 2.62 \cdot 10^6 \frac{ln(R)}{(1-R)} \frac{H}{(H^2 + H_{CMB}^2)^2} \left(\frac{\nu_1^{obs}}{[\text{GHz}]} \right)^{-1} \\
B =& \frac{\Gamma - 1}{2}
\end{aligned}
\tag{A.17}
$$

where H and H_{CMB} are expressed in μG.
The generalized formula can be applied to compute the radiative time in conditions of equipartition of the energy of the radio source.

Appendix B

Input maps for the spectral index estimates

In this Appendix we report the total intensity maps that we produced in order to compute the spectral index maps. In each map the contour levels ar at -3,3,6,12·RMS. In Tab. B we report the the input maps for each spectral index map.

Table B.1: Input maps for each spectral index map

Spectral index map	Input maps
3.9	B.1 B.2
3.10	B.3 B.4
3.11	B.5 B.6
3.12	B.7 B.8
3.13	B.1 B.9
3.14	B.2 B.9

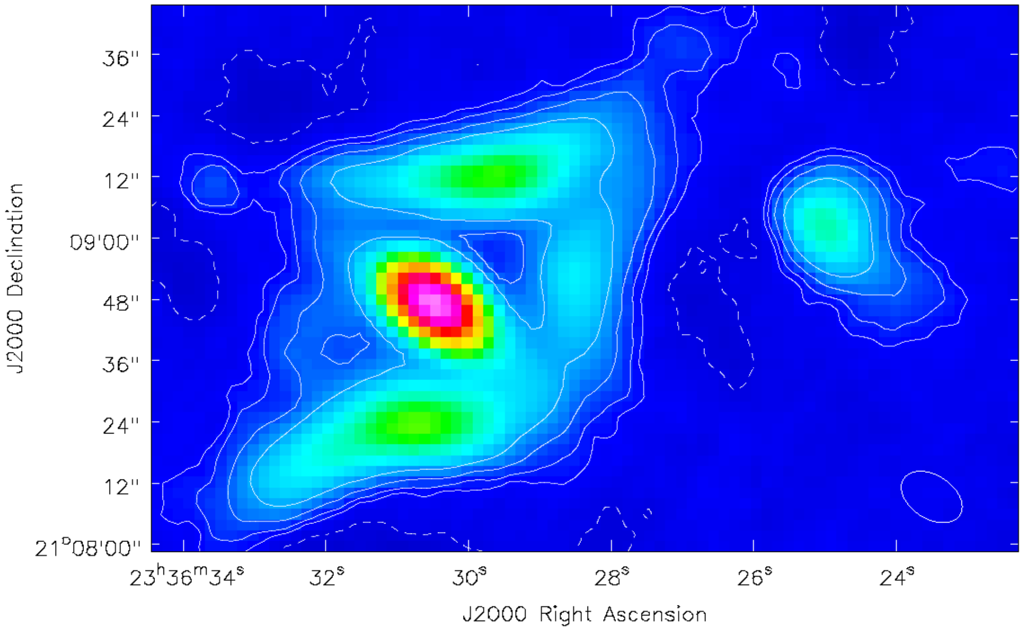

Figure B.1: 1.4 GHz image obtained by setting `NATURAL`, `nterms=1`, `UVRANGE=0-40`. The beam size is 13.1"x8.5". The RMS is 29.4 μJy beam^{-1}.

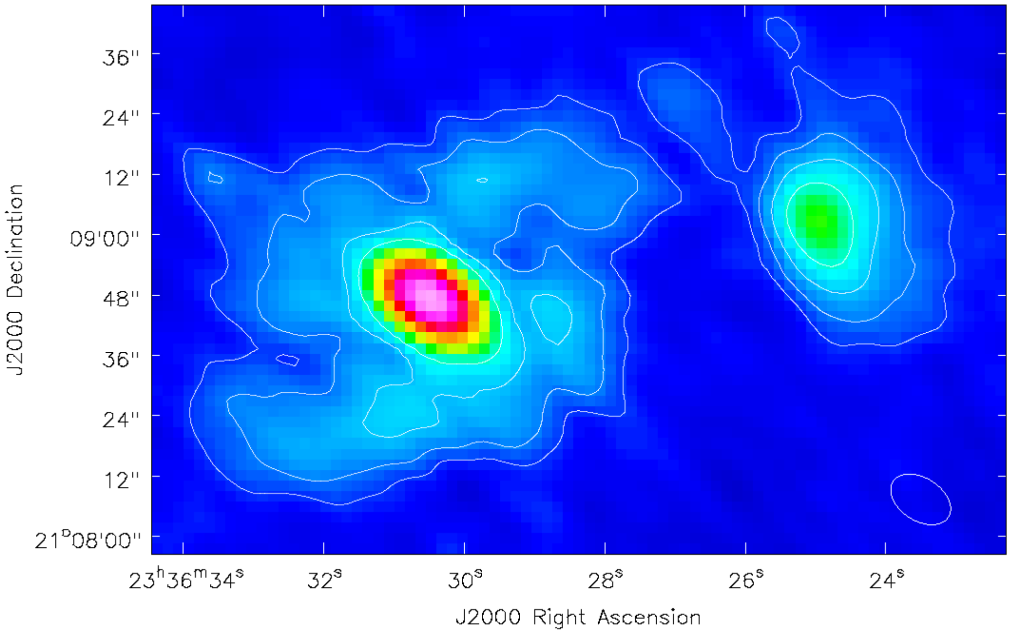

Figure B.2: 3.0 GHz image obtained by setting `NATURAL`, `nterms=1`, `UVRANGE=0-40`. The beam size is 13.1"x8.5". The RMS is 20.5 μJy beam^{-1}.

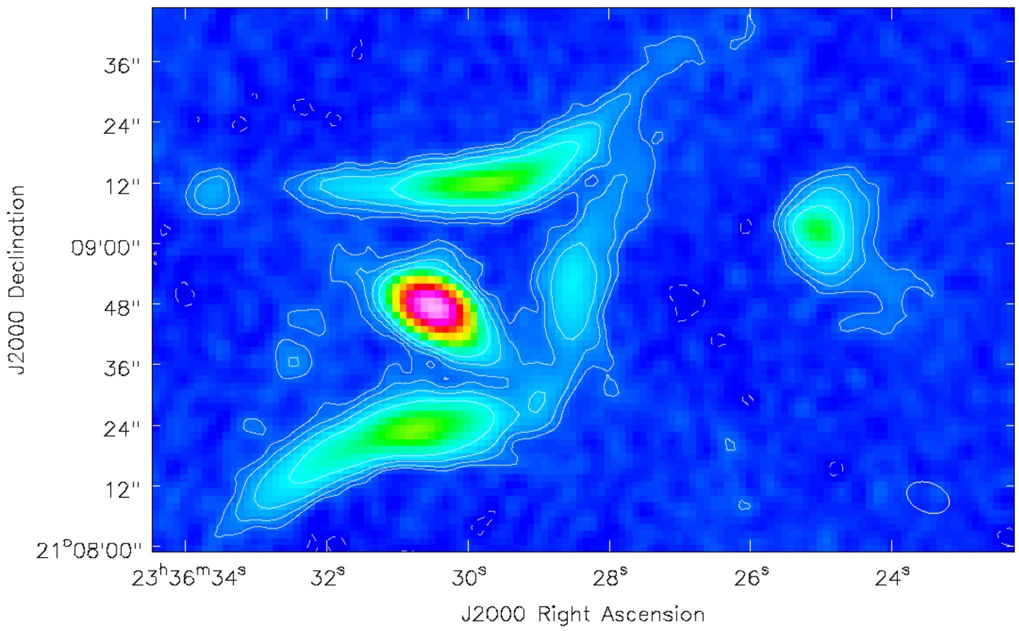

Figure B.3: 1.4 GHz image obtained by setting `ROBUST 0`, `nterms=2`, `UVRANGE=0-40`. The beam size is 8.7"x5.8". The RMS is 21.9 μJy beam^{-1}.

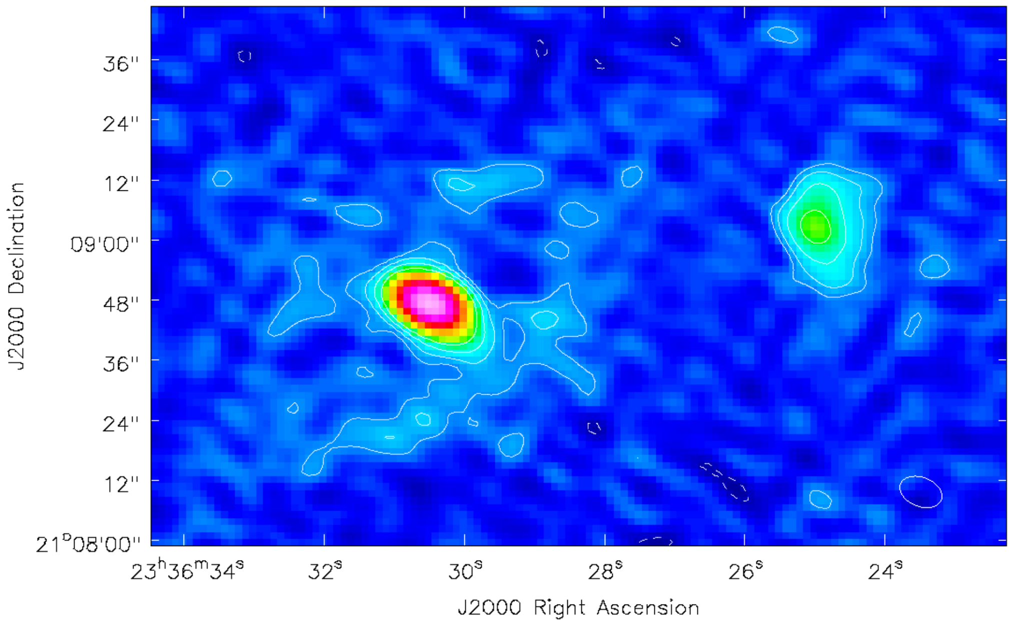

Figure B.4: 3.0 GHz image obtained by setting `ROBUST 0`, `nterms=2`, `UVRANGE=0-40`. The beam size is 8.7"x5.8". The RMS is 20.8 μJy beam^{-1}.

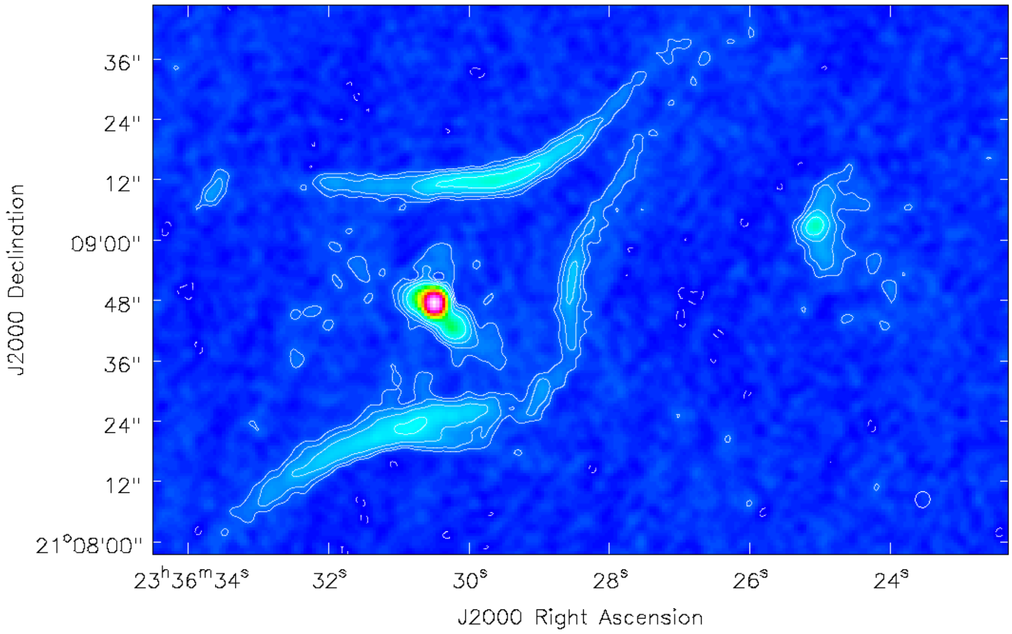

Figure B.5: 1.4 GHz image obtained by setting `ROBUST 0`, `nterms=2`, `UVRANGE=0-68`. The beam size is 3.2"x2.9". The RMS is 15.5 μJy beam^{-1}.

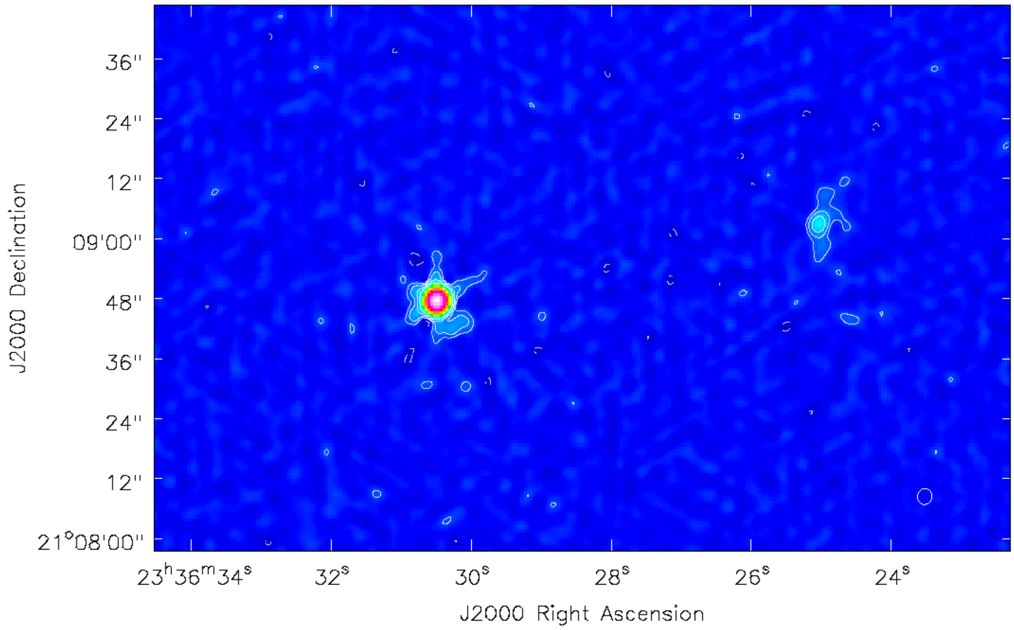

Figure B.6: 5.5 GHz image obtained by setting `ROBUST 0`, `nterms=2`, `UVRANGE=0-68`. The beam size is 3.2"x2.9". The RMS is 8.3 μJy beam^{-1}.

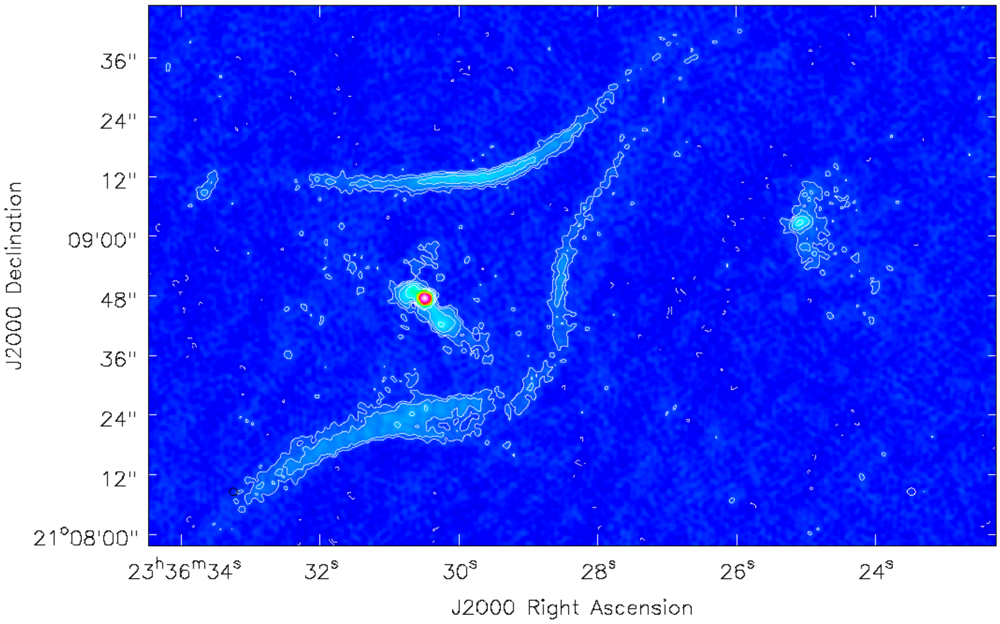

Figure B.7: 1.4 GHz image obtained by setting `ROBUST 0`, `nterms`=2, `UVRANGE=0-170`. The beam size is 1.6"x1.5". The RMS is 12.3 μJy beam^{-1}.

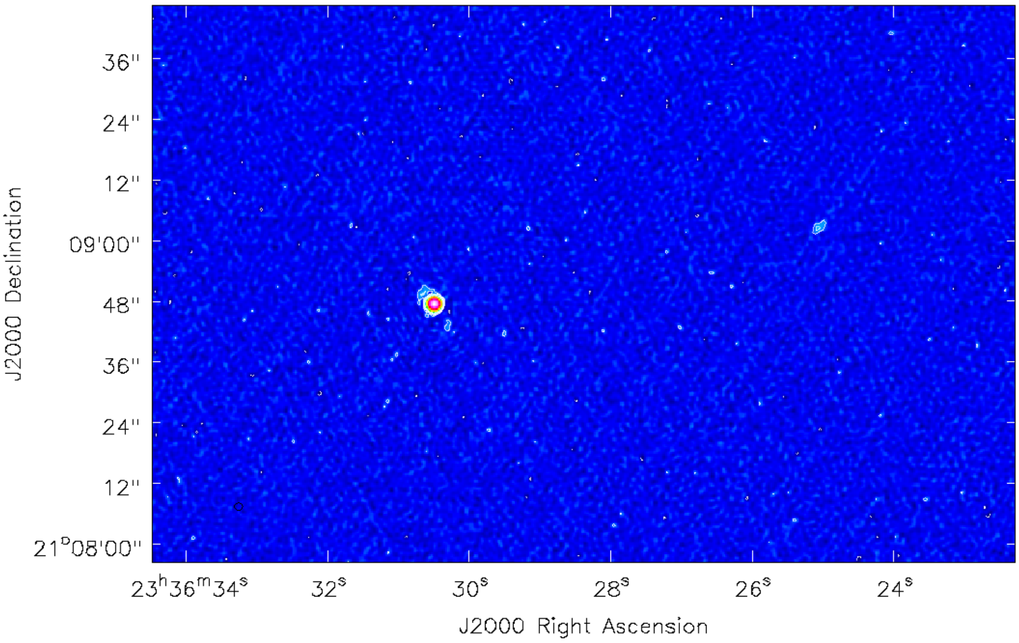

Figure B.8: 4.8 GHz image obtained by setting `ROBUST 0`, `nterms`=2, `UVRANGE=0-170`. The beam size is 1.6"x1.5". The RMS is 12.4 μJy beam^{-1}.

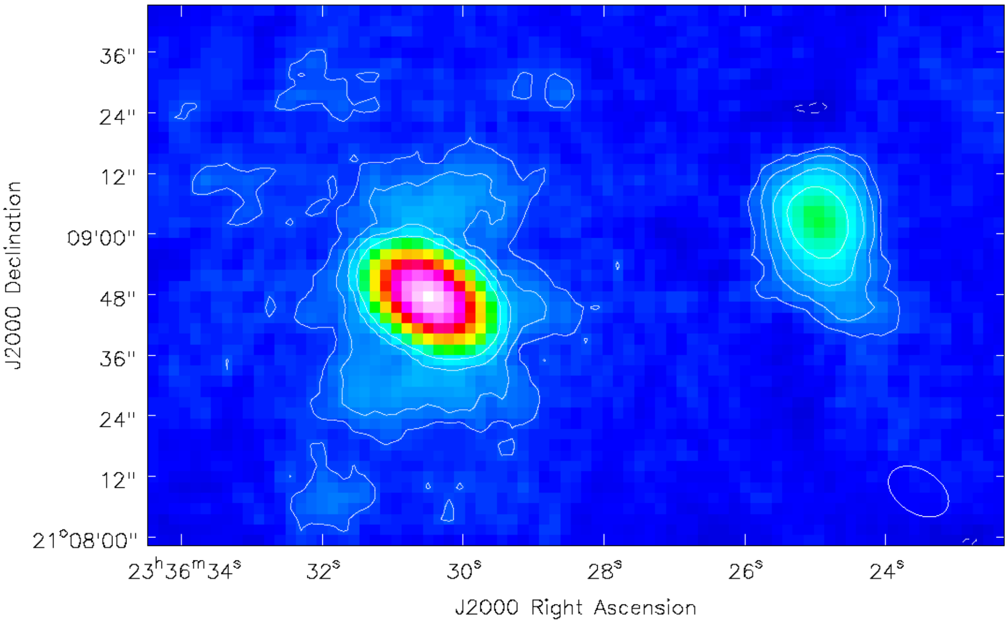

Figure B.9: 5.5 GHz image obtained by setting `NATURAL`, `nterms=1`, `UVRANGE=0-40`. The beam size is 13.1"x8.5". The RMS is 8.1 μJy beam^{-1}.

Bibliography

G. O. Abell. The Distribution of Rich Clusters of Galaxies. *Astrophysical Journal, Supplement*, 3:211–+, May 1958. doi: 10.1086/190036.

Z. Abraham and A. Caproni. 3C345: A Precessing Jet? In L. O. Takalo and E. Valtaoja, editors, *High Energy Blazar Astronomy*, volume 299 of *Astronomical Society of the Pacific Conference Series*, page 93, July 2003.

K. A. Arnaud. XSPEC: The First Ten Years. In G. H. Jacoby and J. Barnes, editors, *Astronomical Data Analysis Software and Systems V*, volume 101 of *Astronomical Society of the Pacific Conference Series*, page 17, 1996.

N. A. Bahcall. Clusters and superclusters of galaxies. *ArXiv Astrophysics e-prints*, November 1996.

R. Barvainis, J. Lehár, M. Birkinshaw, H. Falcke, and K. M. Blundell. Radio Variability of Radio-quiet and Radio-loud Quasars. *Astrophysical Journal*, 618: 108–122, January 2005. doi: 10.1086/425859.

L. Bravi, M. Gitti, and G. Brunetti. Do radio mini-halos and gas heating in cool-core clusters have a common origin? *Monthly Notices of the RAS*, 455: L41–L45, January 2016. doi: 10.1093/mnrasl/slv137.

G. Brunetti and T. W. Jones. Cosmic Rays in Galaxy Clusters and Their Nonthermal Emission. *International Journal of Modern Physics D*, 23:1430007, March 2014. doi: 10.1142/S0218271814300079.

G. Brunetti, G. Setti, L. Feretti, and G. Giovannini. Particle reacceleration in the Coma cluster: radio properties and hard X-ray emission. *Monthly Notices of the RAS*, 320:365–378, January 2001. doi: 10.1046/j.1365-8711.2001.03978.x.

J. O. Burns. The radio properties of cD galaxies in Abell clusters. I - an X-ray selected sample. *Astronomical Journal*, 99:14–30, January 1990. doi: 10.1086/115307.

A. M. Bykov, E. M. Churazov, C. Ferrari, W. R. Forman, J. S. Kaastra, U. Klein, M. Markevitch, and J. de Plaa. Structures and Components in Galaxy Clusters: Observations and Models. *Space Science Reviews*, 188(1): 141–185, 2015. ISSN 1572-9672. doi: 10.1007/s11214-014-0129-4. URL `http://dx.doi.org/10.1007/s11214-014-0129-4`.

C. L. Carilli and G. B. Taylor. Cluster Magnetic Fields. *Annual Review of Astronomy and Astrophysics*, 40:319–348, 2002. doi: 10.1146/annurev.astro.40.060401.093852.

A. Cava, D. Bettoni, B. M. Poggianti, W. J. Couch, M. Moles, J. Varela, A. Biviano, M. D'Onofrio, A. Dressler, G. Fasano, J. Fritz, P. Kjærgaard, M. Ramella, and T. Valentinuzzi. WINGS-SPE Spectroscopy in the WIde-field Nearby Galaxy-cluster Survey. *Astronomy and Astrophysics*, 495:707–719, March 2009. doi: 10.1051/0004-6361:200810997.

A. Cavaliere and R. Fusco-Femiano. X-rays from hot plasma in clusters of galaxies. *Astronomy and Astrophysics*, 49:137–144, May 1976.

E. Churazov, W. Forman, C. Jones, and H. Böhringer. Asymmetric, arc minute scale structures around NGC 1275. *Astronomy and Astrophysics*, 356:788–794, April 2000.

E. Churazov, M. Brüggen, C. R. Kaiser, H. Böhringer, and W. Forman. Evolution of Buoyant Bubbles in M87. *Astrophysical Journal*, 554:261–273, June 2001. doi: 10.1086/321357.

T. J. Cornwell, K. Golap, and S. Bhatnagar. The Noncoplanar Baselines Effect in Radio Interferometry: The W-Projection Algorithm. *IEEE Journal of Selected Topics in Signal Processing*, 2:647–657, November 2008. doi: 10.1109/JSTSP.2008.2005290.

J. A. Eilek and P. N. Arendt. The Synchrotron Spectrum of Diffuse Radio Sources: Effects of Particle and Field Distributions. *Astrophysical Journal*, 457:150, January 1996. doi: 10.1086/176719.

M. Einasto, J. Einasto, E. Tago, V. Müller, and H. Andernach. Optical and X-Ray Clusters as Tracers of the Supercluster-Void Network. I. Superclusters of Abell and X-Ray Clusters. *Astronomical Journal*, 122:2222–2242, November 2001. doi: 10.1086/323707.

A. C. Fabian, C. R. Canizares, and H. Boehringer. Mergers, cooling flows, and evaporation revisited. *Astrophysical Journal*, 425:40–42, April 1994. doi: 10.1086/173959.

J. E. Felten, R. J. Gould, W. A. Stein, and N. J. Woolf. X-Rays from the Coma Cluster of Galaxies. *Astrophysical Journal*, 146:955–958, December 1966. doi: 10.1086/148972.

L. Feretti, G. C. Perola, and R. Fanti. Tailed radio sources as probes of the intergalactic medium pressure. *Astronomy and Astrophysics*, 265:9–18, November 1992.

L. Feretti, G. Giovannini, F. Govoni, and M. Murgia. Clusters of galaxies: observational properties of the diffuse radio emission. *Astronomy and Astrophysics Reviews*, 20:54, May 2012. doi: 10.1007/s00159-012-0054-z.

M. Gitti. The puzzling radio source in the cool core cluster A2626. *Monthly Notices of the RAS*, 436:L84–L88, November 2013. doi: 10.1093/mnrasl/slt118.

M. Gitti, G. Brunetti, and G. Setti. Modeling the interaction between ICM and relativistic plasma in cooling flows: The case of the Perseus cluster. *Astronomy and Astrophysics*, 386:456–463, May 2002. doi: 10.1051/0004-6361:20020284.

M. Gitti, G. Brunetti, L. Feretti, and G. Setti. Particle acceleration in cooling flow clusters of galaxies: The case of Abell 2626. *Astronomy and Astrophysics*, 417:1–11, April 2004. doi: 10.1051/0004-6361:20031750.

M. Gitti, F. Brighenti, and B. R. McNamara. Evidence for AGN Feedback in Galaxy Clusters and Groups. *Advances in Astronomy*, 2012:950641, 2012. doi: 10.1155/2012/950641.

J. A. Högbom. Aperture Synthesis with a Non-Regular Distribution of Interferometer Baselines. *Astronomy and Astrophysics, Supplement*, 15:417, June 1974.

J. P. Huchra, M. S. Vogeley, and M. J. Geller. The CFA Redshift Survey: Data for the South Galactic CAP. *Astrophysical Journal, Supplement*, 121:287–368, April 1999. doi: 10.1086/313194.

W. Jaffe and G. C. Perola. The central radio source in three rich clusters of galaxies. *Astronomy and Astrophysics*, 31:223–234, March 1974.

C. R. Kaiser and P. Alexander. A self-similar model for extragalactic radio sources. *Monthly Notices of the RAS*, 286:215–222, March 1997. doi: 10.1093/mnras/286.1.215.

R. Kale and M. Gitti. Discovery of a fourth arc in Abell 2626 at 610 MHz with the GMRT: spectral properties and possibilities for the origin. *Monthly Notices of the RAS*, 466:L19–L23, March 2017. doi: 10.1093/mnrasl/slw227.

J.-P. Kneib and P. Natarajan. Cluster lenses. *Astronomy and Astrophysics Reviews*, 19:47, November 2011. doi: 10.1007/s00159-011-0047-3.

M. Markevitch and A. Vikhlinin. Shocks and cold fronts in galaxy clusters. *Physics Reports*, 443:1–53, May 2007. doi: 10.1016/j.physrep.2007.01.001.

P. Mazzotta and S. Giacintucci. Do Radio Core-Halos and Cold Fronts in Non-Major-Merging Clusters Originate from the Same Gas Sloshing? *Astrophysical Journal, Letters*, 675:L9–L12, March 2008. doi: 10.1086/529433.

B. R. McNamara and P. E. J. Nulsen. Heating Hot Atmospheres with Active Galactic Nuclei. *Annual Review of Astronomy and Astrophysics*, 45:117–175, September 2007. doi: 10.1146/annurev.astro.45.051806.110625.

B. R. McNamara and P. E. J. Nulsen. Mechanical feedback from active galactic nuclei in galaxies, groups and clusters. *New Journal of Physics*, 14(5):055023, May 2012. doi: 10.1088/1367-2630/14/5/055023.

K. Meisenheimer, M. G. Yates, and H.-J. Roeser. The synchrotron spectra of radio hot spots. II. Infrared imaging. *Astronomy and Astrophysics*, 325:57–73, September 1997.

C. Messier. Catalogue des Nébuleuses des amas d'Étoiles (Catalog of Nebulae and Star Clusters). Technical report, 1781.

E. Middelberg and U. Bach. High resolution radio astronomy using very long baseline interferometry. *Reports on Progress in Physics*, 71(6):066901, June 2008. doi: 10.1088/0034-4885/71/6/066901.

R. Mittal, D. S. Hudson, T. H. Reiprich, and T. Clarke. AGN heating and ICM cooling in the HIFLUGCS sample of galaxy clusters. *Astronomy and Astrophysics*, 501:835–850, July 2009. doi: 10.1051/0004-6361/200810836.

J. J. Mohr, M. J. Geller, and G. Wegner. A Dynamical Analysis of the Poor Galaxy Clusters Abell 2626 and Abell 2440. *Astronomical Journal*, 112:1816, November 1996. doi: 10.1086/118144.

R. Morrison and D. McCammon. Interstellar photoelectric absorption cross sections, 0.03-10 keV. *Astrophysical Journal*, 270:119–122, July 1983. doi: 10.1086/161102.

M. Murgia, F. Govoni, L. Feretti, G. Giovannini, D. Dallacasa, R. Fanti, G. B. Taylor, and K. Dolag. Magnetic fields and Faraday rotation in clusters of galaxies. *Astronomy and Astrophysics*, 424:429–446, September 2004. doi: 10.1051/0004-6361:20040191.

P. E. J. Nulsen, L. P. David, B. R. McNamara, C. Jones, W. R. Forman, and M. Wise. Interaction of Radio Lobes with the Hot Intracluster Medium: Driving Convective Outflow in Hydra A. *Astrophysical Journal*, 568:163–173, March 2002. doi: 10.1086/338494.

P. E. J. Nulsen, D. C. Hambrick, B. R. McNamara, D. Rafferty, L. Birzan, M. W. Wise, and L. P. David. The Powerful Outburst in Hercules A. *Astrophysical Journal, Letters*, 625:L9–L12, May 2005. doi: 10.1086/430945.

E. O'Sullivan, S. Giacintucci, L. P. David, J. M. Vrtilek, and S. Raychaudhury. A deep Chandra observation of the poor cluster AWM 4 - II. The role of the radio jets in enriching the intracluster medium. *Monthly Notices of the RAS*, 411:1833–1842, March 2011. doi: 10.1111/j.1365-2966.2010.17812.x.

J. Oukbir and A. Blanchard. X-ray clusters in open universes. *Astronomy and Astrophysics*, 262:L21–L24, September 1992.

A. G. Pacholczyk. *Radio astrophysics. Nonthermal processes in galactic and extragalactic sources*. 1970.

J. R. Peterson and A. C. Fabian. X-ray spectroscopy of cooling clusters. *Physics Reports*, 427:1–39, April 2006. doi: 10.1016/j.physrep.2005.12.007.

V. Petrosian and J. Dickey. Flux-Density Relation of Extragalactic Radio Sources. *Astrophysical Journal*, 186:403–420, December 1973. doi: 10.1086/152508.

C. Pfrommer and T. A. Enßlin. Constraining the population of cosmic ray protons in cooling flow clusters with γ-ray and radio observations: Are radio mini-halos of hadronic origin? *Astronomy and Astrophysics*, 413:17–36, January 2004. doi: 10.1051/0004-6361:20031464.

B. M. Poggianti, G. Fasano, A. Omizzolo, M. Gullieuszik, D. Bettoni, A. Moretti, A. Paccagnella, Y. L. Jaffé, B. Vulcani, J. Fritz, W. Couch, and M. D'Onofrio. Jellyfish Galaxy Candidates at Low Redshift. *Astronomical Journal*, 151:78, March 2016. doi: 10.3847/0004-6256/151/3/78.

U. Rau and T. J. Cornwell. A multi-scale multi-frequency deconvolution algorithm for synthesis imaging in radio interferometry. *Astronomy and Astrophysics*, 532:A71, August 2011. doi: 10.1051/0004-6361/201117104.

E. Rizza, C. Loken, M. Bliton, K. Roettiger, J. O. Burns, and F. N. Owen. X-Ray and Radio Interactions in the Cores of Cooling Flow Clusters. *Astronomical Journal*, 119:21–31, January 2000. doi: 10.1086/301167.

L. Rudnick and F. N. Owen. Head-tail radio sources in clusters of galaxies. *Astrophysical Journal, Letters*, 203:L107–L111, February 1976. doi: 10.1086/182030.

J. S. Sanders, A. C. Fabian, H. R. Russell, S. A. Walker, and K. M. Blundell. Detecting edges in the X-ray surface brightness of galaxy clusters. *Monthly Notices of the RAS*, 460:1898–1911, August 2016. doi: 10.1093/mnras/stw1119.

C. L. Sarazin. X-ray emission from clusters of galaxies. *Reviews of Modern Physics*, 58:1–115, January 1986. doi: 10.1103/RevModPhys.58.1.

J. Shin, J.-H. Woo, and J. S. Mulchaey. A Systematic Search for X-Ray Cavities in Galaxy Clusters, Groups, and Elliptical Galaxies. *Astrophysical Journal, Supplement*, 227:31, December 2016. doi: 10.3847/1538-4365/227/2/31.

M. F. Struble and H. J. Rood. A Compilation of Redshifts and Velocity Dispersions for ACO Clusters. *Astrophysical Journal, Supplement*, 125:35–71, November 1999. doi: 10.1086/313274.

R. S. Sutherland and M. A. Dopita. Cooling functions for low-density astrophysical plasmas. *Astrophysical Journal, Supplement*, 88:253–327, September 1993. doi: 10.1086/191823.

R. B. Tully, H. Courtois, Y. Hoffman, and D. Pomarède. The Laniakea supercluster of galaxies. *Nature*, 513:71–73, September 2014. doi: 10.1038/nature13674.

K.-W. Wong, C. L. Sarazin, E. L. Blanton, and T. H. Reiprich. XMM-Newton and Chandra Observations of Abell 2626: Interacting Radio Jets and Cooling Core with Jet Precession? *Astrophysical Journal*, 682:155–174, July 2008. doi: 10.1086/588272.

J. ZuHone, M. Markevitch, and G. Brunetti. Testing the Connection Between Radio Mini-Halos and Core Gas Sloshing with MHD Simulations. *ArXiv e-prints*, January 2011.

J. A. ZuHone, M. Markevitch, G. Brunetti, and S. Giacintucci. Turbulence and Radio Mini-halos in the Sloshing Cores of Galaxy Clusters. *Astrophysical Journal*, 762:78, January 2013. doi: 10.1088/0004-637X/762/2/78.

F. Zwicky. Die Rotverschiebung von extragalaktischen Nebeln. *Helvetica Physica Acta*, 6:110–127, 1933.

Grazie a tutti, davvero.